INFORMATION TO USERS

This manuscript has been reproduced from the microfilm master. UMI films the text directly from the original or copy submitted. Thus, some thesis and dissertation copies are in typewriter face, while others may be from any type of computer printer.

The quality of this reproduction is dependent upon the quality of the copy submitted. Broken or indistinct print, colored or poor quality illustrations and photographs, print bleedthrough, substandard margins, and improper alignment can adversely affect reproduction.

In the unlikely event that the author did not send UMI a complete manuscript and there are missing pages, these will be noted. Also, if unauthorized copyright material had to be removed, a note will indicate the deletion.

Oversize materials (e.g., maps, drawings, charts) are reproduced by sectioning the original, beginning at the upper left-hand corner and continuing from left to right in equal sections with small overlaps.

Photographs included in the original manuscript have been reproduced xerographically in this copy. Higher quality 6" x 9" black and white photographic prints are available for any photographs or illustrations appearing in this copy for an additional charge. Contact UMI directly to order.

Bell & Howell Information and Learning
300 North Zeeb Road, Ann Arbor, MI 48106-1346 USA

UMI®
800-521-0600

Experimental and Numerical Study of the Bleed Effect on the Propagation of Strong Plane and Converging Cylindrical Shock Waves

Mourad El-Mallah

A Thesis

in

The Department

of

Mechanical Engineering

Presented in partial fulfillment of the requirements
for the degree of Doctor of Philosophy at
Concordia University
Montreal, Quebec, Canada

May 1997

National Library of Canada
Acquisitions and Bibliographic Services
395 Wellington Street
Ottawa ON K1A 0N4
Canada

Bibliothèque nationale du Canada
Acquisitions et services bibliographiques
395, rue Wellington
Ottawa ON K1A 0N4
Canada

Your file Votre référence

Our file Notre référence

0-612-39791-2

Canada

ABSTRACT

Experimental and Numerical Study of the Bleed Effect on the Propagation of Strong Plane and Converging Cylindrical Shock Waves

Mourad El-Mallah, Ph.D.
Concordia University, 1997

A combined experimental-numerical study was conducted to determine the effect of bleeding on the propagation of plane and converging cylindrical shock waves. A fully 3-D Finite Element code was written for simulating inviscid unsteady flow in various cases of shock tube geometry. The scheme used was implicit time-marching with the Galerkin discretization for spatial coordinate derivatives and multi-step finite difference formulation for time derivatives. Initial trials with 1-D radial flow have shown good agreement with the analytical power law of shock propagation derived by Guderley.

The numerical code was first applied to the test case of shock wave strengthening through its reflection from a 15° ramp. The numerical results of the shock front shape were found to be in good agreement with the Schlieren photographs taken for the flow at different time intervals.

The numerical code was then applied to the test case of a plane shock interaction with a transverse slit. Experiments were carried out in this case to determine the degree of shock attenuation for shock Mach numbers ranging between 1.2 and 2.5, and slit-duct width

ratios varying between 0.25 to 1.0. For this test case, a simplified model - based on the Method of Characteristics and the Chester-Chisnel-Whitham (CCW) theory - was also introduced. Numerical results for the attenuated shock Mach number were found to be in excellent agreement with the experimental results and the approximate analytical model.

For the 2-D axisymmetric flows, domains similar to the plane flow cases were used to account for the radial convergence effect. Pressure measurements were also carried out at various radii to determine the pressure time history. The transmitted shock, past the slit, was found to undergo attenuation as in the 2-D case, but combined with strengthening due to area convergence. At the same location downstream of the slit, attenuation was found to be higher than in the 2-D case of similar slit-chamber width ratios.

ACKNOWLEDGMENTS

The author wishes to express his gratitude to his supervisor, Dr. Rafik A. Neemeh, for his sincere guidance and encouragement during the present work. His technical and moral support was an asset without which this work would not have been finalized.

Thanks are also extended to the staff of the Concordia University Faculty Workshop for their assistance throughout the experimental phase of the thesis work.

Finally, the author wishes to thank Ms. Laura Neemeh for revising the manuscript, and for her valuable assistance in preparing the figures for the thesis.

TABLE OF CONTENTS

	page
LIST OF FIGURES	ix
LIST OF TABLES	xi
NOMENCLATURE	xii
Chapter	
1 - INTRODUCTION	1
1.1 - Analytical Methods	3
1.2 - Experimental Methods	6
1.3 - Numerical Methods	8
1.4 - Shock Bleed Control	9
1.4.1 - Shock Diffraction and Reflection Processes	11
1.4.2 - Related Research Work	15
1.4.3 - Objective of the Present Work	19
2 - THEORETICAL BACKGROUND	22
2.1 - Alternative Formulations for Euler Equations	22
2.2 - One-Dimensional Formulation	25
2.2.1 - The Method of Characteristics	26
2.2.2 - Self-Similar Solutions	30
2.3 - Multi-Dimensional Formulation	34
2.3.1 - Quasi-One-Dimensional Treatment	35

2.3.2 - Geometrical Shock Dynamics
(Whitham Ray-shock Theory) 40

2.4 - Application to Shock Diffraction and Mach Reflection 45

3 - NUMERICAL METHOD 52

3.1 - Finite Element Method 54

3.2 - Governing Equations 57

3.3 - Weak Formulation 59

3.4 - Boundary Conditions 72

3.5 - Matrix Solution Requirements 74

4 - EXPERIMENTAL SETUP & PROCEDURE 76

4.1 - The Two-dimensional Shock Tube 76

4.1.1 - Experimental Setup 76

4.1.2 - Test Section Options 80

4.2 - The Axisymmetric Cylindrical Shock Tube 81

4.2.1 - Experimental Setup 81

4.2.2 - Test Section Options 84

4.3 - Monitoring Equipment 85

4.3.1 - Schlieren System 85

4.3.2 - Pressure Transducers 86

5 - RESULTS & DISCUSSION 90

5.1 - Shock Wave Reflection & Diffraction in a Ramp 90

5.1.1 - Experimental Results 90

5.1.2 - Analytical Results 91

5.1.3 - Numerical Results 92

5.2 - Shock Wave Interaction with a Narrow Slit 96

5.2.1 - Shock Attenuation Experimental Results 99

5.2.2 - Numerical Results 101

5.2.3 - Analytical Results 106

5.3 - Cylindrical Converging Shock Wave Bleeding 109

5.3.1 - Experimental Results 111

5.3.2 - Numerical Results 112

6 - CONCLUSION 117

Proposed Future Work 121

REFERENCES 124

LIST OF FIGURES

page

Fig.(1.1) Perry and Kantrowitz shock tube. 134

Fig.(1.2) Takayama and Watanabe shock tube. 135

Fig.(1.3) Shock-slit interaction (subsonic duct flow). 136

Fig.(1.4) Shock-slit interaction (supersonic duct flow). 137

Fig.(2.1) The (x , t) diagram for Guderley's implosion solution. 138

Fig.(2.2) The (x , t) diagram for shock propagation in a non-uniform area duct (subsonic flow behind the shock). 139

Fig.(2.3) The Chester function [ref.64]. 140

Fig.(2.4) Curvilinear quadrilateral element. 141

Fig.(2.5) Shock diffraction at a convex corner (subsonic flow behind the incident shock). 142

Fig.(2.6) Reflection of a moving shock wave. 143

Fig.(2.7) Ray-shock treatment of Mach reflection. 144

Fig.(3.1) Finite Element geometry. 145

Fig.(3.2) Flow chart for the numerical solution. 146

Fig.(4.1) 2-D shock tube experimental setup. 147

Fig.(4.2) Test sections used in the 2-D square shock tube. 148

Fig.(4.3) Test section for the cylindrical shock tube. 149

Fig.(4.4) The new test section. 150

Fig.(4.5) Specifications for the pressure transducers. 151

Fig.(4.6) Sample oscilloscope output for pressure transducer calibration. 152

Fig.(4.7) Pressure transducers' calibration curves. 153

Fig.(4.8) Sample oscilloscope output for the cylindrical imploding shock (near center, no bleed). 154

Fig.(5.1) Schlieren photos for shock propagation over a 15° ramp ($M_0 = 2.106$). 155

Fig.(5.2) Shock front stages for the ramp test case. 157

Fig.(5.3) Computational domain for the ramp test case. 158

Fig.(5.4) Density contours for the ramp test case. 159

Fig.(5.5) Grid sensitivity checks for the ramp problem ($M_0 = 2.106$) (density contours). 160

Fig.(5.6) Schlieren photos for shock-slit interaction ($M_0 = 2.33$) (Ostrowski [64]). 161

Fig.(5.7) Attenuation coefficient for shock-slit interaction. 162

Fig.(5.8) Computational domain for shock-slit interaction ($M_0 = 2.33$). 163

Fig.(5.9a) Density contours for shock-slit interaction ($M_0 = 2.33$, 40 time steps). 164

Fig.(5.9b) Density contours for shock-slit interaction ($M_0 = 2.33$, 80 time steps). 165

Fig.(5.9c) Density contours for shock-slit interaction ($M_0 = 2.33$, 120 time steps). 166

Fig.(5.9d) Density contours for outer diffracted shock ($M_0 = 2.33$, 150 time steps). 167

Fig.(5.10) Shock Mach number distribution along the duct walls (W/H = 1.0). 168

Fig.(5.11) Shock Mach number distribution along the duct walls (W/H = 2.0). 169

Fig.(5.12) Attenuation coefficient for the shock-slit interaction ($M_0 = 2.33$). 170

Fig.(5.13) The effect of incident Shock Mach number on bleed ratio (supersonic duct flow). 171

Fig.(5.14) Converging shock Mach number v/s shock radius. 172

Fig.(5.15) Pressure distribution for converging cylindrical shocks. 173

Fig.(5.16) Numerical and experimental pressure history at transducer locations ($M_0 = 2.33$). 174

LIST OF TABLES

page

Table (5.1) Experimental results for 2-D shock-slit interaction ($M_0 = 2.33$). 175

Table (5.2) Experimental results for cylindrical shock-slit interaction ($M_0 = 2.33$). 176

NOMENCLATURE

Latin Symbols :

A	Area.
A_e	Finite element surface area.
C^+ , C^-	Characteristic paths.
C_p , C_v	Specific heats under constant pressure, constant volume, respectively.
$C(\xi)$	Non dimensional speed of sound (self-similar solution).
c	Speed of sound.
$\frac{D}{Dt}$	Total derivative w.r.t. time (along particle path).
$\frac{D^{\pm}}{Dt}$	Derivative w.r.t. time along $C^{\pm}$ characteristics.
E	Energy released in explosion (self-similar solution).
e	Internal energy.
$\underline{e}_r$, $\underline{e}_\theta$, $\underline{e}_z$	Unit vectors in cylindrical co-ordinate directions.
F, G, H(x, t)	Source terms in characteristic equations.
F, G, H($\underline{U}$, t)	Flux vector terms in conservation P.D.E.s.
H	Duct or chamber width.
h	Enthalpy.
[I]	Identity matrix.
[J]	Jacobean matrix.

K(M)	Chester function.
(i , j , k)	Indices, iteration or series counters.
M, M_s	Shock Mach number.
m	Characteristic angle.
N_j	Finite element shape function.
n	Power-law exponent, 2.0/average Chester function K_{av} .
$\underline{n}$	Normal unit vector.
P	Particle path.
P	C^+ Riemann invariant.
P(ξ)	Non dimensional pressure (self-similar solution).
p	Pressure.
Q	C^- Riemann invariant.
R	Gas constant.
R(t)	Shock radius (self-similar solution).
r	Radius, radial co-ordinate.
$\underline{S}$	Source term vector.
s	Entropy.
T	Temperature.
t	Time.
U	Vector of convected variables.
U(ξ)	Non dimensional shock velocity (self-similar solution).
V_e	Finite element control volume.

$\underline{v}$, $\underline{V}$	Velocity vector.
$V(\xi)$	Non dimensional particle velocity (self-similar solution).
W	Slit width.
W_i	Finite element weight function.
(u, v, w)	Cartesian velocity components.
(x, y, z)	Cartesian co-ordinates.

Greek Symbols :

α , β	Ray-shock Theory co-ordinates.
γ	Specific heat ratio.
ϕ	Convected variable, shock angle for Ray-shock Theory's element.
λ	Eigenvalue, Lagrange multiplier.
λ (M)	Equivalent to Chester function (= 2.0 / K(M)).
μ	Viscosity, artificial dissipation coefficient.
ρ	Density.
θ	Angular cylindrical co-ordinate, flow angle, ray angle for Ray-shock Theory's element.
ξ	Non-dimensional radial co-ordinate r / R(t) (self-similar solution).
(ξ, η, ζ)	Finite element natural co-ordinates.
χ	Shock-shock angle.
$\Omega(\xi)$	Non-dimensional density (self-similar solution).

ω	Ray-shock Theory integral function.

Subscripts :

0	Incident, initial.
av	Average.
cr	Critical (sonic flow behind shock).
r	Radial.
sh	Shock.
t	Total (stagnation).
u	Non-bled.
z	Axial.
θ	tangential.

1 - INTRODUCTION

The creation and performance of shock waves have been the focus of study by many engineers and scientists working in topics related to continuum physics. Shock waves - either in their weak form (acoustic waves) or their moderate to stronger form - play an important part in scientific and engineering calculations whether their existence is desirable or not. For example, in the case of gas pipelines, a sudden valve closure or opening (or any other blockage or leak) creates a response signal in the form of shock or expansion waves, whose speeds depend on the aerothermodynamic state of the gas. The change in properties behind such waves should be taken into consideration for designing the pipeline as well as the surrounding installations (for safety considerations). Similar dangers exist in coal mining operations (due to methane gas explosions). In the latter case, explosions are more confined and tend to propagate through branches of underground tunnels. For internal combustion engines, the sudden opening and closing of valves create a continuous stream of shock or expansion waves, interacting and moving down the muffler as well as other ducts. This stream has to be controlled and optimized for environmental protection [1]. In the field of interior ballistics of guns, the existence of shock waves ahead of and behind the projectile is an unavoidable side-effect to contend with, and designs are made to divert the blast and reduce its noise level [2]. Another example is the shock wave formation ahead of underground trains while entering tunnels. While part of the air slides beside the train body, the major part is moved forward through a shock wave, causing a pressure rise and drag as well as noise at the tunnel ends [3].

Another important application is the use of cylindrical converging shock waves to produce localized high gas pressures and enthalpies. Theoretically, area convergence is expected to strengthen the shocks, thus producing infinitely dense amounts of energy at the center of convergence (point of collapse). Probably the most famous application in the military is the creation of partly converging - partly advancing shock waves in shaped charges for armor piercing. Furthermore, converging shocks are used to create naturally non-existent environments or materials for scientific research processes or applications. Examples of these processes are artificial diamond manufacturing from graphite [4], propulsion of projectiles at hypersonic speeds [5], rocket engine ignitions, thermonuclear fusion, and creating chemical non-equilibrium gas mixtures. The common factor here is the need for accumulating great amounts of energy in virtually point-size domains. This fact probably explains why the technical steps required to create converging shocks have their inherent difficulties.

For the case of cylindrical converging shock waves, one of the main issues faced in establishing the physical process is the shock stability. This is defined as the ability of the generated shocks to retain their required symmetric shapes if subjected to perturbations due to geometrical or physical irregularities, which is inevitable in practical considerations. Unlike plane shocks, which retain their shape due to transverse waves [6-9], cylindrical waves are affected by two contradictory processes: stabilizing effect due to the transverse waves, and the increase in shock speed associated with the reduction in the frontal area.

Therefore, the measure of stability for converging shocks should aim at minimizing the ratio between the magnitude of unavoidable perturbations, and the mean value of the shock radius.

The need to stabilize the shock for as long as possible requires an efficient method for simulating the shock performance throughout the implosion process. In this respect, research activities have been diversified according to the available theoretical and technical facilities.

1.1 - Analytical Methods

The converging shock problem was first handled theoretically in 1942 by Guderley [10] under the assumption of perfect inviscid gas. Guderley demonstrated that strong cylindrical converging shock waves propagate according to a power-law relation when approaching the center and that their Mach numbers reach infinite values at the point of collapse. However, this is not possible in reality due to the effect of viscosity and heat conduction. Subsequent studies were conducted under the same assumptions by Lighthill [11], Butler [12,13], Stanyukouvich [14] and Whitham [22].

Theoretical handling of the one-dimensional form of governing equations continues to this day [e.g., 15-19], with the introduction of new equations of state or constitutive relations

to simulate shock dynamics in more complicated physical situations, or in other types of continua (including real gases).

During the same period, the development of the CCW theory deduced concurrently by Chester, Chisnell and Whitham [20-22], as well as Whitham's Ray-shock Theory [23,24], provided researchers with a new graphically-operable tool to simulate shock dynamics. For the CCW theory, shocks are considered as discontinuities between continuously varying sections of fluids. The continuous fluid sections were solved for by using the modified set of quasi-1-D Euler equations in its characteristics form, while the variations across wave fronts are governed by the Rankine - Hugoniot relations. The final result was a new governing equation relating the local duct area (at shock location) to the local shock Mach number, incorporating the newly-defined Chester function, named after its inventor. Although the quasi-1-D derivation was meant to deal with flows in ducts with varying cross sections, the simplified set of equations was used for handling the cylindrical and spherical converging shocks (where symmetry ensures one-dimensionality) [26,27].

This method of solution was extended to multiple dimensions using the Ray-shock Theory deduced by Whitham [23,24]. Based on concepts from geometrical acoustics, the method employs successive shock contours and their orthogonal trajectories (rays) as curvilinear coordinate lines. It was assumed that no lateral flow takes place across the ray lines, meaning that the rays coincide with streamlines at the shock location. The geometrical compatibility requirements lead to one differential equation relating the shock Mach

number, M , and the ray-tube area, A , for each tube. A second relationship between the two quantities is deduced using the CCW theory for the motion of a shock wave down a tube of varying cross section. The resulting equations are of hyperbolic nature and a solution can be deduced using the Method of Characteristics, which also describes the motion of lateral waves on the shock front. These are interpreted as the intersection of acoustic waves with the shock front, and the case where these waves break is termed a "shock-shock" (which is well visualized in the case of Mach reflection).

Another fundamental assumption in Whitham's formulation of the Ray-shock theory is that there is no interaction of any kind between neighboring ray tubes. In some cases, it is more feasible to use a constant averaged value of the Chester function K(M) in the integration of the characteristic relations. In general, however, the results should be treated with some reserve. Apart from the assumptions concerning the shape of fluid motion, the results simulate the kinematics aspects of the shock motion without referring to the motive forces behind it, which are the pressure and momentum fields. Consequently, the results do not give a complete picture of the flow environment.

Due to its multi-dimensional form, the Ray-shock method has been applied successfully to a wide variety of shock dynamics problems. For the cylindrical converging shock in the radial-tangential plane, it has become possible to perform more accurate studies on the effect of circumferential perturbations of irregular nature on the shock advance and eventual collapse [34,40].

Although cumbersome in use and not flexible with complicated geometries, graphical methods of Geometrical Shock Dynamics have proven to be accurate enough due to their analytical basis. This is why they remained the mainstay for scientific research in the field of shock wave dynamics until the advent of modern computers.

1.2 - Experimental Methods

Considerable efforts were made to investigate the converging shock stability experimentally, to obtain test data in order to verify theoretical or numerical trials and to reach empirical relations defining the basic parameters affecting the process. Initial trials relied on creating imploding cylindrical shock waves using outer rim explosions in solid chambers. To this day, improvements in lab technology are bringing up new ideas for the process [28-30]. However, these methods are prone to technical difficulties as well as the impossibility to ensure axial symmetry for the generated waves. A simpler method relied on reflecting originally plane shock waves using specially designed surfaces to create implosions [31-34]. The method has the disadvantage of incomplete one-dimensionality of the resulting shock, except using large dimensions.

Attention was then shifted towards using the conventional shock tube creating an easily obtained plane shock, and then reflecting it using a multiple-conical surface to form the required cylindrical converging one. This technique was pioneered by Perry and

Kantrowitz [35] using the "teardrop" design shown in Fig.(1.1) . It was later used, with differences in the apparatus, by Knystautus and Lee [36] for relatively weak shocks, as well as Takayama et al. [41] and Watanabe et al. [42]. It has been observed that for weak shocks, the transverse pressure waves are able to regain the symmetrical shape of the shock provided it did not reach the self-propagation stage. The design, shown in Fig.(1.2), gives the generated shock more ability for transverse signals to retain the shock's plane shape before conical reflection.

Wu et al. [37-39] and Neemeh et al. [40,67] used a new setup which relied on splitting the initially plane shock into an inner cylindrical core, which is removed, and an annular part which is kept and reflected into a cylindrical converging shock. The time required to form a stable annular shock becomes very small depending on the sharpness of the splitter section. Although a considerable improvement was obtained in the quality of generated shocks, it was not possible to maintain their cylindrical symmetry near the geometric center. Recent research work in the Concordia shock wave dynamics lab aims at correcting this problem using non-uniform bleed effect [69,70].

Reliable experimental work, however, should be tackled with care and, whenever possible, it should be used only for validating numerical or analytical studies. In the present work, attention is directed towards studying the bleed effect on the propagation of strong plane and converging shock waves using less expensive numerical techniques, augmented by experimental verification to gain more insight into the physical details of the problem.

1.3 - Numerical Methods

Numerical methods were proven to be a viable tool to produce results with minimum cost in solving the problem of unsteady compressible flow. It was evident from the beginning that the governing equations for fluid flow have no exact solutions except for special cases with simple geometries, limited dimensions or gross simplifying assumptions. In view of the facts also mentioned above pertaining to requirements for experimental methods, the cost-effectiveness of numerical techniques stands today beyond doubt.

On the other hand, the rapid development of high-speed, high-capacity computers facilitates the numerical handling of problems with complicated geometries using fine and boundary-conforming grids. This, in turn, facilitates getting repeatable answers, with the ability to change parameters independently at marginal increase in cost.

The numerical simulation of cylindrical converging shocks has been pioneered by Payne [43] using the Lax finite difference scheme. Part of the current numerical studies is directed towards using a 1-D set of equations to solve the implosion problem in an ideal or real gas but with more detailed simulation of related physical processes, while dispensing with multi-dimensionality and its related problems [44,46,47]. Furthermore, two-dimensional cases for convergence of shock waves in the radial-tangential plane have also been simulated [45,48-52,68,72]. The main issue has been the evolution of the inherent

instabilities as a function of the geometry and the nature of shock front disturbances. The results obtained showed the anticipated rise in pressure and temperature as well as the dominating onset of instability for the initiated perturbation modes at small radii, leading to the eventual collapse and formation of vortex pairs at the center.

1.4 - Shock Bleed Control

In view of the importance of shock wave effects in structural and industrial applications, there is an ever-growing interest in simulation and measurement of the interaction, particularly the loading nature, of shock or blast waves with obstacles and structures.

As a first example, the spillage and subsequent ignition of combustible gases present a major problem to the engineer concerning the ability of the surrounding structures to survive a catastrophic explosion. Consequently, the design process of gas lines or industrial plants should incorporate practical methods of dissipating shock waves, which may be generated either regularly or accidentally. Designing blast-resistant structures or keeping a proper distance away from explosion sources can lead to a considerable damage reduction. This question arises while choosing the locations of gas processing facilities relative to loading facilities, storage sites as well as population centers.

Attention has also been focused on the inverse problem, that is, the modification and optimization of blast and shock waves by various structures and obstacles. This topic falls into the aspect of gas dynamics, called "shock wave interactions". For example, in the internal combustion engine mufflers, proper adjustment of shock wave synchronization improves the charging volumetric efficiency of the engine (through a better expulsion of exhaust gases from the cylinders) beside reducing the noise levels, thus improving engine performance. For the gun muzzle brake design, the shock diffraction should be optimized to reduce the noise level and also to contain and reverse the resulting flow behind the shock. The optimum design reduces the recoil force and, if applicable, facilitates using the combustion gases to re-arm the weapon.

To date, most of the work on shock control has been focused on attenuation of traveling plane waves moving through ducts. The simple solution of duct area increase is not practical for strong shocks or attenuation requirements along a small distance. One method for shock attenuation is to reflect the wave by placing obstacles in its path. Examples of used obstacles include cylinders, grids, perforated barriers, orifice plates and similar objects. Another method, which receives considerable attention today, examines the duct shock attenuation by creating particle-gas mixtures, triggered before or by the shock, to absorb the kinetic energy of the gas. The disturbances are then communicated forward to the traveling shocks to cause attenuation. This requires the solution of the two-phase media equations for gas and dust suspensions [53].

The third method, which is adopted in the present study, focuses on the attenuation of shocks by bleeding mass, and thus momentum and energy using wall slits or perforations. Expansion waves are generated by the bleeding of fluid through the perforations, which then overtake and gradually weaken the traveling shock.

1.4.1 - Shock Diffraction and Reflection Processes :

Provided that interactions in the third-dimension are omitted, a fair judgment for the performance of fluid bleeding methods needs an accurate analysis of the simple 2-D shock-slit interaction. A simplified description for the stages of that interaction have been given previously [64] for plane shocks where the flow behind the incident shock is subsonic (Fig.(1.3)) or supersonic (Fig.(1.4)). However, in the present case the emphasis will be on supersonic flow behind strong shocks. Initially, the planar shock is diffracted as it exceeds the upstream edge into the slit, so the shock curves around the opening to maintain contact with the wall. At the same time, a series of cylindrical expansion waves is generated at the upstream edge of the slit as the fluid passes by. As time progresses, these waves spread out into the channel and are responsible for the attenuation of the shock. Since the flow behind the shock is taken to be supersonic, the acoustic waves will remain enveloped by the first characteristic line in the expansion fan. Furthermore, since there is no characteristic length involved, this initial stage of the interaction is self-similar, the configuration remains but with a time-expanding scale.

The later insertion of the downstream edge of the slit into the problem introduces a characteristic length (the slit width) and the self-similar nature of the flow is no longer valid. In physical terms, this is accomplished by the reflection of the diffracting shock at the downstream edge, which produces a Mach stem (the new shock) as well as a reflected shock spreading out into the flow. This compression wave, which is also nearly cylindrical, then terminates the initial expansion and tends to reduce the attenuation of the main shock. It is interesting to note that in the case of subsonic particle flow, the secondary shock progresses upstream and eventually collides with the opposite (upstream) edge of the slit to produce a third shock which then moves downstream to collide with the downstream edge (Fig.(1.3)). This reflection process continues until the colliding waves become so weak that the motion is entirely acoustic. However, if the flow is still supersonic after the initial shock, then the secondary shock will remain attached to the downstream edge while propagating across the channel as well as the outer region. If the downstream edge is not sharp, the shock will be slightly detached from the edge - according to the flow situation - and this will trigger expansion zones for the fluid to catch up with the original waves outside the channel.

Experiments indicate that the reflection of the diffracting shock is a Mach reflection, i.e. a three shock configuration with a Mach stem normal to the duct wall at its foot. Although there is no reason to put this assumption as a general case, the present work focuses on strong shocks (i.e. small downstream edge reflection angles), and only the Mach reflection case will be considered. The initiated Mach stem is later transformed into the attenuated

wave, and since the stem lags behind the undisturbed portion of the main shock, significant shock curvature is exhibited in the vicinity of the triple point. The generated expansion and compression waves continue to affect the flow inside the duct through their interactions as well as multiple reflections at the walls. Signals emanating from the processes are transferred to the main shock along characteristic lines.

After some time, the internal attenuated shock moves far downstream and regains its plane shape due to transverse wave reflections. At the slit zone, the wave configuration inside the duct approaches a steady state, with the internal flow characterized by the waves described earlier. Outside, the external expanding shock waves move far away from the slit zone and their influence is no longer present. A steady inclined fluid jet is established at the slit, with jet structure depending on the pressure ratio across the slit as well as the flow velocity behind the shock. For the case when the particle velocity behind the incident shock is supersonic, a Prandtl-Meyer expansion exists at the upstream edge of the slit and a slightly detached shock exists at the downstream edge, as shown in Fig.(1.4c). The jet structure is quite complex due to the reflection of the detached shock from the jet boundary.

Furthermore, for a confined shock problem, like shock waves in ducts, both the expansion wave and secondary (reflected) shock will undergo multiple reflections from the walls of the tube as the main shock propagates down the tube. Thus the attenuation, measured at the wall containing the slit, will proceed in cyclic form corresponding to the arrival of the

reflected waves at the wall. Furthermore, the frequency of the reflections, and hence the attenuation rate, will depend upon the width of the duct. In practical cases, multiple slits would provide more efficient attenuation and this effect would become secondary (as in the case of perforated walls).

In general, shock wave attenuation is a complex process and since the equations which describe shock wave dynamics are nonlinear, there are no simple solutions to this type of problems. Apart from the natural tendency of waves to attenuate due to area divergence effects, the slit bleeding geometry creates a complicated set of shock and expansion waves affecting the shock. To this day, simulation and measurements for the flow field at the diffraction and reflection corners are a challenge to researchers in numerical as well as experimental methods. Multiple reflection of waves from the duct walls provides a more complicated attenuation history with shock or expansion waves traversing the original shock several times before the dissipation of their effects.

For cylindrical converging shocks, specifically at small radii, the problem includes the additional effect of the high rate of area change and the eventual self-propagating state, when the imploding shock evades the effects of the shock structure behind.

1.4.2 - Related Research Work:

In view of today's requirements in industrial and engineering applications, the bulk of research in shock bleed attenuation deals with flows in ducts and similar geometries. Consequently, the schemes are mostly developed for perforated duct flow using quasi-1-D formulation, for which the Method of Characteristics was the most widely used. An important question was how to express the flux terms due to perforations in the governing equations. The earlier scheme developed by Rudinger [54] assumed the fluxes leaving the duct to maintain the same axial momentum as the main stream. A different approach was later adopted by Rosciszewski [55] assuming thick-walled ducts and the jet velocity to be normal to the duct axis, while its value was deduced using Bernoulli's equation. His method was developed using the linearized general form of the quasi-1-D characteristic equations, from which the CCW theory was deduced. The linearization limits application to cases where disturbances in the flow field are relatively small, but the generalized formulation has given it a wider applicability. Experimental measurements have shown good agreement with theory, although the theory was found to predict a more rapid shock decay rate. This has been attributed to errors in evaluation of the mass, momentum and energy flux through the perforations rather than a flaw in the general analysis. Later studies have been directed partly towards updating the formulation the external bleed flux terms [56-59].

A general analysis of shock bounded flows with mass, momentum and energy transfer has been presented recently by Frolov [60]. In his paper, the author has tried different methods of shock wave attenuation for quasi-1-D configuration and compared the output with experimental results. The author has concluded that the proper method for shock wave attenuation depends on the available geometrical space and the required attenuation amount. A nomograph has been supplied to define zones of relative efficiency for different methods in the (M , X) diagram, where M is the Mach number and X is a non-dimensional axial coordinate whose definition depends on the method used. A set of empirical formulae have been obtained for different methods, with an error margin claimed to be less than 5% over the Mach number range between 1.01 and 4.

Later work by Wu et al. [63] and Lee et al. [65] used the Ray-shock Theory, with experimental back-up, to study the 2-D shock bleeding through a single transverse slit for shock Mach numbers producing both subsonic and supersonic flow behind the shock. They have concluded that the single slit attenuation is relatively weak (with a maximum value of about 7% for the largest slit tested) and sensitive to the change in channel width (controlling the lateral reflection frequency) rather than the change in slit width. Thus they concluded that for an effective shock attenuation, multiple-slit bleeding would be the proper method.

However, single slit attenuation continued as an interesting topic for researchers in the field of cylindrical converging shocks. Due to the encountered stability problems, side

bleeding has arisen as an option for controlling the shock speed. A more detailed single slit bleed analysis was required since the available distance - through which attenuation is required - is relatively small. The accelerating radial effect further reduces the travel time, thus rendering a detailed study of bleeding process more crucial for optimizing the experimental procedure. Initial research by Wu et al. [66] dealt with bleeding through a localized aperture to study the transverse diffusion of the bleed effect along the shock front. They concluded that the perturbation tends to die out at large radii and then it is intensified at smaller radii, thus introducing the bleed radial location as an important factor in defining the relative efficiency of stabilizing the front shape.

Later work by Neemeh [67] used bleeding for the different purpose of isolating the effect of the boundary layer from that of the chamber geometry. This was done by splitting the converging shock into two parts using an adjustable disk, thus keeping one part in a cylindrical chamber with a controllable width, while keeping the initial shock conditions invariable.

The recent studies have focused on the effect of all-perimeter bleed on the stability of converging shock waves. The sudden bleed and expansion in flow area slow down the shock wave and provide an opportunity for transverse signal propagation to bring the contour back to its original shape. For a distorted wave front, non-uniform bleed can facilitate regaining the original circular front shape and maintain it until smaller radii.

Amirfazli [68] developed a finite difference operator-splitting code to simulate the front shape development of a 2-D imploding shock in the radial-tangential plane. The initial solution of an elliptic shock front was taken from experimental results of a converging shock after undergoing a non-uniform bleed. The results depicted a tendency to maintain the shock front until the center where breakdown takes place, and agreed with experimental results showing a complex shape of perturbation for elliptic waves. however, this treatment precludes the detailed simulation of the bleeding process and the effect of shock reshaping in the axial direction, whose nature and frequency have a significant effect on the developing shock front.

Tashtoush [69,70] experimentally studied the effect of non-uniform bleed on the shock propagation and stability as well as the vortices formed at the center behind the reflected shock. The study has indicated the incremental effect of increasing the chamber width (which means reducing the reflection frequency) on the shock's rate of recovery. Another conclusion was the technique's ability of bringing distorted cylindrical shock fronts back to their required shape. This is done by aligning the non-uniform bleed geometry to cope with the observed departure from circular geometry, and slowing the faster portion of the shock front. In part of his work, Tashtoush used the Ray-shock Theory to predict the effect of variable bleed on the wave propagation. Bleed non-uniformity was represented by dividing the domain in the tangential direction into segments and solving each one independently using graphical methods in a 2-D Cartesian formulation (for radial-axial coordinates). The above mentioned scheme works efficiently at large radii, where the

radial effect is minimal. At small radii, however, the area rate of change is too significant to be ignored. Besides, the kinematics-oriented CCW theory and the absence of lateral interaction considerably reduce the applicability of the solution.

1.4.3 -Objective of the Present Work :

The ultimate goal is to be able to perform a complete parametric study on the shock convergence in fully 3-D domain to simulate both shock bleeding and lateral instability. One suitable method for doing so is to develop a 3-D Euler numerical code which represents the full flow field rather than the kinematics of the shock motion.

For the time being, the mandate of the present work is to perform a parametric study for cylindrical converging shock-slit interaction in the radial-axial plane, covering the whole convergence history, including the bleeding stage with its associated diffraction and reflection phenomena. In addition to complementing the previous work, the present work's generic 3-D code facilitates including the transverse (tangential) direction at a later stage, thus covering the complete domain once computing facilities are available.

As an introductory step for studying cylindrical shock attenuation, the first stage deals with studying the purely 2-D shock-slit interaction. The purpose of this stage is fourfold. The first is to validate the numerical code against well-established benchmark test cases. The second is to be able to visualize the expected shock structure due to bleeding. The

third is to calculate the anticipated attenuation behavior without the radial convergence effect. The last is to utilize the availability of better measuring instruments and analytical results for re-evaluating the previously concluded trends [64]. Results will be presented in terms of the system parameters, basically the initial shock Mach number and the slit-chamber width ratio. The second phase tackles the analysis of similar geometries in the axisymmetric plane to investigate the effect of frontal area contraction.

Attention is paid to the numerical simulation of the problem, and it will be shown that the Finite Element Method provides an adequate description of the fluid flow cases. As the theoretical basis, the Euler equations are chosen as they form the simplest approach and still give a reliable overview for the wave motion in the fluid. The energy equation is written in a new form to introduce the pressure as a convected variable. With pressure and density as variables, the results are easily compared to Schlieren photographs and pressure transducer outputs. Although Euler equations assume the working fluid to be inviscid and perfect, they have been used successfully to describe this category of problems, and it will be shown later in the discussion that the model is adequate for the present purposes.

Because of the complexity of flow phenomena associated with the shock-slit interaction, experimental work is needed to validate the numerical handling. Two types of shock tubes are used for the study. For the 2-D tests, a simple air/air shock tube with a square cross section is employed to cover the practical range of shock Mach numbers up to about 2.5, thus covering the regime where supersonic flow exists behind the incident shock. For the

cylindrical converging flow cases, a 6" inner diameter cylindrical shock tube is used to create converging shocks. To cover strong shocks, a new test section was designed to extend the Mach number range by inward bleeding into the vacuumed driven section.

The theoretical background of the plane and cylindrical converging shock wave analysis is presented in Chapter 2. This includes the governing equations, the analytical methods developed for one- and multi-dimensional treatments, as well as their application to the basic processes of diffraction and Mach reflection. The Finite Element formulation and derivations are presented in Chapter 3, together with the solution techniques and means of implementing boundary conditions. In Chapter 4, the experimental setups for plane and cylindrical shock testing, as well as their monitoring instruments, are described in detail. Chapter 5 is dedicated to presenting and discussing the results for plane and cylindrical converging shock bleeding, as well as the necessary benchmark problems for numerical code validation. Finally, Chapter 6 includes the conclusions and recommendations for future work.

2 - THEORETICAL BACKGROUND

For control volume-based schemes, like the FEM and the FVM, the conservative form is the most suitable formulation because it represents the local rate of accumulation of convected variables, as well as their convective fluxes across the boundaries. It is also useful for flow description in the vicinity of shock waves, across which the exact rates of change can not be easily defined while the total variations can be calculated using conservation laws.

2.1 - Alternative Formulations for Euler Equations

The governing equations for 3-D unsteady inviscid compressible gas, without heat conduction or chemical reaction, are loosely known as Euler equations. The conservation formulation is written as follows :

Mass :
$$\frac{\partial \rho}{\partial t} + \underline{\nabla} . (\rho \underline{V}) = 0 \qquad (2.1a)$$

X - Momentum :
$$\frac{\partial (\rho u)}{\partial t} + \underline{\nabla} . (\rho \underline{V} u) = - \frac{\partial p}{\partial x} \qquad (2.1b)$$

Y - Momentum :
$$\frac{\partial (\rho v)}{\partial t} + \underline{\nabla} . (\rho \underline{V} v) = - \frac{\partial p}{\partial y} \qquad (2.1c)$$

Z - Momentum :
$$\frac{\partial (\rho w)}{\partial t} + \underline{\nabla} . (\rho \underline{V} w) = - \frac{\partial p}{\partial z} \qquad (2.1d)$$

Energy :
$$\frac{\partial(\rho e_t)}{\partial t} + \underline{\nabla}.(\rho \underline{V} e_t + \underline{V} p) = 0 \qquad (2.1e)$$

where the variables are (ρ , $\rho \underline{V}$, e_t , p), where $e_t = C_v T + \frac{1}{2}|\underline{V}|^2$ is the total internal energy / unit mass , incorporating the kinetic energy. To complement the abovementioned set, the equation of state is added for a perfect gas:

$$p = \rho R T \qquad (2.2)$$

The set written above is in terms of Cartesian coordinates, which are suitable for geometries of the 2-D cases in the present study. The equations can be rewritten in different ways depending on the problem geometry, the chosen set of variables and the associated boundary conditions. For the energy equation, another form can be deduced leaving only the static instead of the total internal energy. The momentum equation in non-conservative vector form can be written as :

$$\frac{\partial \underline{V}}{\partial t} + (\underline{V}.\underline{\nabla})\,\underline{V} = -\frac{1}{\rho}\underline{\nabla} p \qquad \text{or}$$

$$\frac{D\underline{V}}{Dt} = -\frac{1}{\rho}\underline{\nabla} p \qquad (2.3)$$

After scalar multiplication by the velocity vector, the equation is recast as :

$$\rho \frac{D}{Dt}\left(\frac{|\underline{V}|^2}{2}\right) = -\underline{V}.\underline{\nabla} p \qquad (2.4)$$

Subtracting this streamwise line integral from the non-conservative total energy equation will result in the modified form. Using the equalities :

$$p = (\gamma - 1)\rho e \quad , \quad p(\underline{\nabla}.\underline{V}) = \underline{\nabla}.(\underline{V} p) - \underline{\nabla} p.\underline{V}$$

and adding the continuity equation again, the conservative equation becomes :

$$\frac{\partial(\rho e)}{\partial t} + \underline{\nabla}.(\underline{V}\rho e) = -p(\underline{\nabla}.\underline{V}) \qquad (2.5)$$

Introducing the pressure (p) leads to the final form :

$$\frac{\partial p}{\partial t} + \underline{\nabla}.(\gamma \underline{V} p) = (\gamma - 1)\underline{\nabla} p.\underline{V} \qquad (2.6)$$

where the variables then are (ρ , $\rho\underline{V}$, p). This form has the advantage of introducing the pressure as the convected variable, and simplifying the linearization processes in case they are needed. The newly-emerging non-divergence term can be considered as an internal energy source (actually it represents the work done by the pressure gradient force inside the control volume).

A third form for the energy equation can be deduced applying the first and second laws of thermodynamics. Consider the non-conservative continuity and energy equations :

$$T\frac{Ds}{Dt} = p\frac{D}{Dt}\left(\frac{1}{\rho}\right) + \frac{De}{Dt} = \frac{p}{\rho}\left(\underline{\nabla}.\underline{V}\right) + \frac{De}{Dt} = 0 \qquad (2.7)$$

This means that the material derivative for entropy is zero. Thus entropy is conserved along the particle path unless the particle is subject to a physical entropy-generating process (e.g., a shock wave).

2.2 - One-Dimensional Formulation

In view of the mathematically complicated nature of the equations governing fluid flow, it was inevitable that initial trials for handling shock wave propagation relied on the simple 1-D formulation. The domain of applications covers phenomena where the effect of irregularities is small compared to the otherwise-1-D computation domain (e.g., shock flows in straight ducts with perforations, cylindrical and spherical implosions, nuclear explosion shock waves.....etc.). Dispensing with the multi-dimensionality enabled researchers either to simulate other physical aspects of the flow and introduce the necessary minimum assumptions for obtaining closed form solutions [e.g., 10-19].

2.2.1 - The Method of Characteristics :

For the present problem of converging shock waves, the initial trials were performed analytically assuming only radial velocity component. The one-dimensional set of equations is written in non-conservative form as :

Continuity :
$$\frac{\partial \rho}{\partial t} + v_r \frac{\partial \rho}{\partial r} + \rho \frac{\partial v_r}{\partial r} + \rho \frac{v_r}{r} = 0 \qquad (2.8a)$$

Radial Momentum :
$$\frac{\partial v_r}{\partial t} + v_r \frac{\partial v_r}{\partial r} + \frac{1}{\rho} \frac{\partial p}{\partial r} = 0 \qquad (2.8b)$$

Energy :
$$\frac{\partial s}{\partial t} + v_r \frac{\partial s}{\partial r} = 0 \qquad \text{or}$$

$$\frac{\partial p}{\partial t} + v_r \frac{\partial p}{\partial r} - c^2 \left(\frac{\partial \rho}{\partial t} + v_r \frac{\partial \rho}{\partial r} \right) = 0 \qquad (2.8c)$$

Where the local speed of sound $c = \sqrt{\frac{\gamma p}{\rho}}$. Modifying the energy equation to include one time derivative, the set can be written in the form :

$$\frac{\partial \underline{U}}{\partial t} + [J] \frac{\partial \underline{U}}{\partial r} = \underline{S}(\underline{U}) \qquad (2.9)$$

$$\underline{U} = \begin{Bmatrix} \rho \\ v_r \\ p \end{Bmatrix} \quad , \quad \underline{S}(\underline{U}) = \begin{Bmatrix} -\rho v_r / r \\ 0 \\ -c^2 \rho v_r / r \end{Bmatrix} \quad , \quad [J] = \begin{bmatrix} v_r & \rho & 0 \\ 0 & v_r & \frac{1}{\rho} \\ 0 & c^2 \rho & v_r \end{bmatrix}$$

The eigenvalues of the Jacobean matrix are calculated using the determinant of the matrix $[J - \lambda I]$ where λ is the eigenvalue diagonal matrix. The results are three different real values :

$$\frac{dr}{dt} = v_r \quad , \quad v_r + c \quad , \quad v_r - c \tag{2.10}$$

Thus the system of equations is hyperbolic and a set of characteristics can be defined for signal propagation in the (r , t) plane. In case the energy equation is written in terms of entropy as the convected variable, it will be self-sufficient for defining its own characteristic line of entropy conservation (the particle path, which is moving with a speed equal to particle speed in the position-time space). In the present case pressure was introduced since it is intended to be used in the coming work. Lagrange multipliers can be used to define the associated eigenvectors, equations and variables:

$$\frac{\partial p}{\partial t} + v_r \frac{\partial p}{\partial r} + c^2 \left(\rho \frac{\partial v_r}{\partial r} + \rho \frac{v_r}{r} \right) + \lambda_1 \left(\frac{\partial v_r}{\partial t} + v_r \frac{\partial v_r}{\partial r} + \frac{1}{\rho} \frac{\partial p}{\partial r} \right)$$

$$+ \lambda_2 \left(\frac{\partial \rho}{\partial t} + v_r \frac{\partial \rho}{\partial r} + \rho \frac{\partial v_r}{\partial r} + \rho \frac{v_r}{r} \right) = 0 \tag{2.11}$$

re-arranging terms in operator form :

$$\left[\frac{\partial}{\partial t}+(v_r+\lambda_1\frac{1}{\rho})\frac{\partial}{\partial r}\right]p+\left[\lambda_1\frac{\partial}{\partial t}+(\lambda_1 v_r+c^2\rho+\lambda_2\rho)\frac{\partial}{\partial r}\right]v_r+$$

$$\left[\lambda_2\frac{\partial}{\partial t}+(\lambda_2 v_r)\frac{\partial}{\partial r}\right]\rho+\left[\lambda_2\rho\frac{v_r}{r}+c^2\rho\frac{v_r}{r}\right]=0 \qquad (2.12)$$

To have an exact differential along a certain characteristic line in the (r , t) plane, the differential operator should have the same proportions.

$$\therefore \qquad v_r+\lambda_1\frac{1}{\rho} = \frac{\lambda_1 v_r+c^2\rho+\lambda_2\rho}{\lambda_1} = v_r$$

The first possible solution is that $\lambda_1 = 0$, $\lambda_2 = -c^2$ which leads to the exclusion of the momentum equation and repetition of the energy equation in the conserved entropy form. To avoid this trivial case, the density derivative terms should be canceled out.

$$\left[\frac{\partial}{\partial t}+(v_r+\lambda_1\frac{1}{\rho})\frac{\partial}{\partial r}\right]p+\left[\lambda_1\frac{\partial}{\partial t}+(\lambda_1 v_r+c^2\rho)\frac{\partial}{\partial r}\right]v_r+\left[c^2\rho\frac{v_r}{r}\right]=0$$

$$\Rightarrow \qquad v_r+\lambda_1\frac{1}{\rho} = \frac{\lambda_1 v_r+c^2\rho}{\lambda_1} \quad \text{or} \quad v_r\lambda_1+\lambda_1^2\frac{1}{\rho} = \lambda_1 v_r+c^2\rho$$

$$\therefore \qquad \lambda_1^2 = c^2\rho^2 \quad \text{or} \quad \lambda_1 = \pm c\rho \qquad (2.13)$$

Substituting in the operator equation :

$$\left[\frac{\partial}{\partial t} + (v_r \pm c) \frac{\partial}{\partial r} \right] p \pm \rho c \left[\frac{\partial}{\partial t} + (v_r \pm c) \frac{\partial}{\partial r} \right] v_r + \left[c^2 \rho \frac{v_r}{r} \right] = 0$$

It is possible to rewrite the previous equation in terms of a defined total derivative w.r.t. time along the characteristics in the (r , t) plane. Defining the operators:

$$\frac{D^{\pm}}{Dt} = \frac{\partial}{\partial t} + (v_r \pm c) \frac{\partial}{\partial r}$$

along the characteristics $\mathbf{C^{\pm}}$: $\frac{dr}{dt} = v_r \pm c$. The equations become :

$$\frac{D^{\pm}}{Dt} p \pm \rho c \frac{D^{\pm}}{Dt} v_r + \left[c^2 \rho \frac{v_r}{r} \right] = 0 \qquad (2.14a,b)$$

along the characteristic $\mathbf{P}$: $\frac{dr}{dt} = v_r$. The entropy equation is satisfied :

$$\frac{Ds}{Dt} = 0 \qquad (2.14c)$$

As a special case, the isentropic flow region may be considered. In this case, the pressure may be expressed as a function of only the density.

$$c^2 = \gamma \frac{p}{\rho} = \gamma \frac{p}{p^{1/\gamma}} k \quad \Rightarrow \quad \frac{2dc}{c} = \frac{\gamma - 1}{\gamma} \frac{dp}{p} = \frac{\gamma - 1}{\rho c} dp$$

$$\Rightarrow \quad \frac{2\rho c}{\gamma - 1} \frac{D^{\pm}}{Dt} c \pm \rho c \frac{D^{\pm}}{Dt} v_r + \left[c^2 \rho \frac{v_r}{r} \right] = 0$$

$$\therefore \quad \frac{D^{\pm}}{Dt} \left[\frac{2}{\gamma - 1} c \pm v_r \right] + \left[c \frac{v_r}{r} \right] = 0 \qquad (2.15a,b)$$

where the quantities $\frac{2}{\gamma - 1} c \pm v_r$ are called the Riemann variables.

The equations are used for solution advancing in time steps to solve for radial velocity and thermodynamic state variables. This is supposed to be done graphically on a plane representing the radius-time space. the domain is divided into nodes and an iterative procedure is performed to adjust both the characteristic variables and the characteristic lines passing by each node in terms of the previous value distribution.

However, contrary to the case of Cartesian formulation for plane waves, the extra algebraic term in the case of cylindrical converging waves renders the tracing process impractical since no conserved variable is well defined along the first two characteristics.

2.2.2 - Self-Similar Solutions :

The self-similarity principle provided another simple, yet cost-effective, technique which was incorporated for the solution of one- or multi-dimensional equations. The similarity

methods are used in case the problem has no fixed characteristic length. The technique facilitates transforming the governing P.D.E.s to simpler ones, or even O.D.E.s, in terms of a time-dependent expanding (or contracting) set of coordinates, thus reducing their complexity. The coordinate time relationship is assumed to take the general form of a power law.

The method has achieved success in the case of point explosion with the following two assumptions : very strong shocks ($M^2 >> 1$), and a dimensional argument that results depend on the amount of energy released at the center as well as the density of the stagnant medium ahead of the shock front. The Rankine-Hugoniot relations were modified accordingly to express the pressure, velocity and density in terms of the shock speed. The balancing of units led to the calculation of the exponent (n) value equal to 2/5 for the shock radius-time relationship being in the form.

$$R(t) = \text{shock radius at time } t \;=\; k\left(\frac{E}{\rho_0}\right)^{n/2} t^n \;=\; k\left(\frac{E}{\rho_0}\right)^{1/5} t^{2/5} \qquad (2.16)$$

where k is a non-dimensional constant.

For the implosion problem, there was no similar dimensional argument to define the value for such a power law exponent. However, the power law assumption was adopted by

Guderley [10] for the shock radius-time relationship. Defining the set of dimensionless variables :

$$\xi = \frac{r}{R(t)} \qquad \text{where} \quad R(t) = \text{shock radius at time } t = (K\,t)^n$$

$$v_r = n\frac{r}{t}V(\xi) \quad , \quad c = n\frac{r}{t}C(\xi)$$

$$\rho = \rho_0\,\Omega(\xi) \quad , \quad p = n^2\rho_0\,\frac{r^2}{t^2}\,P(\xi)$$

$$\therefore \quad C = \sqrt{\frac{\gamma P}{\Omega}}$$

The partial derivatives are modified in terms of the new variable

$$\frac{\partial}{\partial t} = \frac{\partial}{\partial \xi}\frac{\partial \xi}{\partial t} = -n\frac{r}{t}\frac{\partial}{\partial \xi} \quad , \quad \frac{\partial}{\partial r} = \frac{\partial}{\partial \xi}\frac{\partial \xi}{\partial r} = \frac{\xi}{r}\frac{\partial}{\partial \xi}$$

Introducing these modifications, the one-dimensional set of equations can be re-written in terms of the new set of variables, and the original partial differential equations (in terms of dimensional physical variables) are transformed into a new set of ordinary differential equations which can be solved independently.

$$\left\{(V-1)^2 - C^2\right\}\xi\frac{dV}{d\xi} = \left\{2V - \frac{2(1-n)}{n\gamma}\right\}C^2 - V(V-1)\left(V - \frac{1}{n}\right) \qquad (2.17a)$$

$$\left\{(V-1)^2-C^2\right\}\frac{\xi}{C}\frac{dC}{d\xi} = \left\{1-\frac{(1-n)}{n\gamma}(V-1)^{-1}\right\}C^2+\frac{\gamma-1}{2}V\left(V-\frac{1}{n}\right)$$

$$-(\gamma-1)\,V\,(V-1)-(V-1)\left(V-\frac{1}{n}\right) \qquad (2.17b)$$

$$\left\{(V-1)^2-C^2\right\}\frac{\xi}{\Omega}\frac{d\Omega}{d\xi} = 2\left\{2U-\frac{(1-n)}{n\gamma}\right\}(V-1)^{-1}\,C^2-V\left(V-\frac{1}{n}\right)$$

$$-2\,V\,(V-1) \qquad (2.17c)$$

Where U is the non-dimensional shock speed. The set is integrated between the limits $\xi=\infty$ (inlet) and $\xi=1$ (shock) with the Rankine-Hugoniot relations forming the boundary conditions at shock location. There is a clear singularity when $V\pm C=1$, which agrees with the fact that all singularities must happen on the family of characteristics

$$\frac{dr}{dt}=v_r\pm c = n\frac{r}{t}(V\pm C) \qquad (2.18)$$

Thus the limiting member along which the singularity can occur is the one passing by the origin of the (r , t) plane.

$$V\pm C=1 \quad\Rightarrow\quad \frac{dr}{dt}=n\frac{r}{t} \quad \text{or} \quad r=(Kt)^n \qquad (2.19)$$

which means that the power-law curve becomes a characteristic when approaching the center. However, other than this particular moment the flow is not supposed to have any other singularities, especially if one considers the feedback resulting from the backward-moving characteristics reflecting on the limiting one (Fig.(2.1)). The only way to ensure this is to have the exponent (n) such that the RHS tends to zero when the LHS has the same value. The values of (n) were tabulated for different values of specific heat ratio for both spherical and cylindrical converging shocks [25]. It must be mentioned here that the flow approaches a power-law behavior at small radii. Far from the center, the flow should be treated with the Method of Characteristics and numerical integration.

2.3 - Multi-Dimensional Formulation

Other than perfectly one-dimensional problems, the only cases handled with characteristics were those in which transverse flow adjustments require smaller time scales than those required for advance in the axial direction. Adopting a time-marching scheme in which the solution step - between the successive shock fronts - is small enough to ensure small area increment, the flow can be treated as quasi-one-dimensional. This applies to duct flow problems including small rate area variations. Applying the characteristic relations and Rankine-Hugoniot thermodynamic relations can lead to defining the history of shock propagation as a relation between the area and the Mach number variations along the duct or tube.

Furthermore, similar cases where side bleeding process is used for attenuating shock waves were of major concern for engineering applications related to duct or tube flows. This requires investigators not only to consider the effect of area changes on traveling shocks, but also to examine the more general situation where mass, momentum and energy transfer flux terms exist and influence the shock motion as well, thus providing farther quantitative insight into the continuous bleed problem.

Our interest in the present investigation is confined to the case where no fluxes exist (for the CCW is considered here as an introduction to the Ray-shock Theory, which does not assume cross flow, as will be shown later in this chapter). Besides, the bleed problem studied is due to a single slit only, which precludes the use of continuous flux term treatment.

2.3.1 - Quasi-One-Dimensional Treatment :

Omitting the mass, momentum and energy flux terms on the right side of equations, the quasi-one-dimensional formulae for Euler equations can be written in the form :

Continuity :
$$\frac{\partial \rho}{\partial t} + u\frac{\partial \rho}{\partial x} + \rho\frac{\partial u}{\partial x} + \rho\frac{u}{A}\frac{dA}{dx} = 0 \qquad (2.20a)$$

Momentum :
$$\frac{\partial u}{\partial t} + u\frac{\partial u}{\partial x} + \frac{1}{\rho}\frac{\partial p}{\partial x} = 0 \qquad (2.20b)$$

Energy :

$$\frac{\partial s}{\partial t} + u\frac{\partial s}{\partial x} = 0 \qquad \text{or}$$

$$\frac{\partial p}{\partial t} + u\frac{\partial p}{\partial x} - c^2\left(\frac{\partial \rho}{\partial t} + u\frac{\partial \rho}{\partial x}\right) = 0 \tag{2.20c}$$

or in characteristic form. Along the characteristics $\mathbf{C^{\pm}}: \frac{dx}{dt} = u \pm c$

$$\left[\frac{\partial}{\partial t} + (u \pm c)\frac{\partial}{\partial x}\right] p \pm \rho c\left[\frac{\partial}{\partial t} + (u \pm c)\frac{\partial}{\partial x}\right] u + \left[\rho c^2 u \frac{1}{A}\frac{dA}{dx}\right] = 0$$

(2.21a,b)

while the entropy equation

$$\frac{\partial s}{\partial t} + u\frac{\partial s}{\partial x} = 0 \tag{2.21c}$$

is valid along the particle path $\mathbf{P}: \frac{dx}{dt} = u$

In this case, u is the local velocity in the tube direction and x is the position along the tube axis. The only equation which includes area change is the continuity equation. Across the shock front, the Rankine-Hugoniot relations apply

$$\frac{u_2 - u_1}{a_1} = \frac{2}{\gamma+1}\left[M - \frac{1}{M}\right] \tag{2.22a}$$

$$\frac{p_2}{p_1} = \frac{2\gamma M^2 - (\gamma-1)}{\gamma+1} \tag{2.22b}$$

$$\frac{\rho_2}{\rho_1} = \frac{(\gamma+1)M^2}{2+(\gamma-1)M^2} \tag{2.22c}$$

$$\frac{c_2}{c_1} = \left[\frac{p_2}{p_1}\frac{\rho_1}{\rho_2}\right]^{1/2} \tag{2.22d}$$

where case (1) refers to the state ahead of the shock and case (2) to the state behind the shock. Assuming stagnant conditions ahead of the shock, the particle path and C^- characteristic not affecting the shock, the equation of the C^+ characteristic can be recast in the general form :

$$\frac{dA}{A} = - g(M)\ dM \tag{2.23}$$

The form of the function g (M) reflects the different approaches followed by the early researchers who handled the problem. Chester [20] assumed that the variations at any time station to be small compared to the current flow conditions. So the equations were recast as perturbations superimposed on the previously-uniform tube mean flow. The equations were linearized around the mean flow state and solved explicitly. By integrating each linearized equation along its own characteristic line, the equations take the form :

$$p - p_1 + \rho_1 c_1 (u - u_1) + \frac{\rho_1 c_1^2 u_1}{u_1 + c_1} \frac{A - A_1}{A_1} = F[x - (u_1 + c_1) t] \qquad (2.24a)$$

$$p - p_1 - \rho_1 c_1 (u - u_1) + \frac{\rho_1 c_1^2 u_1}{u_1 - c_1} \frac{A - A_1}{A_1} = G[x - (u_1 - c_1) t] \qquad (2.24b)$$

$$p - p_1 + c_1^2 (\rho - \rho_1) = H[x - u_1 t] \qquad (2.24c)$$

where the functions F , G and H represent the disturbances carried along their respective characteristic lines to reach the point under investigation. Since the C^+ line is the only one capable of carrying signals from the undisturbed region far behind the shock, the function F is identically zero. The other two can be calculated from the local thermodynamic values through the Rankine-Hugoniot relations and their values are conserved along their respective characteristics to interact with other locations at new time stations (Fig.(2.2)). The final result is in the form :

$$\frac{\Delta A}{A} = - \frac{2 M \Delta M}{(M^2 - 1) K(M)} \qquad (2.25)$$

where K(M) is a slowly varying function (from 0.5 at M = 1 to 0.3941 at M $\Rightarrow \infty$) which was named the Chester function (Fig.(2.3)).

$$K(M) = \frac{2}{\lambda(M)} \quad \text{where} \quad \lambda(M) = [1 + \frac{2}{\gamma + 1} \frac{1 - \mu^2}{\mu}] (1 + 2\mu + \frac{1}{M^2}) \quad \text{and}$$

$$\mu^2 = \frac{(\gamma-1)M^2+2}{2\gamma M^2-(\gamma-1)}$$

Chisnel [21] followed a different approach assuming any finite area variation as a sequence of area jumps after each the flow can be treated as steady uniform. The shock undergoes a disturbed transformation while the emanating signals are reflected along the characteristics. These are re-reflected again - after intersecting with previous changes - to overtake the shock and contribute to its behavior. Considering multiple re-reflections was impractical and so one re-reflection was considered. It was found by the researcher that their total contribution to the shock history is negligible. This led to considering Chester's Area-Mach number relationship as the differential form of the real one.

$$\frac{dA}{A} = -\frac{2M\,dM}{(M^2-1)\,K(M)} \qquad \text{or}$$

$$A = A_0 \exp\left(-\int_1 \frac{2M\,dM}{(M^2-1)\,K(M)}\right) \tag{2.24}$$

where the area where M = 1 is taken as the reference area A_0

Whitham [22] followed the more direct approach of assuming that in the (x , t) plane, the shock path and the C^+ characteristic are close enough to be considered as one line. Applying Rankine-Hugoniot equations directly on the equation of the C^+ characteristic,

Whitham obtained the same formula derived by his two predecessors. Because of this, the resulting formula was called after them the CCW relationship.

For high Mach numbers ($M^2 >> 1$) in imploding cylindrical and spherical shocks, the Chester function approaches its asymptotic value and the area-Mach no. relation takes the power law. For cylindrical case :

$$\frac{dR}{R} = \frac{dA}{A} = -\frac{2M\,dM}{(M^2-1)\,K(M)} \equiv -\frac{2M\,dM}{(M^2)\,0.394}$$

$$\therefore \quad \frac{dR}{R} \equiv -\frac{1}{0.197}\frac{dM}{M} \qquad (2.25)$$

2.3.2 - Geometrical Shock Dynamics (Whitham Ray-shock Theory) :

For multi-dimensional cases associated with complicated geometries, the use of the Method of Characteristics in its original form (with the time axis) becomes impractical and different schemes relying on space axes only become a must. For quasi-1-D flows in duct-like paths, the CCW theory has provided a tool relating the local shock Mach number and the local area across which the flow is confined to move. With the moving shock thermodynamic relations incorporated, the new scheme was supposed to provide researchers with the thermodynamic state just behind the shock front and not far beyond.

As an extension to the abovementioned quasi-one-dimensional formulation, Whitham presented a multi-dimensional treatment based on the same derived formulas [23-25]. It is assumed that the solution domain - between the successive shock fronts - is divided into stream tubes. Each tube is bounded by rays in stream line directions as well as the shock fronts (which are assumed to be normal to the rays). In each tube, if the time increment and tube width are small enough, the flow can be considered as quasi-one-dimensional. The CCW theory can predict the alternatives for shock speed versus tube width, while the lateral geometrical compatibility requirements enforces the definition of the new total front shape.

An orthogonal curvilinear set of coordinates was defined to match the two orthogonal families of curves. Along the rays, the axial coordinate ($\alpha = c_0 t$) represents the locations of shock fronts at its contours , where c_0 is the undisturbed speed of sound ahead of the shock. Accordingly the distance traveled by the shock in a time increment dt is $U\,dt = M\,d\alpha$, where (U) is the shock speed and (M) its Mach number. The other coordinate (β) describes the rays as its contours such that the area increment is defined as $dA = A(\alpha,\beta)\,d\beta$, as shown in Fig (2.4).

The P.D.E.s for the new system can be rewritten in terms of the original Cartesian system of coordinates using the proper Jacobean tensor. The geometry of the curvilinear element PQRS shown in Fig (2.4) shows that

$$d\theta = \theta_2 - \theta_1 = \frac{QR - PS}{PQ} = \frac{(A + \frac{\partial A}{\partial \alpha} d\alpha)\, d\beta - A d\beta}{M\, d\alpha}$$

$$\therefore \quad d\theta = \frac{\frac{\partial A}{\partial \alpha} d\alpha\, d\beta}{M\, d\alpha} \qquad \text{or} \qquad \frac{d\theta}{d\beta} = \frac{1}{M} \frac{\partial A}{\partial \alpha} \tag{2.26}$$

A similar derivation leads to the formula relating the angle of the orthogonal contours

$$-d\phi = \frac{(M + \frac{\partial M}{\partial \beta} d\beta)\, d\alpha - M d\alpha}{A\, d\beta}$$

$$\therefore \quad -\frac{d\phi}{d\alpha} = \frac{1}{A} \frac{\partial M}{\partial \beta} \tag{2.27}$$

Since the two families of contour lines tend to be orthogonal, i.e. $d\theta = d\phi$, then

$$\frac{d\theta}{d\beta} - \frac{1}{M} \frac{\partial A}{\partial \alpha} = 0 \quad , \quad \frac{d\theta}{d\alpha} + \frac{1}{A} \frac{\partial M}{\partial \beta} = 0 \tag{2.28}$$

The set of equation is hyperbolic and the characteristic form can be obtained using Lagrange multipliers. Multiplying the first one by λ and adding to the second one

$$\left[\frac{\partial}{\partial \alpha} + \lambda \frac{\partial}{\partial \beta} \right] \theta + \left[-\lambda \frac{1}{M} \frac{dA}{dM} \frac{\partial}{\partial \alpha} + \frac{1}{A} \frac{\partial}{\partial \beta} \right] M = 0 \tag{2.29}$$

It must be noted that in the equation above the A-M derivative is introduced as a total derivative assuming the one-to-one relationship deduced previously and assumed to describe the flow inside the stream tubes. Denoting the A derivative w.r.t. M as A'

$$\frac{dA}{A} = - g(M)\ dM \qquad \Rightarrow \qquad A' = -g(M)\ A \tag{2.30}$$

the existence of characteristic lines implies the uniqueness of the directional derivative operator along them. Then

$$\lambda^2 = \frac{-M}{A'A} \qquad \Rightarrow \qquad \lambda = \frac{d\beta}{d\alpha} = \pm\sqrt{\frac{-M}{AA'}} = \pm C(M) \tag{2.31}$$

The resulting characteristic equations will be

$$\left[\frac{\partial}{\partial\alpha} \pm C\frac{\partial}{\partial\beta}\right]\left[\theta \pm \int\frac{dM}{AC}\right] = 0 \quad \text{or}$$

$$\left[\frac{\partial}{\partial\alpha} \pm C\frac{\partial}{\partial\beta}\right](\theta \pm \omega(M)) = 0 \tag{2.32}$$

Since the integral $\omega(M)$ in the above equation is a function of M only, its values - as well as those of the characteristic angle $m = \tan^{-1}(C(M))$ - are tabulated to be used in the

solution for the advancing shock fronts in two-dimensional problems. For using Cartesian coordinates the transformation is easy to visualize and the characteristic directions

$$\frac{d\beta}{d\alpha} = \pm C(M) = \pm \tan(m) \tag{2.33}$$

are recast as the formulation

$$\frac{dy}{dx} = \tan(\theta \pm m) \tag{2.34}$$

For practical applications, the value of the Chester function K(M) are taken as equal to a constant mean value depending on the Mach number range of operations. Consequently the value of the characteristic angle (m) can be deduced as a direct function of the Mach number. Defining the parameter (n) as 2 / K(M), the equation (2.24) is rewritten as

$$\frac{dA}{A} = -\frac{2M\,dM}{(M^2-1)\,K(M)} = -\frac{n\,M\,dM}{(M^2-1)} \quad \text{or}$$

$$\frac{A}{A_0} = \left[\frac{M_0^{\,2}-1}{M^2-1}\right]^{\frac{1}{K}} \tag{2.35}$$

where A_0 (taken usually as 1) and M_0 are the undisturbed reference values. Going back to the relations of the angle (m) and the integral (ω),

$$\tan(m) = \frac{d\beta}{d\alpha} = \pm\sqrt{\frac{-M}{AA'}} = \pm\frac{1}{M}\sqrt{\frac{M^2-1}{n}} \qquad (2.36)$$

$$\omega(M) = \int\frac{dM}{AC} = \sqrt{n}\int_{M_0}^{M}\frac{dM}{\sqrt{M^2-1}} = \sqrt{n}\,(\cosh^{-1}M - \cosh^{-1}M_0) \qquad (2.37)$$

As mentioned before, the Ray-shock Theory has its limitations concerning the location and quality of results obtained, in addition to the cumbersome calculation procedure. The approximation above can not be considered as reliable for weak shocks with large Mach number variations or large diffraction angles (since the constant function K assumption will not be suitable). In problems including flows in the radial-axial plane, the scheme should be modified for considering the width of flow area in the tangential direction, which is proportional to the radius. This means that solutions based on the abovementioned derivation are reliable only at large radii.

2.4 - Application to Shock Diffraction and Mach Reflection

Interaction of an initially plane shock with both concave and convex corners has been examined by several authors both analytically and experimentally. In the present section, we present a brief discussion for the application of the Ray-shock Theory for the two basic events.

For the case of diffraction at a convex corner, the result is the simple expansion fan comprising one family of characteristics. Considering the sharp edge as a concentration of simple finite angle diffractions, The straight, radial lines will be centered at the corner, as shown in Fig.(2.5). Each characteristic carries constant values of the diffraction angle and its associated Mach number, and corresponds to the appearance of acoustic waves which spread out and perform the modification of the shock. In fact, the characteristic lines are just the paths of the intersection of each acoustic wave with the shock. The head characteristic line is associated with the initial (undisturbed) shock Mach number according to the above equation (2.33).

The shock shape can be calculated by integration along characteristics and the shock or along rays instead [64]. For weak to moderate strength shocks, the former method is chosen as it is simpler. For the diffraction of a very strong shock Whitham has chosen the latter method and found that the shock shape is given universally in terms of the similarity parameters $X/\alpha M_0$ and $Y/\alpha M_0$ centered at the edge, where α is the time-dependent coordinate ($c_0 t$) used in the theory's derivation.

As the Ray-shock Theory was the first feasible method to emerge, an early experimental verification for it has been undertaken by Skews [61,62] for 2-D diffraction around both sharp and rounded corners via Schlieren photography. As anticipated by Whitham, reasonable agreement between the experimental and theoretical shock profiles is observed

only for shock Mach numbers greater than about 3.0. For lower values of Mach numbers, Whitham observed that the theory concentrates the disturbance over too small a segment of the shock. In actuality, the disturbance is spread over the entire region encompassed by the sonic circle emanating from the corner, as is verified by Skew's experiments.

The approximate nature of the Ray-shock Theory is demonstrated by the fact that for a given shock Mach number there exists a limiting value of the turning angle which corresponds to a wall shock Mach number equal to unity. Beyond the maximum angle, no solution exists for a given M_0 since the shock wave degenerates into a Mach wave. However, experimental evidence indicates that this is inaccurate for low or even moderate shock Mach numbers ($M_0 < 3$) [61]. For example, at Mach number 1.5, the critical diffraction angle is roughly 90° while the experiments show a finite shock strength even for Mach number 1.2 and a diffraction angle of nearly 180°. For corner angles less than 90°, the theory is observed to predict the wall shock Mach number fairly well throughout the entire range of the tests (Mach numbers = 1.0 to 5.0 approximately).

The theoretical value for the angle (m_0) takes the form :

$$\tan(m_0) = \sqrt{\frac{(M_0^2 - 1)[2 + (\gamma - 1)M_0^2]}{(\gamma + 1)\, M_0^4}} \qquad (2.38)$$

These results imply that the Ray-shock Theory will likely not accurately predict the characteristic angle (m) at any arbitrary location on the diffracted shock as well. Skews'

experiments using Schlieren photography demonstrate that a finite shock strength is observed for initial Mach numbers for all corner angles tested (up to nearly 180 °) while the theory breaks down at limited diffraction angles of about 72 °. Skews thus concluded that generally the Ray-shock Theory is not adequate for all shock Mach numbers and corner angles simultaneously. For moderate shocks, the theory works well for angles less or equal to 30°, while for large corner angles, good agreement with the theory is observed only for $M_0 > 3$. The two formulae were found to approach the same asymptotic value of 23 ° at Mach numbers > 5.

For strong shocks and slight turning angles, assuming an average constant Chester function K(M) becomes applicable, so are equations (2.36,37) and - defining the average value (n) as $2 / K_{av}$ - the head characteristic angle is approximated as

$$\tan m_0 = \sqrt{\frac{(M_0^2 - 1)}{n M_0^2}} \qquad (2.39)$$

For the interaction of a plane shock with a concave corner, the CCW and Ray-shock Theory were used to calculate the resulting motion. It was experimentally observed that a critical angle value - which depends on the incident shock Mach number - exists, dividing between two possible cases:

- If the angle is below this value, Mach reflection will take place where the shock is replaced by the confluence of three parts : the remaining incident shock, a reflected shock initiated at the corner and its profile depending on the fluid Mach number behind the shock, and a third shock - called Mach stem - normal to the wall with the flow behind parallel to the wall. The point of confluence is referred to as the "triple point".

- If the angle is higher than the critical one, the Mach stem disappears and the incident-reflected shock structure, called regular reflection, prevails.

A schematic description for the two cases is shown in Fig.(2.6). In the present study, the interest will be confined to the first case since it is the one mostly found. Although Mach stems are assumed to be straight it was found that this is not the case, specially for weak shocks and near the triple point. This is due to the fact that the fluid is affected by three rather than one shock, as well as the non-uniformity of the conditions behind the advancing shock structure (due to reflected waves) which - in turn - affects the shock behavior through characteristics. Since part of the flow is influenced by the incident-reflected shock couple while another part by the Mach stem, a slip line is created behind the shock formation across which equality in pressure only is satisfied.

The Ray-shock Theory treatment assumes straight Mach stems. For the geometrical compatibility of the two triangles described in Fig. (2.7)

$$\frac{A}{A_0} = \frac{\sin(\chi-\theta)}{\sin\chi} \quad \text{and} \quad \frac{M}{M_0} = \frac{\cos(\chi-\theta)}{\cos\chi} \tag{2.40}$$

Also, considering the values of Ray-shock Theory variables

$$\tan(\chi-\theta) = \frac{A\,\Delta\beta}{M\,\Delta\alpha} \quad \text{and} \quad \tan\chi = \frac{A_0\,\Delta\beta}{M_0\,\Delta\alpha}$$

$$\therefore \quad \tan(\chi-\theta) = \frac{A}{A_0}\cdot\frac{M_0}{M}\,\tan\chi$$

which is consistent with the geometrical considerations above, thus leading to the final set of equations

$$\tan(\chi-\theta) = \frac{A}{A_0}\left\{\frac{1-(M_0/M)^2}{1-(A/A_0)^2}\right\}^{1/2} \tag{2.41a}$$

$$\tan\theta = \frac{(M^2-M_0^2)^{1/2}\,(A_0^2-A^2)^{1/2}}{AM+A_0M_0} \tag{2.41b}$$

in addition to the previously derived CCW equations (2.24,25)

$$\frac{A}{A_0} = \frac{f(M)}{f(M_0)} \text{ in general} \quad , \quad \frac{A}{A_0} \cong \left\{\frac{M_0}{M}\right\}^{n} \text{ for strong shocks}$$

The integral f(M) is evaluated using the reference M = 1 state and the Chester function, as indicated before.

However, the theory was found to have limitations in finding the Mach stem angle. For moderate to weak shocks, it was found that the Ray-shock Theory overestimates the Mach stem angle for wedge angles higher than 20° . On the other hand, when the wedge angle approaches zero - which means that acoustic theory is applicable - the theory was found to underestimate the angle. As a compromise based on experimental observations, Ostrowski [64] suggested the use of the mean value of the Ray Theory and the acoustic theory values for the triple-point locus.

Although the processes described above are those occurring at the corners, other reflection processes occur at the straight wall for the fully developed Mach stem and the expansion fan or whatever comes out of their interaction. For this reason, the duct or chamber width plays a pivotal role in defining the exact features of the problem since it controls the reflection positions and consequently the interaction trends.

3 - NUMERICAL METHOD

The solution of Euler equations has always been a challenge to specialists in computational gas dynamics. Despite their apparent simplicity, their mathematical hyperbolic nature implies the physical existence of characteristic directions for signal propagation with respect to time. Even in steady flow analysis, the problem becomes more critical in case of transonic flow which includes mixtures of subsonic flow domains (in which signals passing by any point can propagate in all directions) and supersonic flow domains (in which signals passing by the point propagate into - or come out of - restricted domains governed by the Mach number). To reach an efficient simulation of the physical problem, the numerical scheme has to accurately simulate the process of signal propagation (or zonal interaction) while defining the mathematical relations between nodal variables.

To simulate unsteady transonic flows, numerical schemes fall into two main categories:

1. Explicit schemes : in which the spatial residue formulation is evaluated at the old time level. This means that each nodal value at the calculated new time level is obtained in terms of the old set of values at the previous time level.

2. Implicit schemes : in which spatial residue formulation is evaluated at the new time level. This is formulated using a "reversed" form of the explicit schemes (each nodal value at the old time level is expressed as a function of the values at the new time

level). Consequently all the equations for nodal values at the calculated new time level are coupled and should be solved for simultaneously.

The main advantage for implicit schemes is their unconditional stability, which facilitates using unstructured grids and increasing the time step to a limit governed only by accuracy considerations. This depends on the complexity of the geometry and flow history. However, they require larger amount of matrix storage for the discretized spatial and temporal derivatives. Since the accuracy of the time derivative has a profound effect on the obtained flow history, solution at two or more previous time levels are used to discretize the current time derivative and increase its order of accuracy. This limits the ability for changing the time steps and increases storage requirements.

On the other hand, explicit schemes require storing only the time-derivative terms in the matrix. This advantage of considerable reduction in matrix storage can be augmented further if the set of variables is chosen such that the time derivative matrix is diagonal-dominant and linear. In this case the matrix is loaded once during the run. Unlike multi-step implicit schemes, it is possible for explicit schemes to change the time step in the middle of calculations (by re-scaling the matrix). This is useful in case the time step needs change for stability- or accuracy-related reasons. The main disadvantage is the limitation imposed on the time step to ensure stability (the Courant-Friedrich-Lewy criterion). According to the CFL criterion, signals emanating from one node point at the calculated time level should not overjump the neighboring node points at the next time level. The

problem becomes more critical in case of unequal element size (which is desirable for a better simulation for the flow at high gradient domains). Although this limitation could be inevitable for the sake of simulating the flow history with reasonable accuracy, the number of nodes, and the size of their associated arrays, becomes higher and consumes part of the gained storage space.

Considering explicit and implicit methods as the two extremes in numerical simulations, researchers tried to reach a compromise by deriving schemes which combine as much as possible the advantages of both. The literature contains a variety of schemes of variable order of accuracy with mixed formulation for the temporal derivatives [71].

3.1 - Finite Element Method :

The rapid development of the Finite Element Method has led to its incorporation into a gradually increasing number of fields of scientific research dealing with continuum physics. In the Finite Element Method, the domain is divided into small cells (or elements). Inside each element, a prescribed piecewise continuous distribution of the variables is assumed in terms of the values at the element's corner points (or nodes). The problem is then transformed into finding the finite set of nodal values so as to satisfy the governing equations with the minimum possible residual error integral.

The basic advantages of the Finite Element Method can be summarized as the following:

1. Its weighted average solutions cover the complete domains solved for, rather than local linearization of differential terms at nodes (e.g., the Finite Difference Method).

2. Since nodes are shared between adjacent elements, then the prescribed distribution can also be made continuous across the boundaries, thus ensuring solution continuity over the whole domain.

3. The method's flexibility in conforming with complicated domain geometries. This is attributed to the localized nature of the mapping process linking the real element in the physical domain to the parent element in the computational domain. This is contrary to old methods which require global mapping of the computational grid to ensure localized conformity (which puts limits on the grid design according to domain complexity).

4. The ability of the mathematical formulation, extending to element boundaries, to incorporate the natural boundary conditions through its contour integrals. Consequently, the extrapolation of any mathematical quantity from inside the domain to the boundaries is done automatically.

Although the Finite Element Method was a late newcomer to the field of numerical methods for fluid dynamics, it has achieved considerable progress in simulating viscous as

well as inviscid flow test cases. Despite the fact that most of the scheme development efforts are still based on the two older methods, the FEM is gaining more ground and more schemes, originally derived for the FDM and FVM, were re-formulated for the FEM [75]. However, it has been noticed that this is not the case for researchers working in the field of shock wave dynamics, of whom very few showed interest in the method [72-74].

In this chapter, a fully implicit multi-step three-dimensional Finite Element scheme is introduced for the solution of unsteady Euler set of equations for 2-D or 3-D domains. Two-dimensionality can be imposed in the global matrix assembly stage by imposing invariance in the transverse direction, and plane motion can be imposed through setting the transverse velocity to zero. The code was prepared for using the minimum possible storage requirements, with an iterative solver for the resulting matrix equation. The success of the code to simulate 1-D and 2-D problems gives a good indication about the code's capability of simulating the original fully 3-D cases.

3.2 - Governing Equations :

The Euler equations for 3-D unsteady inviscid compressible gas, without heat conducting or chemical reaction, are written in conservation form as follows :

Mass :
$$\frac{\partial \rho}{\partial t} + \underline{\nabla} . (\rho \underline{v}) = 0 \qquad (3.1a)$$

Radial momentum :
$$\frac{\partial (\rho v_r)}{\partial t} + \underline{\nabla} . (\rho \underline{v} v_r) = - \frac{\partial p}{\partial r} + \frac{\rho v_\theta^2}{r} \qquad (3.1b)$$

Tangential momentum :
$$\frac{\partial (\rho v_\theta)}{\partial t} + \underline{\nabla} . (\rho \underline{v} v_\theta) = - \frac{\partial p}{r \partial \theta} - \frac{\rho v_r v_\theta}{r} \qquad (3.1c)$$

Axial momentum :
$$\frac{\partial (\rho v_z)}{\partial t} + \underline{\nabla} . (\rho \underline{v} v_z) = - \frac{\partial p}{\partial z} \qquad (3.1d)$$

Energy :
$$\frac{\partial p}{\partial t} + \underline{\nabla} . (\gamma \underline{v} p) = (\gamma - 1) \underline{\nabla} p . \underline{v} \qquad (3.1e)$$

where the variables are : the density (ρ), mass velocity ($\rho \underline{v}$), pressure (p)

This set of variables was chosen to be suitable for both explicit and implicit schemes to account for the possibility of future modifications. However, it was decided to use implicit methods at the present stage to be able to change element size distribution without stability problems. The energy equation was put in its modified form omitting the kinetic energy term, thus making it represent the pressure variation equation.

Since the primitive variable formulation is convection-dominated, an artificial dissipation term had to be used to smooth the shock discontinuity by diffusing it along few grid points, to omit the possibility of entropy-lowering expansion shocks and to overcome the matrix ill-conditioning due to the central difference discretization of convection terms. Since all the equations take the form

$$\frac{\partial(\phi)}{\partial t} + \underline{\nabla} . (\underline{v}\phi) = S_{\phi}$$

where ϕ is the thermodynamic variable, a Laplacian term was introduced to the RHS of all the above equations. The Laplacian coefficients were tested to be made as small as possible. In the modified form, Euler equations will take the form :

$$\frac{\partial \rho}{\partial t} + \underline{\nabla} . (\rho \underline{v}) = \underline{\nabla} . ([\mu] . \underline{\nabla} \rho) \tag{3.2a}$$

$$\frac{\partial (\rho v_r)}{\partial t} + \underline{\nabla} . (\rho \underline{v} v_r) = -\frac{\partial p}{\partial r} + \frac{\rho v_\theta^2}{r} + \underline{\nabla} . ([\mu] . \underline{\nabla} \rho v_r) \tag{3.2b}$$

$$\frac{\partial (\rho v_\theta)}{\partial t} + \underline{\nabla} . (\rho \underline{v} v_\theta) = -\frac{\partial p}{r \partial \theta} - \frac{\rho v_r v_\theta}{r} + \underline{\nabla} . ([\mu] . \underline{\nabla} \rho v_\theta) \tag{3.2c}$$

$$\frac{\partial (\rho v_z)}{\partial t} + \underline{\nabla} . (\rho \underline{v} v_z) = -\frac{\partial p}{\partial z} + \underline{\nabla} . ([\mu] . \underline{\nabla} \rho v_z) \tag{3.2d}$$

$$\frac{\partial p}{\partial t} + \underline{\nabla} . (\gamma \underline{v} p) = (\gamma - 1) \underline{\nabla} p . \underline{v} + \gamma \underline{\nabla} . ([\mu] . \underline{\nabla} p) \tag{3.2e}$$

where $[\mu]$ is a diagonal matrix relating the diffusion and the gradient vector of the convected variable. In the simple case this will be equal to a constant multiplied by the identity matrix [I] . In the present case this matrix was chosen as follows :

$$[\mu] = \begin{bmatrix} \mu_r & 0 & 0 \\ 0 & \mu_\theta & 0 \\ 0 & 0 & \mu_z \end{bmatrix} \tag{3.3}$$

where the coefficients are constant but linearly proportional to their respective grid sizes and the anticipated orders of magnitudes of the respective velocity components.

3.3 - Weak Formulation :

For every time marching to a new time level, the set of coupled equations was discretized using the Galerkin weighted residual formulation for the spatial coordinate distributions and derivatives [75,76]. The implicit 3-step Gear formulation, based on a Taylor series expansion in time, was used for the time derivatives since it has proven to be accurate enough for maintaining shock intensity and time accuracy.

The weak form is created by multiplying the governing equations, in the form $F(u) = 0$, by a group of test functions (called weight functions):

$$W_i \quad , \quad i = 1 \ , \ \text{number of nodes / element}$$

covering the element space but giving more weight to the zones adjacent to their respective nodes. For each test function, the weighted residual is integrated over the element volume. Through the coupled solution for all elements and nodes, the local as well as global residuals are brought to their minimum possible values. The resulting divergence volume integrals are transformed into surface integrals using the divergence theorem, and used to introduce natural boundary conditions.

For the set of Euler equations, the weighted residual equations take the form:

Continuity :

$$\iiint_{V_e} W_i \left\{ \frac{\partial \rho}{\partial t} + \underline{\nabla} . (\rho \, \underline{v}) - \underline{\nabla} . ([\mu] . \underline{\nabla} \rho) \right\} dV = 0 \quad \Rightarrow$$

$$\iiint_{V_e} \left\{ W_i \frac{\partial \rho}{\partial t} - \underline{\nabla} W_i . (\rho \, \underline{v} - [\mu] . \underline{\nabla} \rho) \right\} dV +$$

$$\iint_{A_e} W_i \, \{ \rho \, \underline{v} - [\mu] . \underline{\nabla} \rho \} . \underline{n} \, dA = 0 \qquad (3.4a)$$

Radial momentum :

$$\iiint_{V_e} W_i \left\{ \frac{\partial(\rho v_r)}{\partial t} + \underline{\nabla}.(\rho \underline{v} v_r) + \frac{\partial p}{\partial r} - \frac{\rho v_\theta^2}{r} - \underline{\nabla}.([\mu].\underline{\nabla}\rho v_r) \right\} dV = 0 \Rightarrow$$

$$\iiint_{V_e} \left\{ W_i \frac{\partial(\rho v_r)}{\partial t} - W_i \frac{p+\rho v_\theta^2}{r} - \underline{\nabla} W_i .(\rho \underline{v} v_r - [\mu].\underline{\nabla}\rho v_r) - p\frac{\partial W_i}{\partial r} \right\} dV +$$
$$\iint_{A_e} W_i \{\rho \underline{v} v_r - [\mu].\underline{\nabla}\rho v_r + p \underline{e}_r\}.\underline{n}\, dA = 0 \qquad (3.4b)$$

Tangential momentum :

$$\iiint_{V_e} W_i \left\{ \frac{\partial(\rho v_\theta)}{\partial t} + \underline{\nabla}.(\rho \underline{v} v_\theta) + \frac{\partial p}{r\partial\theta} + \frac{\rho v_r v_\theta}{r} - \underline{\nabla}.([\mu].\underline{\nabla}\rho v_\theta) \right\} dV = 0 \Rightarrow$$

$$\iiint_{V_e} \left\{ W_i \frac{\partial(\rho v_\theta)}{\partial t} + W_i \frac{\rho v_r v_\theta}{r} - \underline{\nabla} W_i .(\rho \underline{v} v_\theta - [\mu].\underline{\nabla}\rho v_\theta) - p\frac{\partial W_i}{r\partial\theta} \right\} dV +$$
$$\iint_{A_e} W_i \{\rho \underline{v} v_\theta - [\mu].\underline{\nabla}\rho v_\theta + p \underline{e}_\theta\}.\underline{n}\, dA = 0 \qquad (3.4c)$$

Axial momentum :

$$\iiint_{V_e} W_i \left\{ \frac{\partial(\rho v_z)}{\partial t} + \underline{\nabla}.(\rho \underline{v} v_z) + \frac{\partial p}{\partial z} - \underline{\nabla}.([\mu].\underline{\nabla}\rho v_z) \right\} dV = 0 \Rightarrow$$

$$\iiint_{V_e} \left\{ W_i \frac{\partial(\rho v_z)}{\partial t} - \underline{\nabla} W_i .(\rho \underline{v} v_z - [\mu].\underline{\nabla}\rho v_z) + p\frac{\partial W_i}{\partial z} \right\} dV +$$
$$\iint_{A_e} W_i \{\rho \underline{v} v_z - [\mu].\underline{\nabla}\rho v_z + p \underline{e}_z\}.\underline{n}\, dA = 0 \qquad (3.4d)$$

Energy :

$$\iiint_{V_e} W_i \left\{ \frac{\partial p}{\partial t} + \underline{\nabla}.(\gamma \underline{v} p) - (\gamma-1)\underline{\nabla} p.\underline{v} - \gamma \underline{\nabla}.([\mu].\underline{\nabla} p) \right\} dV = 0 \Rightarrow$$

$$\iiint_{V_e} \left\{ W_i \frac{\partial p}{\partial t} - W_i(\gamma-1)\underline{\nabla} p.\underline{v} - \underline{\nabla} W_i .(\gamma \underline{v} p - \gamma [\mu].\underline{\nabla} p) \right\} dV +$$
$$\iint_{A_e} W_i \{\gamma \underline{v} p - \gamma [\mu].\underline{\nabla} p\}.\underline{n}\, dA = 0 \qquad (3.4e)$$

The formula for variable distribution inside the element is written in the form

$$\phi = \sum_{j=1}^{nnode} N_j \, \phi_j \qquad (3.5)$$

where N_j is the shape function defining the contribution of node (j), ϕ_j is the associated nodal value of the variable and (nnode) is the number of nodes in the element. The brick elements used in the present work are defined in a dimensionless mathematical space, called the natural coordinate space, as cubes extending between the values (-1 , 1) in each direction (Fig.(3.1)). The trilinear shape function is defined in terms of the natural coordinates (ξ, η, ζ) as :

$$N_j = \frac{1}{8}(1+\xi\xi_j)(1+\eta\eta_j)(1+\zeta\zeta_j) \quad , \quad j = 1, 8 \qquad (3.6)$$

For simulation of spatial variable derivatives, the shape function partial derivatives with respect to physical coordinates are needed. These derivatives are obtained at any point inside the element through inverting the Jacobean equation. In the element used, the real coordinates are linearly distributed in the natural coordinate space using the same shape functions as the variables. So the Jacobean matrix elements - as well as the variable gradient vector w.r.t. natural coordinates - are also evaluated using the shape functions and their derivatives :

$$\begin{bmatrix} \frac{\partial N_j}{\partial \xi} \\ \frac{\partial N_j}{\partial \eta} \\ \frac{\partial N_j}{\partial \zeta} \end{bmatrix} = \begin{bmatrix} \frac{\partial r}{\partial \xi} & \frac{r\partial \theta}{\partial \xi} & \frac{\partial z}{\partial \xi} \\ \frac{\partial r}{\partial \eta} & \frac{r\partial \theta}{\partial \eta} & \frac{\partial z}{\partial \eta} \\ \frac{\partial r}{\partial \zeta} & \frac{r\partial \theta}{\partial \zeta} & \frac{\partial z}{\partial \zeta} \end{bmatrix} \begin{bmatrix} \frac{\partial N_j}{\partial r} \\ \frac{\partial N_j}{r\partial \theta} \\ \frac{\partial N_j}{\partial z} \end{bmatrix} = \left[\mathbf{J} \right] \begin{bmatrix} \frac{\partial N_j}{\partial r} \\ \frac{\partial N_j}{r\partial \theta} \\ \frac{\partial N_j}{\partial z} \end{bmatrix} \tag{3.7}$$

For the Galerkin formulation used, the weight functions are also chosen to be the same shape functions for the nodes. Because of the non-linearity, the problem is cast in the Newton iterative technique. The value of an unknown ϕ is linearized and modified after each iteration as follows :

$$\phi^{n+1} = \phi^{n} + d\,\phi \tag{3.8}$$

The differential terms with order higher than first order are neglected. Applying the distribution formulae on the element level and assembling for the whole grid, a global matrix equation is created in the form :

$$\left[K_{ij}\right]\left\{d\phi_j\right\} = -\left\{R_i\right\} \tag{3.9}$$

where

K = the Jacobean matrix of coefficients (solution-dependent)

ϕ = vector of the current solution values

$d\phi$ = the increments to be added to the current values

R = the residue vector, which is the motive for the solution correction

For the equations used, the local element's matrix equations will take the following shape :

Continuity (3.10a):

$$\sum_{j=1}^{8}\left[\sum_{m=1}^{5} K_{ijm}^{(\rho)}\right] = -R_i^{(\rho)} \qquad \text{where}$$

$$K_{ij1}^{(\rho)} = \iiint_{V_e}\left\{1.5\frac{W_i\,N_j}{\Delta t} + \underline{\nabla} W_i \,.\,([\mu].\underline{\nabla} N_j)\right\} dV + \iint_{A_e} -W_i\left\{[\mu].\underline{\nabla} N_j\right\}.\underline{n}\,dA$$

$$K_{ij2}^{(\rho)} = \iiint_{V_e} -\frac{\partial W_i}{\partial r}\,.\,N_j\,dV + \iint_{A_e} W_i\,N_j\,\underline{e}_r\,.\,\underline{n}\,dA$$

$$K_{ij3}^{(\rho)} = \iiint_{V_e} -\frac{\partial W_i}{r\partial\theta}\,.\,N_j\,dV + \iint_{A_e} W_i\,N_j\,\underline{e}_\theta\,.\,\underline{n}\,dA$$

$$K_{ij4}^{(\rho)} = \iiint_{V_e} -\frac{\partial W_i}{\partial z}\,.\,N_j\,dV + \iint_{A_e} W_i\,N_j\,\underline{e}_z\,.\,\underline{n}\,dA$$

$$R_i^{(\rho)} = \iiint_{V_e}\left\{W_i\,\frac{1}{\Delta t}\left[1.5\rho^{(n+1)} - 2\rho^{(n)} + 0.5\rho^{(n-1)}\right] - \underline{\nabla} W_i\,.\left(\rho\,\underline{v} - [\mu].\underline{\nabla}\rho\right)\right\} dV +$$

$$\iint_{A_e} W_i\,\left\{\rho\,\underline{v} - [\mu].\underline{\nabla}\rho\right\}.\underline{n}\,dA$$

Radial momentum (3.10b):

$$\sum_{j=1}^{8}\left[\sum_{m=1}^{5} K_{ijm}^{(\rho v_r)}\right] = -R_i^{(\rho v_r)} \qquad \text{where}$$

$$K_{ij1}^{(\rho v_r)} = \iiint_{V_e}\left\{\frac{1}{\rho^2}(\underline{\nabla} W_i \cdot \rho\,\underline{v})\,\rho v_r N_j + \frac{1}{\rho r} W_i\, N_j\,\frac{(\rho v_\theta)^2}{\rho}\right\} dV -$$

$$\iint_{A_e} \frac{1}{\rho^2} W_i\, N_j\, \rho v_r\,(\rho\underline{v}\cdot\underline{n}\, dA)$$

$$K_{ij2}^{(\rho v_r)} = \iiint_{V_e}\left\{1.5\frac{W_i\, N_j}{\Delta t} - \frac{1}{\rho}\left(\underline{\nabla} W_i \cdot \rho\,\underline{v} + \frac{\partial W_i}{\partial r}\rho v_r\right) N_j + \underline{\nabla} W_i \cdot \left\{[\mu]\cdot\underline{\nabla} N_j\right\}\right\} dV +$$

$$\iint_{A_e} W_i\left\{\frac{1}{\rho} N_j\,(\rho\underline{v} + \rho v_r \underline{e}_r) - [\mu]\cdot\underline{\nabla} N_j\right\}\cdot\underline{n}\, dA$$

$$K_{ij3}^{(\rho v_r)} = \iiint_{V_e}\left\{-\frac{\partial W_i}{r\partial\theta}\frac{\rho v_r}{\rho} N_j - \frac{2}{\rho r} W_i N_j \rho v_\theta\right\} dV + \iint_{A_e}\frac{1}{\rho} W_i\, N_j\,\rho v_r\,\underline{e}_\theta\cdot\underline{n}\, dA$$

$$K_{ij4}^{(\rho v_r)} = \iiint_{V_e}\left\{-\frac{\partial W_i}{\partial z} N_j\,\frac{\rho v_r}{\rho}\right\} dV + \iint_{A_e}\frac{1}{\rho} W_i\, N_j\,\rho v_r\,\underline{e}_z\cdot\underline{n}\, dA$$

$$K_{ij5}^{(\rho v_r)} = \iiint_{V_e} -\left(\frac{\partial W_i}{\partial r} + \frac{W_i}{r}\right) N_j\, dV + \iint_{A_e} W_i\, N_j\ \underline{e}_r\cdot\underline{n}\, dA$$

$$R_i^{(\rho v_r)} = \iiint_{V_e}\left\{\frac{W_i}{\Delta t}\left[1.5\rho v_r^{(n+1)} - 2\rho v_r^{(n)} + 0.5\rho v_r^{(n-1)}\right] - W_i\,\frac{\rho v_\theta^2}{r}\right\} dV +$$

$$\iiint_{V_e}\left\{-\underline{\nabla} W_i\cdot\left\{\rho\,\underline{v}\,v_r - [\mu]\cdot\underline{\nabla}\rho v_r\right\} - p\left(\frac{\partial W_i}{\partial r} + \frac{W_i}{r}\right)\right\} dV +$$

$$\iint_{A_e} W_i\left\{\rho\,\underline{v}\,v_r - [\mu]\cdot\underline{\nabla}\rho v_r + p\,\underline{e}_r\right\}\cdot\underline{n}\, dA$$

Tangential momentum (3.10c):

$$\sum_{j=1}^{8}\left[\sum_{m=1}^{5} K_{ijm}^{(\rho v_\theta)}\right] = -R_i^{(\rho v_\theta)} \qquad \text{where}$$

$$K_{ij1}^{(\rho v_\theta)} = \iiint_{V_e}\left\{\frac{1}{\rho^2}(\underline{\nabla}W_i \cdot \rho\,\underline{v})\,\rho v_\theta N_j - \frac{1}{\rho r} W_i\, N_j\, \frac{\rho v_r\, \rho v_\theta}{\rho}\right\} dV -$$

$$\iint_{A_e} \frac{1}{\rho^2} W_i\, N_j\, \rho v_\theta\, (\rho\underline{v} \cdot \underline{n}\, dA)$$

$$K_{ij2}^{(\rho v_\theta)} = \iiint_{V_e}\left\{-\frac{\partial W_i}{\partial r} N_j \frac{\rho v_\theta}{\rho} + \frac{1}{\rho r} W_i N_j \rho v_\theta\right\} dV + \iint_{A_e} \frac{1}{\rho} W_i\, N_j\, \rho v_\theta\, \underline{e}_r \cdot \underline{n}\, dA$$

$$K_{ij3}^{(\rho v_\theta)} = \iiint_{V_e}\left\{1.5\frac{W_i\, N_j}{\Delta t} + \frac{1}{\rho r} W_i N_j \rho v_r\right\} dV +$$

$$\iiint_{V_e}\left\{-\frac{1}{\rho}\left(\underline{\nabla}W_i \cdot \rho\,\underline{v} + \frac{\partial W_i}{r\partial\theta}\rho v_\theta\right) N_j + \underline{\nabla}W_i \cdot \left\{[\mu] \cdot \underline{\nabla} N_j\right\}\right\} dV +$$

$$\iint_{A_e} W_i \left\{\frac{1}{\rho} N_j\, (\rho\underline{v} + \rho v_\theta \underline{e}_\theta) - [\mu] \cdot \underline{\nabla} N_j\right\} \cdot \underline{n}\, dA$$

$$K_{ij4}^{(\rho v_\theta)} = \iiint_{V_e}\left\{-\frac{\partial W_i}{\partial z} N_j \frac{\rho v_\theta}{\rho}\right\} dV + \iint_{A_e} \frac{1}{\rho} W_i\, N_j\, \rho v_\theta\, \underline{e}_z \cdot \underline{n}\, dA$$

$$K_{ij5}^{(\rho v_\theta)} = \iiint_{V_e} -\left(\frac{\partial W_i}{r\partial\theta}\right) N_j\, dV + \iint_{A_e} W_i\, N_j\, \underline{e}_\theta \cdot \underline{n}\, dA$$

$$R_i^{(\rho v_\theta)} = \iiint_{V_e}\left\{\frac{W_i}{\Delta t}\left[1.5\rho v_\theta^{(n+1)} - 2\rho v_\theta^{(n)} + 0.5\rho v_\theta^{(n-1)}\right] + W_i \frac{\rho\, v_r\, v_\theta}{r}\right\} dV +$$

$$\iiint_{V_e}\left\{-\underline{\nabla}W_i \cdot \left\{\rho\,\underline{v}\, v_\theta - [\mu] \cdot \underline{\nabla}\rho v_\theta\right\} - p\frac{\partial W_i}{r\partial\theta}\right\} dV +$$

$$\iint_{A_e} W_i \left\{\rho\,\underline{v}\, v_\theta - [\mu] \cdot \underline{\nabla}\rho v_\theta + p\,\underline{e}_\theta\right\} \cdot \underline{n}\, dA$$

Axial momentum (3.10d):

$$\sum_{j=1}^{8}\left[\sum_{m=1}^{5} K_{ijm}^{(\rho v_z)}\right] = -R_i^{(\rho v_z)} \qquad \text{where}$$

$$K_{ij1}^{(\rho v_z)} = \iiint_{V_e}\left\{\frac{1}{\rho^2}(\underline{\nabla} W_i \cdot \rho\underline{v})\,\rho v_z N_j\right\} dV - \iint_{A_e}\frac{1}{\rho^2} W_i\, N_j\, \rho v_z\,(\rho\underline{v}\cdot\underline{n}\, dA)$$

$$K_{ij2}^{(\rho v_z)} = \iiint_{V_e}\left\{-\frac{\partial W_i}{\partial r} N_j \frac{\rho v_z}{\rho}\right\} dV + \iint_{A_e}\frac{1}{\rho} W_i\, N_j\, \rho v_z\, \underline{e}_r \cdot \underline{n}\, dA$$

$$K_{ij3}^{(\rho v_z)} = \iiint_{V_e}\left\{-\frac{\partial W_i}{r\partial\theta} N_j \frac{\rho v_z}{\rho}\right\} dV + \iint_{A_e}\frac{1}{\rho} W_i\, N_j\, \rho v_z\, \underline{e}_\theta \cdot \underline{n}\, dA$$

$$K_{ij4}^{(\rho v_z)} = \iiint_{V_e}\left\{1.5\frac{W_i\, N_j}{\Delta t} - \frac{1}{\rho}\left(\underline{\nabla} W_i \cdot \rho\,\underline{v} + \frac{\partial W_i}{\partial z}\rho v_z\right) N_j + \underline{\nabla} W_i \cdot \left\{[\mu]\cdot\underline{\nabla} N_j\right\}\right\} dV +$$

$$\iint_{A_e} W_i\left\{\frac{1}{\rho} N_j\,(\rho\underline{v} + \rho v_z \underline{e}_z) - [\mu]\cdot\underline{\nabla} N_j\right\}\cdot\underline{n}\, dA$$

$$K_{ij5}^{(\rho v_z)} = \iiint_{V_e} -\left(\frac{\partial W_i}{\partial z}\right) N_j\, dV + \iint_{A_e} W_i\, N_j\ \underline{e}_z \cdot \underline{n}\, dA$$

$$R_i^{(\rho v_z)} = \iiint_{V_e}\left\{\frac{W_i}{\Delta t}\left[1.5\rho v_z^{(n+1)} - 2\rho v_z^{(n)} + 0.5\rho v_z^{(n-1)}\right]\right\} dV +$$

$$\iiint_{V_e}\left\{-\underline{\nabla} W_i \cdot \left\{\rho\,\underline{v}\, v_z - [\mu]\cdot\underline{\nabla}\rho v_z\right\} - p\frac{\partial W_i}{\partial z}\right\} dV +$$

$$\iint_{A_e} W_i\left\{\rho\,\underline{v}\, v_z - [\mu]\cdot\underline{\nabla}\rho v_z + p\,\underline{e}_z\right\}\cdot\underline{n}\, dA$$

Energy (3.10e):

$$\sum_{j=1}^{8}\left[\sum_{m=1}^{5} K_{ijm}^{(p)}\right] = -R_i^{(p)} \qquad \text{where}$$

$$K_{ij1}^{(p)} = \iiint_{V_e}\left\{\frac{1}{\rho^2}(\underline{\nabla} W_i \cdot \rho\underline{v})\, p\, N_j + \frac{1}{\rho^2} W_i\, N_j (\gamma-1)\,\underline{\nabla} p \cdot \rho\underline{v}\right\} dV -$$

$$\iint_{A_e} \frac{1}{\rho^2} W_i\, N_j\, p\, (\rho\underline{v} \cdot \underline{n}\, dA)$$

$$K_{ij2}^{(p)} = \iiint_{V_e}\left\{-\gamma\frac{\partial W_i}{\partial r} N_j \frac{p}{\rho} - \frac{1}{\rho^2} W_i\, N_j (\gamma-1)\frac{\partial p}{\partial r}\right\} dV + \iint_{A_e} \frac{\gamma}{\rho} W_i\, N_j\, p\, \underline{e}_r \cdot \underline{n}\, dA$$

$$K_{ij3}^{(p)} = \iiint_{V_e}\left\{-\gamma\frac{\partial W_i}{r\partial\theta} N_j \frac{p}{\rho} - \frac{1}{\rho^2} W_i\, N_j (\gamma-1)\frac{\partial p}{r\partial\theta}\right\} dV + \iint_{A_e} \frac{\gamma}{\rho} W_i\, N_j\, p\, \underline{e}_\theta \cdot \underline{n}\, dA$$

$$K_{ij4}^{(p)} = \iiint_{V_e}\left\{-\gamma\frac{\partial W_i}{\partial z} N_j \frac{p}{\rho} - \frac{1}{\rho^2} W_i\, N_j (\gamma-1)\frac{\partial p}{\partial z}\right\} dV + \iint_{A_e} \frac{\gamma}{\rho} W_i\, N_j\, p\, \underline{e}_z \cdot \underline{n}\, dA$$

$$K_{ij5}^{(p)} = \iiint_{V_e}\left\{1.5\frac{W_i\, N_j}{\Delta t} - \frac{1}{\rho}(\gamma-1)(\underline{\nabla} N_j \cdot \rho\,\underline{v}) W_i\right\} dV +$$

$$\iiint_{V_e}\left\{-\frac{\gamma}{\rho}\underline{\nabla} W_i \cdot \left\{\rho\,\underline{v}\, N_j - [\mu]\cdot\underline{\nabla} N_j\right\}\right\} dV +$$

$$\iint_{A_e} W_i \left\{\frac{\gamma}{\rho} N_j (\rho\underline{v}) - \gamma[\mu]\cdot\underline{\nabla} N_j\right\}\cdot \underline{n}\, dA$$

$$R_i^{(p)} = \iiint_{V_e}\left\{\frac{W_i}{\Delta t}\left[1.5\, p^{(n+1)} - 2\, p^{(n)} + 0.5\, p^{(n-1)}\right] - \frac{1}{\rho} W_i (\gamma-1)\,\underline{\nabla} p \cdot \rho\underline{v}\right\} dV +$$

$$\iiint_{V_e}\left\{-\underline{\nabla} W_i \cdot \left\{\gamma\,\underline{v}\, p - \gamma[\mu]\cdot\underline{\nabla} p\right\}\right\} dV + \iint_{A_e} W_i \left\{\gamma\,\underline{v}\, p - \gamma[\mu]\cdot\underline{\nabla} p\right\}\cdot\underline{n}\, dA$$

The volume or surface integrals are evaluated numerically using Gauss quadrature technique. Three quadrature point were chosen for every spatial direction to ensure accuracy up to a fifth-degree polynomial. For multi-dimensional integration, the Gauss point locations are distributed in the multi-dimensional range (-1 , 1), while their weight values are combinations of the one-dimensional weight values (according to their location in the natural coordinate space).

Concerning the differential volume or surface elements used in the integration process, they are evaluated using their associated differential domains in the natural coordinate space and the Jacobean matrix of transformation. Since the coordinate transformation equation is :

$$\begin{bmatrix} dr \\ r\,d\theta \\ dz \end{bmatrix} = \begin{bmatrix} \frac{\partial r}{\partial \xi} & \frac{\partial r}{\partial \eta} & \frac{\partial r}{\partial \zeta} \\ \frac{r\,\partial \theta}{\partial \xi} & \frac{r\,\partial \theta}{\partial \eta} & \frac{r\,\partial \theta}{\partial \zeta} \\ \frac{\partial z}{\partial \xi} & \frac{\partial z}{\partial \eta} & \frac{\partial z}{\partial \zeta} \end{bmatrix} \begin{bmatrix} d\xi \\ d\eta \\ d\zeta \end{bmatrix} = \begin{bmatrix} \mathbf{J} \end{bmatrix} \begin{bmatrix} d\xi \\ d\eta \\ d\zeta \end{bmatrix} \qquad (3.11)$$

then the volume integral differential element is

$$r\,dr\,d\theta\,dz = |J|\,d\xi\,d\eta\,d\zeta \qquad (3.12)$$

Combining the above mentioned formulae, the volume integration will be written as :

$$\iiint_{V_e} f(r,\theta,z)\ \ r\,dr\,d\theta\,dz \ = \ \int_{-1}^{1}\int_{-1}^{1}\int_{-1}^{1} f(\xi,\eta,\zeta)\ \ |J|\,d\xi\,d\eta\,d\zeta$$
$$= \sum_{k=1}^{3}\sum_{l=1}^{3}\sum_{m=1}^{3} W_k W_l W_m\ f(\xi_k,\eta_l,\zeta_m)\ \left|J_{(k,l,m)}\right| \qquad (3.13)$$

where ξ_k,η_l,ζ_m are natural coordinates of the Gauss points and W_k, W_l, W_m are their weight values. The same method is used for surface integrals in double instead of triple summation, with values of Gauss point coordinates depending on which face of the standard element in handled.

In the global assembly stage, the convective and pressure surface integral parts of the residues, which represent the interaction, will be identically canceled out to ensure conservation between elements. The normal derivative surface integrals resulting from the artificial dissipation terms are also ignored between elements in order to enhance, at least partly, the averaged continuity of the normal first derivatives (since the original FEM formulation has no means of doing so).

The resulting global matrix equation will have the same residual minimization form of the element matrix while imposing conservation of all convected variables between elements. Once the residue L_2 norm reaches a specified value, the solution for the time level stops

and the code shifts to the next one. In the present study, reaching the machine accuracy value of 10^{-16} was taken as a sign of convergence. This has been reached in a maximum of 4 iterations, converging quadratically (on a semi-log chart of L_2 .vs. iteration number, the curve takes an approximate inverted parabolic shape). Fig.(3.2) describes the flow chart of the nested loop. The outer loop is for time-marching and the inner loop is the iterative one dealing with residual minimization to account for non-linearity

3.4 - Boundary Conditions :

As discussed in Chapter 2 , the hyperbolic nature of Euler equations implies that the boundary values imposed should be consistent with the possible channels for signal propagation. For a 1-D set of Euler equations, the characteristics are found to propagate with speeds equal to the forward- and backward-moving speeds of sound, superimposed on the flow velocity. For multi-dimensional flow the active velocities were found to be the same sound speeds, superimposed on the velocity components normal to the local boundary [75,76].

The boundary condition specification depends on the boundary status as well as the velocity component normal to the boundary. Several cases are possible in this respect :

1 - For subsonic inlet, two characteristics will be coming from outside the domain. So their associated variables, or mathematical relations, should be imposed as boundary

conditions either explicitly or implicitly through surface integral terms. For isentropic flow these are the transverse velocity component in addition to the entropy and the C^+ Riemann invariant

$$s = C_v \ln \frac{p}{\rho^\gamma} \quad , \quad P = u + \frac{2}{\gamma - 1} c .$$

where u is the inlet fluid speed and c is the speed of sound. The third one is supposed to be extrapolated from inside the domain. In the Finite Element technique this is identically satisfied.

2 - For supersonic inlet, the three characteristics will be coming from outside the domain. This means that inlet section conditions will not be perturbed by any signal propagation from the inside. In this case all the characteristic variables, or any other complete set of variables, can be introduced as boundary conditions.

3 - For subsonic exit, only one characteristic will be coming from outside the domain. So its associated variable or relation can be imposed as a boundary condition. For unsteady isentropic Euler equations it is the C^- Riemann invariant

$$Q = u - \frac{2}{\gamma - 1} c .$$

4 - For supersonic exit, the three characteristics will be coming from inside the domain. This means that exit section conditions will not be perturbed by any signal propagation from the outside. In this case, no values are imposed for the variables.

5 - For wall surfaces, the no-penetration condition is imposed. However, in the case of unsteady flow with localized shock or rarefaction waves colliding with walls, the method of imposition should be strong enough to avoid flux values at walls, yet it has to avoid multiplicity in imposing the condition to avoid the numerical scheme's divergence. Since the solid surfaces encountered in the present study were found to be straight surfaces, the no-penetration condition was easily imposed in the global matrix assembly stage. Linear combination was enforced between the velocity components such that the normal component is zero. In this case the no-penetration condition is imposed only once, and all convective flux integral terms, including the continuity flux integral, were included in the matrix calculations since they vanish identically. The surface integral resulting from the artificial dissipation is ignored since it is not strong enough to impose zero normal gradient, yet it causes a non-realistic flux value in case the gradient exists.

3.5 - Matrix Solution Requirements :

To extend the work to three dimensions, matrix storage has to be considerably optimized to be able to use the available computing facilities. Although explicit schemes contribute greatly to the solution of this problem, the most cost-effective method is to use iterative

solvers, which require storing only the matrix non-zero elements. Despite the gradual approach to the final solution, the method is suitable for conventional computers and for the diagonally-dominant matrices associated with time-marching problems.

The GMRES iterative solver used in the present study was developed by Y. Saad [77] for linear algebraic problems with large size sparse matrices. The main idea is to perform an L-U decomposition only for the originally-nonzero entries of the matrix. Consequently the resulting L and U matrices are not exactly equivalent to the original matrix and the resulting solution will not satisfy the matrix equation at once. Assuming an N-dimensional space including the solution and RHS vectors (where N is the number of unknowns), the solver creates a limited number of orthonormal basis vectors, from which the solution is composed, by successive minimization of the residual vector (the difference between the combination of previous solution vectors, and the RHS). Once the residual vector is less than the specified minimum, the solution is constructed from the calculated vectors.

This solver is decoupled from the original formulation and is used explicitly for matrix equation solution - a task in which it has gained considerable reputation for its success in problems with ill-posed matrices (e.g., convection-dominated P.D.E.s of high Reynolds number fluid dynamics). It has been used successfully for steady flow problems for both Euler and Navier-Stokes equations [78], and for the present study its performance has shown improvement due to the enhanced diagonal dominance resulting from the linear time derivative terms.

4 - EXPERIMENTAL SETUP & PROCEDURE

The experimental work for the present study was carried out in the Concordia University Shock Wave Dynamics Laboratory. A variety of test cases were used to compare to the simulation of the basic phenomena encountered in the original problem (e.g., convergence strengthening, diffraction, reflection ....etc.). The test results chosen include Schlieren and pressure measurements of plane 2-D flows for validating Cartesian coordinates formulation, as well as pressure measurements of radial or 2-D axisymmetric flow for validating the cylindrical coordinates formulation.

4.1 - The Two-dimensional Shock Tube

4.1.1 - Experimental Setup :

For two-dimensional cases, a square section shock tube was used. The tube is made of seamless structural steel and has inner dimensions 2.06" x 2.06" (51 x 51 mm) and a 0.25" (6.3 mm) wall thickness. A schematic diagram of the shock tube assembly is shown in Fig.(4.1). The setup consists of four basic parts :

1. A driver section 5 feet (1.52 meter) long for high pressure, supplied with air either from the compressed air line of the building (up to 110 psig), or the air tank filled by a

reciprocating compressor available in the lab (for higher values). The idea behind a relatively long driver section is to prevent any waves reflected at driver tube end from affecting the measured flow at the critical time.

2. A driven section of equal length in which some transducer measurements are taken to calculate the incident shock velocity. Special threaded holes are available on top of the section to introduce the pressure transducers. The length of the driven section allows the shock - resulting from localized diaphragm rupture - to regain its planer shape due to transverse signal propagation. The driver and driven sections have O-ring sealed flanges. They are separated by mylar plastic diaphragms whose rupture depends on the pressure values at the two sides and the diaphragm thickness. The same flange and sealing mechanism exists between the driven and test sections. However, an extra set of pins is used to align the two sections to minimize the possibility of shock perturbation.

3. A 37.5" (952 mm) long test section in which all Schlieren photographs as well as some transducer measurements are taken. For Schlieren photographs a 5" (127 mm) long section is milled away on three sides of the test section. Two square frames are welded on opposite sides, each holding a 0.5" (12.7 mm) thick commercial glass window with the necessary clamping and sealing. The third (middle) milled part is replaced with the metal sections defining the experiment's geometry. The test section should always be broad enough to maintain the two-dimensionality of the experiment.

The driven and test sections are well sealed to allow creation of negative gauge pressure, thus increasing the shock speed, and the test section has wide outer bleed chamber with square dimensions to prevent the bled shock from reflecting and affecting the tube flow once more.

4. A 5-KV power supply unit equipped with a time-delay circuit to control the spark time for Schlieren photography. The circuit is triggered by a transducer located in the driven section, upstream of the test section. For the slit interaction experiment, the same transducer is used to trigger the oscilloscope cursors for pressure and shock velocity measurements.

Compressed air enters the shock tube via a copper tubing through the control panel. The pressure in the driven section could be atmospheric or vacuum, depending on the Mach number required in the experiment. Vacuum pressure is provided by an electrically powered vacuum pump via a connection to the driven section, through the control panel, by copper tubing. The pressure supply is measured by two control panel gauges, one measuring absolute pressure with operating range (0-100 psia) for the driven-test sections, and another measuring gauge pressure with operating range (0-300 psig) for the driver section.

The driven section is evacuated to different values, while the driver section is filled slowly until the diaphragm ruptures. The driver pressure rupture value was maintained as much as

possible by using the same diaphragm type and careful handling of the driver section filling process. It should be mentioned, however, that according to the Riemann problem formulation, the pressure behind the shock is lower than the driver pressure, which means that the resulting error in its value will be smaller. Furthermore, it is evident from the Rankine-Hugoniot pressure ratio equation that the sensitivity of the shock Mach number to variations in pressure ratio is small.

Near the downstream end of the driven section, 3 transducers were installed. One is used to trigger the oscilloscope and the other two to measure the incident shock speed. For the slit bleeding experiment, the attenuated shock speed is measured using 2 more transducers located 20" downstream of the slit zone on the test section. They are not installed for the ramp experiment, since the flow does not reach their location. For the ramp test case, and since it was only possible to have one photograph for each experiment, the Schlieren system was adjusted with successively increasing lag time relative to the trigger transducer.

The available tube did not have diaphragm piercing mechanism similar to that of the cylindrical shock tube. However, it was found that for the same diaphragm type, the high pressure value is almost the same at rupture. So the diaphragm type (instead of the high pressure) and the low pressure value became the control parameters, so as to reach the range of supersonic flow Mach number behind the incident shock. The piercing mechanism

will be essential if the used diaphragms rupture at pressure values higher than the available operating range for the driver pressure.

4.1.2 - Test Section Options :

Fig.(4.2) shows the configuration of the test section, whose inner outlines depend on the phenomenon to be tested. Two have been tried using the tubes in the lab with air as the working fluid. One is for shock waves undergoing a contraction through an incline, and the other is for shock waves being decelerated through side slit bleeding.

For the bleeding experiments, two L-shape aluminum wedges, with 15 ° edges, were employed to form the slit. The upstream wedge was fixed while the other was varied in dimension to control the slit width. Ostrowski's Schlieren results were used to visualize the flow and shock structure for numerical code validation. However, in the present work, experiments were also carried out to determine the shock attenuation as a function of the geometrical parameter, namely the slit-channel width ratio.

For the ramp reflection-diffraction experiment, the two wedges were replaced by an L-shape 15° wedge and a supporting U-shape panel. The wedge geometry represents the 50% reduction in area of the original cross section through a 15° slope, while keeping the 2 " (51 mm) breadth constant. For facilitating Schlieren photography, the side walls are made of commercial glass (as opposed to metal plates, in case no photography is needed).

4.2 - The Axisymmetric Cylindrical Shock Tube

4.2.1 - Experimental Setup :

Fig.(4.3) shows the general layout of the axisymmetric shock tube assembly. The axisymmetric air-to-air shock tube is made of seamless steel tubing with 7 mm wall thickness. The inner diameter of the cylinder tube is 154 mm and the total length is 5.81 meters. This shock tube consists of three sections :

1. A 2 meter long driver section which is connected to a compressor or a high pressure compressed air line available in the lab. The driver and driven sections, separated by a mylar plastic diaphragm, are assembled using standard and well centered flanges bolted by eight bolts. In order to prevent air leakage and to assure sealing, O-ring seals were installed in the raised face of the flanges, connecting both driver and driven sections.

2. A 3.81 meter long driven section which is connected to a vacuum pump to create negative gauge pressures. This section is subdivided into two parts: one 2.74 meter long tube followed by another 1.07 meter long tube housing the three-stage conical contraction and is closed by a cover flange. A two-part aluminum inner tube with 10 cm outer diameter and 1.83 meter length is mounted concentric with the driven section

of the shock tube. This inner tube combination has two purposes: The first splits the originally produced normal shock wave into an inner plane wave and an outer (annular) wave, and the second houses the bleed test section at its end. These two aluminum parts are supported at the middle by an outer aluminum flange of thickness 40 mm (recessed in the shock tube inner surface) and a ring with 100 mm outer diameter (recessed in and matching the aluminum tube outer diameter) and 76 mm inner diameter. Four fins with 10 ° wedge angles at both sides, are placed between the flange and the ring in order to provide the support (as webs) while minimizing the disturbing effect on the shock front shape. A 5 ° chamfer is machined at the upstream end of the aluminum inner tube in order to minimize any disturbance to the annular part of the plane shock, whose effect might show later at the inlet condition.

3. A test section located downstream of the driven section. At the extreme end of the shock tube, a 3-stage incremental area contraction, designed by Wu et al. [37], is fixed at the end of the aluminum inner tube. Its geometry is defined using the outer machining of the test section corner and the inner machining of the end cover flange. The contraction's contour is designed to turn the annular plane shock by 90 ° to form a cylindrical converging one. The inner bore of this cover flange is designed to accommodate a fine quality glass window, which is sealed by a rubber gasket of 0.5 mm thickness. In the present study, where the bleed effect only is to be studied, a 78.7 mm diameter circular disk with an adjustable axial location was used for the purpose

of defining the constant width test chamber by adjusting its surface to be parallel to that of the end cover flange.

Compressed air enters the shock tube via a copper tubing through the control panel. The pressure in the driven section could be atmospheric or vacuum, depending on the Mach number required in the experiment. Vacuum pressure is provided by an electrically powered vacuum pump through a connection to the driven section by a 75 mm steel pipe followed by copper tubing. The pressure supply is measured by two gauges, mounted on the control panel, one measuring absolute pressure with operating range (0-760 mm Hg) for the driven section, and another measuring gauge pressure with operating range (0-100 psig) for the driver section.

At the downstream end of the shock tube and upstream of the area contraction, a transducer was installed to trigger the oscilloscope. In order to gain precise control of the bursting pressure, induced rupture of the diaphragm by mechanical or electrical means is preferable over the natural bursting by pressure alone. The piercing mechanism incorporates a sharpened plunger driven by compressed air. This plunger was put concentric with the shock tube and is controlled by a switch located on the control panel.

4.2.2 - Test Section Options :

In previous work the test section was bled to atmospheric air, which limited the available pressure ratio. At present, a new test sections is available to facilitate lowering the pressure of the driven section, thus obtaining higher pressure ratios and Mach numbers. The inner tube of the annular shock tube section was made to contain a bleed chamber which absorbs the diffracted part of the shock wave. A schematic layout of the new section is shown in Fig.(4.4). The end cover flange has two options: either a glass window in the test section for visualization of the shock front shape using the Schlieren system, or a solid aluminum cover with transducer threaded holes for studying pressure history and deducing shock velocity accordingly.

The set of four transducers was placed at different radii in the cylindrical chamber ($1.4^{"}$, $0.95^{"}$, $0.55^{"}$ and $0.15^{"}$, respectively) and activated using a fifth upstream trigger transducer to measure the shock pressure history down the tube radius. Bleeding takes place at an outer radius of $1.475^{"}$, with a slit width of $0.1^{"}$. The results show the anticipated sudden jumps in pressure for the incoming wave and the reflected wave passing by the transducer location. From these results, one can measure the pressure ratio across shocks. It is also possible to measure time between successive incident shock jumps and compare it to the numerical and theoretical results.

4.3 - Monitoring Equipment

4.3.1 - Schlieren System :

The Schlieren system is used to photograph shock wave fronts at any time, depending on the fact that refractive indices of gases depend on their density gradients. Therefore, if a plane fluid flow is subjected to a normal light beam, it creates dark and light zones whose intensity depends on the density gradient contours and, consequently, give an indication about shock structure.

A conventional Schlieren photography system was employed to photograph shock waves in the 2-D ramp problem. This system, whose components are shown in Fig.(4.1), consists of a 5-KV spark source, a condenser lens, two parabolic mirrors, a plane mirror, a knife edge and a camera. The spark source is charged by a high voltage power amplifier and operates at pulse value less than 0.1 microseconds. In this system, the light generated from the spark source becomes parallel following its reflection from the parabolic mirror, located at the focal length distance from the source. The other parabolic mirror reflects all incoming rays at the test section, and the flat mirror receives and transmits all the light rays to an open shutter camera.

The spark source and delay circuit were triggered by a transducer placed in the driven section, upstream of the test section. The size of the light source was limited to 0.5 mm x

0.5 mm by edges of four razor blades. In the adjustment stage, a continuous light source - whose light beam follows the same path as the spark's - was used to ensure the alignment of different system components.

4.3.2 - Pressure Transducers :

A set of Piezotronics PCB 105A pressure transducers was used for shock tracking and measuring the shock initial and final (attenuated) velocities. The transducer geometry and performance characteristics are presented in Fig.(4.5). In the 2-D slit bleeding problem, two transducers were located 18" , 24" upstream of the slit edge to measure the incident shock velocity, and two others were located 20" , 24" downstream of the slit edge to measure the attenuated shock velocity (after regaining its original 1-D shape). Signals are processed using a 12-channel Piezotronics PCB Model 483B07 amplifier, and then transmitted to a 4-channel Tektronix TDS 420 digitizing oscilloscope to calculate the shock location history.

The first case which was tried was the simple one-dimensional shock tube problem (Riemann problem) used for calibrating the pressure transducers. The interest has been confined to the values of thermodynamic variables in the driven section behind the moving shock. Far enough from the punctured diaphragm, the wave becomes a plane shock wave with time-invariant state (relative to a frame moving with the shock) and the Rankine-Hugoniot relations can be used to calculate the expected pressure.

Experimentally, several trials were conducted - using the 2-D square shock tube without bleeding - for various driver-driven pressure ratios and interchanging the transducer locations, while the resulting shock motion history was recorded using the oscilloscope. The transducers were placed 6" apart with the upstream one acting as the trigger. The shock speeds were calculated by dividing the distance between the various transducers over the time between successive pressure jumps measured from the transducers' outputs.

A sample of the oscilloscope output is presented in Fig.(4.6). The equal distances between transducers are clearly manifested through the equal time intervals between jumps in the channels' output rises, thus indicating uniform shock speed in the constant area driven section. The theoretical pressure rise across the shock, Δp, is calculated using the Rankine-Hugoniot relations:

$$\Delta p = p_1 \frac{2\gamma}{\gamma - 1} \left(\frac{V_{sh}^2}{c_0^2} - 1 \right) \tag{4.1}$$

where :

p_1 = pressure ahead of the shock

c_0 = sound speed ahead of the shock

V_{sh} = shock speed

Measuring the voltage output from each of the four transducers, it was possible to obtain the required calibration curves for each of the transducers used. The results are presented in Fig.(4.7) for the transducers used in the present study.

Similarly, the transducers are used - although along a smaller distance - to monitor the shock motion down the cylindrical implosion test chamber. Theoretically, the rapid change in the Mach number requires relying only on the local transducer to measure the local shock speed. In this case, calculating the local Mach number is based on pressure jump measurement (which makes its output quality extremely crucial for predicting the Mach number). Another theoretical method is using the oscilloscope's shock radius-time output and an assumed radius-time relationship. For example, the power-law form of the shock Mach number - radius relationship

$$M = C_1 * (R)^{-n} \tag{4.2}$$

can be modified to obtain the radial location history by separation of variables and integrating :

$$(R)^{n+1} = -k * t + C_2 \tag{4.3}$$

where C_2 is an integration constant and k is equal to $(n+1)(C_1)\,c_o$.

However, from the practical point of view, results for such a small duration are susceptible to defects in the transducer's performance parameters, namely its lag time (between 1 and 2 microseconds). Furthermore, in case the transducer is near the center, the flow exhibits high rates of pressure rise and pressure drop following the passage of the reflected shock. This change of trend is expected to yield lower peaks in the pressure curve at the moment of shock reflection since the transducer can not cope with such a change in pressure in a very small time duration (1-2 microseconds). Therefore, the pressure measurements are directly used, without further processing, for comparison with the equivalent numerical or analytical values. An initial adjustment is performed for the two data sets to have the same rise starting time, then the pressure points are obtained from oscilloscope output for comparison with other results. A sample of the oscilloscope output is presented in Fig.(4.8) for cylindrical shock convergence with no bleed.

5 - RESULTS & DISCUSSION

5.1 - Shock Wave Reflection & Diffraction in a Ramp

The first case to be tested was the process of shock strengthening through a 15 ° ramp ending with a straight duct of half the upstream cross sectional area. This test case was chosen for the developed numerical scheme due to its simple geometry, allowing a clear visualization for the phenomena of shock reflection and diffraction, and facilitating a closed form solution to compare to. In the present case, with an initial shock Mach number of 2.106 and a 15° ramp, Mach reflection took place due to the small angle used.

5.1.1 - Experimental Results :

All tests were run using air as the working fluid. The test section used is presented in Fig.(4.2b). The Schlieren system was adjusted with successively increasing lag time relative to the trigger transducer. The history of shock diffraction and reflection can be visualized in the set of photographs shown in Fig.(5.1). Photograph (5.1a) shows the incident shock, whose measured Mach number was equal to 2.106, after passing by the concave edge and undergoing the Mach reflection process, thus creating the reflected shock and the Mach stem. Due to the fact that Schlieren photography recognizes lines of noticeable density gradients, it was also possible to visualize the reflected shock and the slip stream in photographs (b-d). The experiment shows that the Mach stem is

approximately straight near the triple point, which agrees with the Ray-shock approximation for strong shocks concerning Mach reflection.

Photograph (e) show the shock approaching the ramp end. It is worth noting that in the case dealt with, the Mach stem reaches the convex edge at the same instant as it nearly dominates the whole flow cross section. This implies that the incident shock has been completely transformed into a Mach stem, and that the reflected shock has been completely re-reflected at this particular instant, as seen at the figures. As a result, the angle χ between the shock-shock and the horizontal is approximately $30°$.

Photograph (5.1f) shows the "transient" straight shock, with Mach number equal to the Mach stem value, being aligned to its original direction through two new processes; a diffraction process at the convex edge, and a Mach reflection process at the opposing straight wall.

5.1.2 - Analytical Results :

The Ray-shock Theory treatment was previously presented in Chapter 2 for the two basic processes, as it provides a basis to compare to both experimental and numerical treatments [25,64]. According to the initial shock with $M_0 = 2.106$, the $15°$ Mach reflection process results in a stem Mach number, M_{s1} , approximately equal to 2.345, at the inclined surface

(Fig.(5.2)). The shock-shock has an angle of 14.79° with the incline (χ is approximately 30° with the horizontal), which is the same value observed in the experiment.

At the downstream convex corner, a diffraction of 15° is introduced to the fully-developed inclined straight shock, producing a fan of characteristic straight lines centered at the corner. For the wall downstream of the edge, the Ray-shock Theory predicts the first characteristic to make an angle, m_1, equal to 22.5° with the initial shock direction (the incline in our case), and a new diffracted shock Mach number, M_{d2} , approximately equal to 2.08, with the last characteristic having an angle of 22° with the horizontal. For the opposing straight wall, the same 15° Mach reflection procedure followed previously is introduced to the shock, which in turn produces a new upper wall stem Mach number, M_{s2}, equal to 2.64.

5.1.3 - Numerical Results :

The domain covered is shown in Fig.(5.3). It included the upstream straight section, the ramp section and the downstream straight section with length ratios of 2 : 2 : 1, respectively. The grid was composed of trilinear 8-node elements of uniform length in the axial direction to improve the shock resolution. In the normal direction, a gradually increasing length with fixed expansion constant was used, with the grid refined near the edges, where rapid change in properties was anticipated. The third dimension was neutralized during the assembly process by imposing invariance in that direction.

As boundary conditions for the problem, no-penetration was imposed on all the wall nodes. For the convex corner, only the continuity flux integral was canceled on its two adjacent surfaces, while its variables were left to float (to allow the velocity vector to take direction with the minimum error possible). For the concave corner, the velocity was set to zero to stabilize the end of the reflected shock at the corner (which is identical to the real situation). An initial solution pertaining to the shock Mach number of 2.106 - which was obtained experimentally - was calculated using the one-dimensional flow code, and introduced at the starting time level. Numerical solution advancing with time steps of 10 microseconds was calculated, with the thermodynamic variables recorded and compared to the experiment.

The numerical results for the same problem are presented in Fig.(5.4). Evidently, the shock thickness is not as it is in reality due to limitations of the grid selectivity (for the infinite Fourier modes present in a sharp discontinuity). For this reason the shock location will be considered the contour line corresponding to the mean value between the unperturbed fluid ahead of the shock and the final value behind the shock thickness.

Numerical results are presented in Fig.(5.4a-d) for the Mach reflection process. It is evident that the evolution of the straight triple point locus - or "shock-shock" in Ray-shock Theory terminology - approaches a fixed direction as assumed in the theory's treatment. For calculating the angles, measurements were done on figures where the shock

was far enough from the concave corner, as they provide a better definition for the geometry of the Mach stem. As the Mach stem advances and its area gets bigger, the numerical and experimental values of shock-shock angle converge to the same value of approximately 30°. It is understandable, however, that availability of more computing power will cause a significant improvement for the shock resolution. The first stem Mach number M_{s1} is found to be equal to 2.39, which is slightly higher than the analytical solution value of 2.345.

On the other hand, the diffraction and new Mach reflection can be visualized on Fig.(5.4e). In agreement with experimental results, their simultaneous occurrence is almost present, as well as their effect on turning the shock to its original axial direction. The expansion fan, defined by the density contour lines in the figure, is centered at the convex corner. This is consistent with the anticipated uniform change of fluid properties across the fan, provided that the driving flow behind the shock is uniform. The new Mach stem is found to have a shock Mach number of about 2.73 as opposed to the analytical value of 2.64. The differences between numerical and analytical results are partly attributed to the slight peaks created in the solution due to the discretization of sudden discontinuities (like shock waves). Differences are also expected due to the nature of the Ray-shock treatment, which is purely based on shock kinematics.

Furthermore, an additional grid-dependence test was carried out for the numerical solution. This test is carried out to ensure the ability of the numerical scheme to approach

a grid-invariant solution once the grid refinement approaches the continuum state. The grid in the ramp and downstream sections were introduced with variable element numbers in both axial and lateral locations, specifically 150 x 50, 300 x 70 and 540 x 90 elements, respectively. The grid in the upstream section was varied accordingly in the lateral direction. Its axial configuration had 110 elements and was kept invariant so that the same initial solution can be introduced to all grid options.

The test results for the three grids are shown in Fig.(5.5) for the density contours after 30 time steps from the initial state. The general overview, specially of the last two grid solutions, shows that the solution is becoming more and more invariant with grid refinement. The first observation is the expected effect of grid refinement on the thickness of the incident shock-Mach stem front. A similar observation is the relative improvement in defining the discontinuity at the secondary reflected shock. This gives a good indication about the numerical simulation efficiency since the reflected shock in the present case is relatively weak (due to the small deflection angle) and the grids were not too much refined in the lateral direction. Another encouraging note is the emerging definition of the slip line starting at the triple point, which is hard to capture by any numerical scheme due to its small gradient values, thus requiring adaptive grid refinement.

5.2 - Shock Wave Interaction with a Narrow Slit

An initial description for the process of shock-slit interaction was presented in Chapter 1. However, experimental studies by Skews [61,62], Wu et al. [63] and Lee et al. [65] have shed more light on the complicated nature of the interaction process and the existence of more elements in the configuration of both the diffraction and Mach reflection. Another factor is the growing interest in numerical methods due to the new developments available in computers, as well as their increasing flexibility in simulating flows over complicated domains.

The present work's experimental and numerical results are preceded with the Schlieren photographs obtained by Ostrowski [64] for an initial shock Mach number of 2.33. The results yield a valuable description for the diffraction through side bleeding, while comparison to the present work's results facilitates judging the code's efficiency.

The photographs in Fig.(5.6) describe stages of the shock wave interactions with the wedged slit. Photograph (5.6b) shows the plane shock diffracted as it exceeds the upstream edge into the slit, with the expansion wave starting to form. The wave is supposed to follow the expansion fan lines, which are actually the loci of the points of intersection between the incident shock and the acoustic waves created when fluid passes the edge. Since the flow is supersonic, the resulting expansion wave is enclosed within the domain of characteristic lines, with the first line as an envelope emanating at the upstream

edge. As time progresses this fan spreads out into the channel and becomes partly responsible for the attenuation of the shock. The fan splits the shock into the incident straight part, and the nearly cylindrical expanding part which curves around the edge to maintain contact with the wall. Consequently, a contact surface is formed between the fluid domains affected by the two waves. The contact line forms a curve starting at the demarcation point between the incident and expanding shocks. Due to the inability of the flow behind the shock to negotiate the sudden enlargement, a slip line with an associated vortex starts to form at the edge. As the outside frontal area for the diffracted initial shock gets bigger, the shock and flow Mach numbers become smaller. According to shock diffraction experiments by Skews, and for the diffracted flow behind the shock to cope with this deceleration, a new (secondary) shock is gradually formed between the upstream edge and the diffracted shock. This shock should be approximately bounded by the slip line and the last characteristic line (the terminator).

Photograph (5.6c) shows the flow shortly after the shock reaches the downstream edge of the slit. The diffracting shock is reflected from the downstream edge, producing a reflected shock inside the duct (which also spreads out into the flow to terminate the weakening effect of the initial expansion) as well as the "Mach stem", which is the first phase of the new attenuated shock. For supersonic flow and due to a some degree of downstream edge bluntness, the reflected oblique shock remains detached at the edge, and extends through the bleed jet formed at the outer side of the slit. The detached shock results in pressures higher than the values behind the diffracting shock. An expansion fan,

centered at the downstream edge, forms in order for the fluid to match the fluid pressure outside the duct. At the upstream edge, the trio of the slip line, the terminator and the secondary shock is clearly visualized, with a new extension of the shock at the duct side.

Photograph (5.6d) show the flow at a later stage. The detached shock and the expansion fans after the flow are more distinct. Because of the outside frontal area increase, the shock Mach number and the flow Mach number become smaller. For the expanded flow behind to adjust to this factor, the secondary shock appears between the downstream edge and the diffracted initial shock front. The nucleus of a "stagnation zone" can be visualized between both shocks. Inside the duct, the three elements of the Mach reflection are more clear, so is the slip line splitting fluid affected by the incident-reflected shock couple from that affected by the Mach stem. The situation is better defined in photograph (5.6e) where the downstream edge is the center of the detached shock backed with an expansion fan "trio" similar to the one at the upstream edge, bounded by the detached shock, the secondary shock and a new terminator and slip line close to the edge surface.

The photographs (5.6f,g) provides an idea about the flow while approaching its final steady state. At the upstream edge, the full expansion fan, ending with the terminator, as well as the slip line can be visualized, and a Prandtl-Meyer expansion exists at the characteristics zone. At the downstream edge, the detached compression-expansion couple and the slip line define the flow zone. The external traveling waves move far away from the slit and their influence eventually vanishes. A steady inclined fluid jet, whose

geometry is defined by the abovementioned set of waves as well as their interaction, is established at the slit.

Inside the duct, the expansion wave, the reflected shock and the original expansion fan will undergo multiple reflections from the walls as the shock propagates down the tube. The characteristic line structure inside the duct can be partly visualized in photograph (5.6i). The dissipation of the expansion fans will cause a gradual shock weakening. Eventually the expansion waves become diffused while overtaking the shock and the attenuation process becomes smooth but at a slower rate.

5.2.1 - Shock Attenuation Experimental Results :

A series of experiments were carried out for four slit-duct width ratios (0.25, 0.5, 0.75, 1.0, respectively) as well as a wide range of shock Mach numbers (ranging between 1.2 and 2.5). All tests were run with air as the working fluid. Fig.(4.2a) shows the test section, which consists of the tube section of width 2" and the large bleed section. These sections are separated by two 15° wedges to yield the abovementioned slit-duct width ratios. A set of four transducers, two upstream and two downstream, were used to measure the shock speed before and after the slit. The oscilloscope traces were simultaneously activated using a fifth upstream trigger transducer, as shown in the figure.

To ensure reasonable repeatability of the test results, extreme care was taken in setting up the driver and driven pressures and the loading rate of the driver pressure. For any given initial conditions, a sufficient number of trials were carried out (at least five). In most of the cases, four points were considered repeatable (within 0.5 % variation) to be averaged and used for computations.

The results of the measurements are presented in Fig.(5.7) for the attenuated shock Mach number M. The figure shows the attenuation ratio, M/M_0, versus the incident Mach number, M_0, with the slit-duct width ratio, W/H, as a parameter varying between 0.25 and 1.0 according to the experiment setup. The attenuation did not exceed 8% over the covered range of shock Mach numbers and slit-duct width ratios. The general trend shows a high rate of variation in the attenuation coefficient at low shock Mach numbers (with low subsonic flows behind the shock). However, for higher Mach numbers, the flow exhibits a more dominating effect for the width ratio rather than the Mach number. Attenuation becomes nearly invariant over a wide range of Mach numbers high subsonic flows behind the shock ($M_0 < M_{0\,cr} = 2.068$). As M_0 increases beyond the critical value, the coefficient M/M_0 then increases slightly. This trend will be explained later in the analytical solution.

In agreement with Ostrowski's conclusions, the results that have been presented so far give the indication that increased attenuation due to reflections and the corresponding

effect of slit width is relatively small within the practical operating range of Mach numbers and width ratios.

5.2.2 - Numerical Results :

The computational domain for the problem is shown in Fig.(5.8a), which includes both the tube and bleed sections. The tube section length was taken as 10 times the tube width to give the shock enough distance to reach the final 1-D attenuated state. The slit was located at only twice the width from the inlet section because the zone between them is not supposed to undergo any deviation from the incident steady supersonic flow (for the used shock Mach number value). The bleed section was chosen to be 4 times as wide as the tube to avoid any disturbance created by reflected waves from the bleed chamber.

The grid was composed of trilinear 8-node elements whose axial dimensions depend on the zone covered, with the most refined part in the slit zone as shown in Fig.(5.8b). In the other two zones, elements had an expansion coefficient depending on the zone length and the expected variation in flow properties. The lateral direction element size was calculated with lower expansion coefficients for the tube section than that for the bleed section. However, the percentage expansion was kept below a maximum value of 3% to have the best possible results in the vicinity of the edges. Far inside the bleed section, the flow is not required to be accurate as long as it is far from disturbing the tube flow.

As boundary conditions for the problem, no-penetration was imposed on all wall nodes. For the upstream edge, only the continuity flux integral was canceled on the two surfaces adjacent to it while its variables were left to float. For the downstream edge the velocity was set at zero to impose the presence of a detached shock facing that edge at later stages. An initial solution pertaining to the shock Mach number of 2.33 was calculated using the one-dimensional version and introduced at the starting time level. Numerical solution advancing with time steps of 1/400 of the reference time (tube length / inlet velocity) was calculated while recording the values of thermodynamic variables at every tenth step.

Figures (5.9a-d) describe the numerical results at different time levels. Fig.(5.9a) shows the plane shock diffracted as it exceeds the upstream edge into the slit, with the expansion fan starting to form. The fan splits the shock into the incident straight part, and the nearly cylindrical expanding part which curves around the edge to maintain contact with the wall. The peaks in the density contours differentiate between the density gradient across the shock and that inside the expansion domain. In the bleed chamber, the slip line starting at the upstream edge is noted by the closely spaced group of contour lines originating at the edge, with an associated vortex as closed density contours. The vortex size is affected by the artificial dissipation introduced for shock capturing, which depends on the grid refinement and the available computing power. Since the particle velocity is assumed to be supersonic, the expansion fan remains attached to the upstream edge. As the outside frontal area of the diffracted shock gets bigger, the flow and shock Mach numbers become

smaller. Accordingly, another (secondary) shock is gradually formed behind the original diffracted shock.

Fig.(5.9b) shows the flow shortly after the shock reaches the downstream edge of the slit. The diffracting shock is reflected from the downstream edge, producing the reflected shock and the Mach stem. Due to the Mach stem lagging behind the incident portion of the shock, shock curvature is anticipated and can be visualized in the vicinity of the triple point. For supersonic flow and due to downstream edge bluntness, the reflected shock links with the similar one at the outside to form a standing detached shock at the edge. This will trigger an expansion fan, centered at the same edge, for the fluid to match the original shock outside the channel. The outgoing closely-spaced group of contour lines, emanating at the downstream edge, defines the boundaries of the outside detached shock and the outside expansion zone.

Fig.(5.9c) show the flow at a later stage. The detached shock and the expansion fans after the flow are better defined. Because of the outside frontal area increase, the shock Mach number and the flow Mach number become smaller. For the expanded flow behind to cope with this effect, the secondary shock starts formation between the downstream edge and the diffracted initial shock front. The stagnation zone can be visualized between both shocks as the contour line for the local maximum density value. Inside the duct, the reflected shock contours link with those of the expansion fan, thus dividing the internal domain ahead of the upstream edge into three zones: the first affected by the expansion

fan alone, the second by the fan-reflected shock, and the third (incident) affected by none of them.

Fig.(5.9d) shows the outer slit zone a few time steps later. A slip line starts at the upstream edge of the slit, and ends at a slightly detached shock at the downstream edge, followed by the expansion zone. The original and secondary diffracting shocks are more clear.

Inside the duct, the expansion wave, the reflected shock and its associated expansion fan will undergo multiple reflections from the walls as the shock propagates down the tube. Thus the attenuation will proceed with either sharp jumps (corresponding to the arrival of the reflected shock-shocks at the wall), or gradual increase (corresponding to the reflected shock). The expansion fans in general will cause a gradual weakening. Eventually the expansion waves become diffused while overtaking the shock and the attenuation process becomes smooth but at a slower rate.

Fig.(5.10) shows the shock Mach number versus shock location on both flat and slit surfaces for the width-height ratio, W/H = 1 . At the slit wall, the sudden drop and rise correspond to the diffraction and Mach reflection, respectively. The flat wall remains unchanged until the arrival of the expansion fan. The slit side starts a gradual decrease which can be attributed to the effect of the expanding reflected shock, as well as the fan created at the downstream edge (behind the standing shock). At the flat wall, the gradual

decrease corresponds to the effect of the expansion fan while the rise corresponds to the arrival of the shock-shock. The diffused rise can be attributed to the effect of the Mach reflection's reflected shock, whose effect was not taken into consideration in the Ray-shock treatment (which produces sharp jumps upon arrival of the Mach stem). However, the diffusion partly gives an indication about the numerical method's effect on the resolution of shock-shock simulation.

Furthermore, the frequency of the reflections - and hence the attenuation rate - will increase with decrease in duct width, as seen in Fig.(5.11) for the same case and a new value of $W/H = 2$. In terms of the slit width, the first reflection of the expansion fan at the flat wall is seen to have started earlier than before the downstream edge. In general, the reflection cycle (defined by the distance between successive intersection points of the two curves) is taking a shorter distance and the attenuation rate (defined using the envelope of the two curves) becomes larger. This is consistent with the fact that enhancement of the expansion wave diffusion hastens attenuating the wave.

The experimental and numerical results for the initial shock Mach number of 2.33 are presented in Fig.(5.12) for the attenuation coefficient M/M_0 versus the slit-duct width ratio W/H. It shows good agreement between experimental and numerical results despite the difficulties encountered during measurements. The initial value approaches unity for zero slit width, and decreases monotonically as the width increases. This is consistent with the anticipated effect of the width ratio as a measure of percentage loss in mass,

momentum and energy fluxes. As the slit width increases, the expansion fan is more diffused and reflected (in case of wide slit) and the diffracted shock becomes weaker upon reaching the downstream edge. This results in a weaker shock system after the edge and eventually a more attenuated final state.

5.2.3 - Analytical Results:

For the purpose of comparison, a simple solution model was introduced for the shock-slit interaction problem for shock Mach numbers > 2.068 (supersonic flow behind the shock). The solution is based on the assumption that, after a certain time duration, a fully developed steady supersonic flow will take place at the slit zone. Accordingly, a portion of the flow expands gradually from inside to outside the duct, while the rest expands to occupy the full duct width downstream of the slit. The flow in the slit zone can be solved using the steady Method of Characteristics to determine the percentage of the initial flow which is not bled. Once the artificial "duct" geometry has been approximately defined, then the CCW-based A-M relationship is used to calculate the attenuated Mach number.

For low subsonic particle Mach numbers, the zone inside the duct and adjacent to the slit allows signal propagation in all directions. The flow field is brought to a final state matching the pressure ratio across the slit. For this case there is a noticeable effect for both the shock Mach number (a measure of the pressure ratio across the slit) as well as the slit-duct width ratio (a measure of the loss amount as compared to the total initial flow).

As the incident shock Mach number gets higher, the bled mass flow increases until it reaches a maximum state that corresponds to choking conditions of the bleed jet. This explains the initial decrease in the attenuation ratio as the incident shock Mach number increases, until it reaches a minimum value before it increases again when supersonic conditions prevail.

Higher than the critical value, the particle flow becomes supersonic and the attenuation becomes dependent on the characteristic wave structure at the slit, which still depends on the slit-duct width ratio and the shock Mach number. For the critical shock Mach number of 2.068, the leading characteristic angle starts with a value of 90° with the flow direction (corresponding to a sonic particle flow behind the shock) and decreases gradually with further increase in the Mach number value (Fig.(5.13)). The same observation holds for the other fan lines (provided that they are kept corresponding to the same deflection angle values). This implies that with increasing the shock Mach number, the streamlines start downward curvature at a location further downstream of the upstream edge. By reverse drawing of the last bled streamline (passing by the downstream edge), it is noted that increasing the shock Mach number results in that streamline originating from a lateral location closer to the slit side. Consequently the non-bled portion of the initial flow becomes greater. From the A-M relationship of the CCW theory (2.24,25):

$$\frac{M^2 - 1}{M_0{}^2 - 1} = \left[\frac{A_u}{A_0}\right]^K \quad , \quad \frac{M}{M_0} \equiv \left[\frac{A_u}{A_0}\right]^{\frac{K}{2}} \quad \text{for strong shocks} \qquad (5.1)$$

where A_0 is the original duct area, A_u is the upstream non-bled part of the original area, M is the final attenuated shock Mach number, M_0 is the incident shock Mach number and K is the averaged Chester function (varying between 0.5 and 0.394). Since the values of the exponent are less than unity, it is concluded that the attenuation coefficient increases slightly with increasing the shock Mach number. At high shock Mach numbers, the shock structure does not exhibit too much dependence on the Mach number as much as it does on the geometrical parameters, because the characteristic angles approach their asymptotic values. The following results are tabulated for shock Mach numbers higher than critical value:

M_0	M / M_0			
W/H =	0.25	0.5	0.75	1.0
2.1	0.98665	0.97252	0.9575	0.94144
2.33	0.98717	0.9736	0.95925	0.9439
2.5	0.987688	0.9747	0.96098	0.9464

The results show that the slit-duct width ratio is a more dominant factor than the incident shock Mach number, which is the same trend observed during the experiments. For high shock Mach number, the attenuation ratio M/M_0 increases slightly.

Based on the abovementioned approximate model, the third set of values is presented for Ostrowski's test case in Fig.(5.12). The results were found to be slightly higher than the experimental and numerical results. The reason for such differences is due to the fact that the Ray-shock Theory is based on shock kinematics, and not on the full dynamic Euler equations employed in the numerical scheme.

5.3 - Cylindrical Converging Shock Wave Bleeding

In view of the requirements previously mentioned in Chapter 1, the need has arisen to study the effect of side bleeding on the converging shock propagation. The available studies concentrated on examining the behavior of an already non-uniformly perturbed shock to have an idea about the resulting non-uniform convergence history and eventual instability. To augment the past work, the present study focuses on the bleeding process itself (without tangential variation) to have a clearer idea about its attenuating effect on the convergence history. Furthermore, conclusions were compared to the previously established rules for plane shocks to determine whether or to what extent it is feasible to unify these rules.

As an extension to the 2-D problem of shock-slit interaction, the present work explores similar cases for the cylindrical converging shocks where the radial coordinate's effect of front area reduction supposedly results in an increase in shock strength. For the purpose of

isolating the radial convergence effect, the (r , z) computational domains used were identical to those used in the previous section for plane 2-D cases. The plane and axisymmetric cases were then compared. These computational domains are not identical to the geometry of the experimental setup used in the verification, which had a 90° upstream edge. However, experimental studies by Skews [61] have shown that if the flow turning angle exceeds a certain value (about 75°) the diffraction shock structure above the slip line becomes independent of the edge angle. To validate the assumption, the numerical code was tested for two similar plane flow cases with turning angles of 90° and 165°, respectively. The numerical results obtained agreed with the previous conclusion.

The numerical scheme was first tested to solve the basic radial converging shock problem with the code modified for radial motion only (no bleeding). One-dimensionality is imposed during the matrix assembly stage by retaining only the radial velocity component, while imposing invariance in lateral directions and setting the other two velocities to zero. At large radii, the radial geometry effect becomes negligible and the thermodynamic variables ahead and behind the shock wave front are relatively steady. However, this is not the case for small radii due to the front reduction and outcoming signals causing strengthening. The thermodynamic properties on the shock's two sides are related in terms of the shock Mach number using the Rankine-Hugoniot equations.

Fig.(5.14) shows the shock Mach number versus shock radius for different inlet Mach numbers. The results were found to be in good agreement with the power-law formula deduced by Guderley as well as the similar rule using the CCW theory for strong shocks:

$$M_{sh} = C_1 * (R_{sh})^{-n} \qquad \text{(Eqn.(4.2))}$$

$$(R_{sh})^{n+1} = -k * t + C_2 \qquad \text{(Eqn.(4.3))}$$

where C_2 is an integration constant and k is equal to $(n+1)(C_1)c_o$. Numerically, the exponent (n) was found to increase at smaller radii but the average value was equal to 0.195, which is in close agreement with the value of 0.197 obtained by Guderley for the self-similar solution. The change in shock strengthening rate can be attributed to the effect of numerical discretization without conditioning as opposed to the pre-assumed constant power-law assumption of Guderley's solution, which is applicable only at high shock Mach numbers throughout the whole convergence process.

5.3.1 - Experimental Results :

All tests were run using air as the working fluid. The new test section, modified for high Mach numbers, is shown in Fig.(4.4). Various experiments and numerical runs were performed to obtain a consistent set of data pertaining to the same pressure history. The experimental part was obtained using a set of pressure transducers located at radii equal to 1.4", 0.55" and 0.15", respectively. The experimental results are presented later in

Fig.(5.16), with their numerical equivalents, for slit-chamber width ratio W/H equal to 1.0. For the purpose of comparison, the pressure history is also presented at the last transducer location for W/H equal to 2.0.

5.3.2 - Numerical Results :

The domain covered included both the chamber and bleed sections and its features are identical to those of the plane problem, the bleed section length was taken as 4 times the slit width to avoid any disturbance created by the waves reflected from outside. The inlet section was located at a 5 cm radius with the inlet shock Mach number value adjusted to the value of 2.2012 in order to create a shock Mach number of 2.33 at the upstream edge (to compare the results to the 2-D problem).

The grid was composed of trilinear 8-node elements whose radial dimensions depend on the zone covered, with the most refined part in the slit zone. In the other two zones, elements had an expansion coefficient depending on the zone length and the expected variation in flow properties. The lateral direction element size was calculated with lower expansion coefficients for the chamber section than that for the bleed section. However, the percentage expansions were kept below a maximum value of 3% to obtain the best possible results in the vicinity of the edges. Far inside the bleed section, the flow simulation is not required to be accurate as long as it is not disturbing the flow in the cylindrical chamber.

As far as the boundary conditions are concerned, the same conditions used for the plane problem were used in the present case, except for one extra no-penetration condition at the chamber centerline to impose reflection. In order to yield the required shock Mach number of 2.33 at the upstream edge, an initial solution pertaining to the shock Mach number of 2.2012 at the inlet section was calculated using the one-dimensional code and introduced at the starting time level. Solution advancing with time steps of 1/400 of the reference time (inlet radius / inlet velocity) was calculated for different slit-chamber width ratios by recording the values of thermodynamic variables at every tenth step.

The pressure distribution history was extracted from the numerical results and shown in Fig.(5.15) on the flat wall at different time levels. At the slit location, the tendency of formation of a steady flow field can be visualized through the almost complete invariance of the pressure values at later time levels. At earlier time levels, however, the pressure local values decrease because of the formation of the expanded zone and bleed jet. Considering the steady supersonic inlet section conditions, the amount pumped into the chamber tends to increase the local amount of air behind the shock. Since smaller radius means less storage capacity, as the shock converges, the local pressure values increase with a rate depending on the radial location. After reflection at the centerline, the shock proceeds against the flow which was coming behind the incident state, and the shock speed tends to decrease, as concluded from the figure by measuring the distance traveled for a specified time duration.

For studying the attenuation phenomenon, the associated shock Mach numbers were calculated from the pressure jumps across shocks. In the present case, the output jump interval is avoided, and the two sides (constant value before jump and monotonic change after it) are extrapolated to the jump mid-point to form the theoretical jump, and to calculate the pressure behind the shock (and the shock Mach number) accordingly. The final attenuation coefficient was obtained using the numerical results for Mach number at the radial location of the last transducer. It should be mentioned here that the last transducer results should not simply be compared to the first transducer Mach number, but rather to the Mach number at its same location due to the no-bleed 1-D results. The ratio precludes the effect of radius difference and is taken as a measure of shock attenuation. The results are shown in Fig.(5.12) and compared to the similar 2-D plane case. The two curves are almost identical for the value W/H < 0.8 to 1.0. At higher ratios the cylindrical case exhibits slightly higher attenuation than the plane one. Although the difference is not great, this shows the inevitability of using a full numerical simulation rather than relying on unified formulas which might be reliable within a limited range.

However, for plane flow with the same dimensions of openings, the ratio W/H is a measure of the ratio of the bleed area (at the slit) to the entrapped flow area (at the downstream edge) since the width is the same. For axisymmetric flow, this is not the case due to the radial geometry and the area ratio is larger. Denoting the upstream and

downstream edge radii as (r_o) and (r_i), respectively, and noting that $W = r_o - r_i$, the area ratio between bleed and flow sections is :

$$\frac{A_{bleed}}{A_{inlet}} = \frac{\pi (r_o^2 - r_i^2)}{2\pi r_i H} = \frac{W}{H}\frac{r_o + r_i}{2r_i} = \frac{W}{H}\left[\frac{W+2r_i}{2r_i}\right]$$

$$\therefore \quad \frac{A_{bleed}}{A_{inlet}} = \frac{W}{H}\left[1 + \frac{W}{2r_i}\right] = \frac{W}{H}\left[1 + \frac{W}{H}\left(\frac{H}{2r_i}\right)\right] \qquad (5.2)$$

which is greater than the simple 2-D plane motion by an amount highly dependent the downstream radius, and directly proportional to the slit width. Since the bleed area is greater for the axisymmetric case, it is expected then to exhibit more attenuation.

To validate the numerical study, the last set of results includes both the experimental and numerical values for the pressure-time history for the transducer locations. This is shown in Fig.(5.16) for W/H = 1.0 , 2.0 . The numerical part follows the trend described earlier with the first transducer (located close to the upstream edge) undergoing a sudden jump and then gradual drop leading to a steady situation. The other transducers undergo the expected sudden rise due to the incident shock, followed by a gradual rise due to the upstream-traveling reflected waves (created by area convergence and shock strengthening), and then the sudden rise due to the reflected shock. Other than the limitations of numerical discretization or instrumentation errors, the discrepancies between numerical and experimental readings can be attributed to the numerically-omitted effect of

boundary layer on the reflected shock propagation. This effect of the boundary layer is noted where the reflected shock faces the incoming flow with the boundary layer, generated just behind the incident shock, after it has had enough time to develop. This results in pressure peak values lower than expected behind the reflected shock. This discrepancy is less noticeable at the last transducer near the center, where the time allowed for developing the boundary layer is small, and the flows before and after reflection are supposed to have low radial velocity.

As to the effect of slit-chamber width ratio, the basic differences between the last transducer's readings in Fig.(5.16) are the delay of 4 time steps (about one microsecond) in the convergence time observed for the larger slit as well as 25% smaller values for the incident and reflected peak pressures, which is consistent with the expected effect in both experimental and numerical treatments. In all, good agreement was noted between the experimental and numerical results.

6 - CONCLUSION

The present work was directed toward performing a parametric study, numerically and experimentally, for the process of shock attenuation by side bleeding in both plane and axisymmetric domains. The work investigated the fluid flow behind shocks throughout the complete bleeding process, with its associated diffraction and reflection phenomena, and ending with the attenuated final state.

The numerical part was carried out using a fully 3-D Finite Element code, written for simulating inviscid unsteady flow in various shock tube geometries. The energy equation was written in a newly used form, which introduces the pressure explicitly as one of the convected variables in Euler equations. The Newton-Galerkin discretization was used for an implicit multi-step time-marching scheme, with the Galerkin weak formulation for spatial distribution and coordinate derivatives, and an implicit three-step Gear formulation for time derivatives. 2-D cases were obtained during matrix assembly by imposing invariance and zero velocity in the third direction.

The experimental part for 2-D flows was carried out using a variable slit width square shock tube, while keeping the duct width constant. For the cylindrical shock implosion problem, a cylindrical shock tube was used, with variable width for the test chamber while keeping the slit width constant. To verify the numerical results, spark Schlieren photography was employed for flow visualization at different time intervals, while pressure

transducers were used to determine the shock velocities and pressure history upstream and downstream of the slit.

For the cases of supersonic fluid flow behind incident shocks, a new simple analytical model was introduced for the 2-D side bleeding process to compare with other results, assuming a fully developed duct flow behind the attenuated shock, and combining the steady Method of Characteristics solution at the slit zone (to define the non-bled flow profile) with the CCW theory (to calculate the attenuated shock Mach number).

The first phase of the numerical work was directed toward studying the purely 2-D bleeding process, where the radial effect is neutralized. The experimental work covered a reasonable range of slit-duct width ratios as well as inlet shock Mach numbers (for which subsonic as well as supersonic flows exist behind the incident shock). Results were presented in terms of the abovementioned system parameters.

The numerical work was then extended to the 2-D axisymmetric flow, with domains similar to those of the plane flow cases, to account for the radial convergence effect. A newly designed test section was used to bleed the flow inwards into the vacuumed driven section, thus creating stronger converging shocks. The experimental-numerical work covered the effect of slit-chamber width ratio on the convergence process.

From the present study, the following conclusions were drawn :

1. As an introductory step, the experimental-numerical work was first applied to the simple test case of shock strengthening through a 15 ° ramp. The numerical code predicted very well the shock structure for the reflection-diffraction process, and the calculated values for the stem Mach numbers were reasonably close to the analytical CCW solution. The experimental and numerical values for shock-shock angles and shock front shapes were in close agreement. Furthermore, the grid sensitivity test showed the numerical code's efficiency in approaching a grid-independent solution with mesh refinement, and in simulating weak discontinuities once enough computing power is available.

2. The 2-D attenuation experiments showed the strong effect of the slit width, rather than the initial shock Mach number, on defining the final attenuation in both subsonic and supersonic fluid flow. For subsonic fluid flow, the experiments revealed the expected attenuation increase with the shock Mach number as an indication for the pressure ratio. Also was revealed is the existence of a minimum value for the attenuation ratio, M/M_0 , due to the choking effects on the fluid jet. At shock Mach numbers higher than the critical value of 2.068, the attenuation ratio was then found to slightly increase, which is more consistent with the analytical steady Characteristics solution than previous work.

3. Comparison between the experimental Schlieren photographs and the numerical results showed fair agreement in view of the available computing facilities. Good agreement was also noticed concerning the attenuation ratios, thus proving the cost-effectiveness of the used Finite Element Euler scheme in describing the fluid flow.

4. The results obtained by the new approximate analytical model were found to follow the trends obtained experimentally and numerically, with slightly less attenuation. This is expected since the CCW formulation, based on shock kinematics, underestimates the amount of bleeding loss caused by the diffraction process.

5. Without side bleeding, the numerical work for cylindrical converging shocks was applied to the simple case of radial shocks, which have a self-similar analytical solution deduced by Guderley [10]. The numerical results showed good agreement with Guderley's power law solution, giving a power exponent value of 0.195 compared to the closed form solution value of 0.197.

6. The comparison between plane and axisymmetric shock test cases revealed differences between the trends at high slit-chamber width ratio, which are attributed to the higher values of slit-chamber (or bled-entrapped) area ratio for cylindrical geometries. As to the attenuation effect, the numerical values for the pressure history at different radii were in good agreement with the experimental results obtained using pressure transducers.

Proposed Future Work :

1. In the field of studying shock wave dynamics in 2-D and 3-D geometries, the bulk of the work effort is still based on the two older methods (Finite Difference and Finite Volume), and their ever-growing literature provides new ideas for simulating flow discontinuities and boundary conditions. On the other hand, the advantages of the Finite Element Method present the technique as one of the promising tools for unsteady fluid flow simulation, as demonstrated in the present work. The first priority for future work should be the issue of refining the code performance, and using new schemes possessing better resolution for discontinuities.

2. To extend the work to three dimensions, matrix storage has to be considerably optimized to be able to use the available computing facilities. One way of doing this is using iterative solvers, which require storing only the matrix non-zero elements. The cost-effectiveness of the technique is expected to improve for the diagonally-dominant matrices associated with time-marching problems. The original version of the code incorporates the efficient GMRES iterative solver with the unconditionally stable implicit scheme, to allow the use of large time steps or variable size grids. The solver is uncoupled from the original formulation and can be used elsewhere. However, in case of more matrix well-posedness, other solvers may be introduced in due course, if

their performance is found to be satisfactory and their array requirements are reasonable.

3. A second possibility for extension to 3-D is using explicit time-marching schemes, where only the time derivative term forms the matrix. In addition to the advantage of reduction in matrix size, then the matrix can be formed once during the code run, with the possibility of re-scaling in case of time step change. Besides, the stability-related time step limitation should not always be considered a disadvantage since it might be inevitable for accuracy consideration. However, this will require more uniform grid size, and a considerable increase in node number and related storage. In anticipation for future developments, the numerical code incorporates a set of equations and variables chosen to ensure that the time derivative matrix is linear and solution-independent.

4. Once the computing facilities are available, the fully-deployed generic 3-D code can be used to handle the full problem of cylindrical converging shocks. The main goal is to investigate the various options for stability improvement, at a lower cost compared to experimental work. Possible options include non-uniform inner edge [69,70] or outer edge geometry for the bleed slit (to cope with observed trends of front irregularity) and multiple bleeding (to maintain the circular shape until it is as close as possible to the center).

5. Numerical and experimental facilities can be later used to tackle the more general problem of shock wave interaction in various geometries. The method presents a rich field of research for science and engineering applications (some interesting examples were mentioned in Chapter 1) thus enabling the research team to try new ideas of geometrical and physical control of shock wave perturbation and propagation.

REFERENCES :

1. Matsumora, S., Onodera, O. and Takayama, K., "Noise Induced by Weak Shock Waves in Automobile Exhaust Systems (Effects of Viscosity and Back Pressure)", *Proc. of the 19th Int. Symp. on Shock Waves and Shock Tubes*, Marseille, France (Vol. III), pp. 367-372 (1993).

2. Phan, K. C., "On the Performance of Blast Deflectors and Impulse Attenuators", *Proc. of the 18th Int. Symp. on Shock Waves and Shock Tubes*, Sendai, Japan, pp. 927-934 (1991).

3. Matsuo, K., Aoki, T., "Wave Problems in High-speed Railway Tunnels ", *Proc. of the 18th Int. Symp. on Shock Waves and Shock Tubes*, Sendai, Japan, pp. 94-102 (1991).

4. Glass, I.I., Sharma, S.P., "Production of Diamond from Graphite using Explosive-driven Implosions", *AIAA Journal*, Vol. 149 - No. 3, pp. 404-420 (1976).

5. Flagg, R.F., "The Application of Implosion Wave Dynamics to Hypervelocity Launchers", UTIAS Report no. 125 (1967).

6. Freeman, N.C., "On the Stability of Plane Shock Waves", *J. Fluid Mech.*, Vol. 2, pp. 397-411 (1957).

7. Lapworth, K.C., "An Experimental Investigation of the Stability of Plane Shock Waves", *J. Fluid Mech.*, Vol. 6, pp. 469-480 (1959).

8. Briscoe, M.G., Kovitz, A.A., "Experimental and Theoretical Study of the Stability of Plane Shock Waves Reflected Normally from Perturbed Flat Walls", *J. Fluid Mech.*, Vol. 31, pp. 529-546 (1968).

9. Van Moorhem, W.K., George, A.R. "On the Stability of Plane Shocks", *J. Fluid Mech.*, Vol. 68, pp. 97-108 (1975).

10. Guderley, G., "Powerful Spherical and Cylindrical Compression Shocks in the Neighbourhood of the Centre of the Sphere and of the Cylindrical Axis", *Luftfahrtforschung*, Vol. 19, p. 302 (1942).

11. Lighthill, M.J., *Proc. Royal Society*, 198A, p. 454 (1949).

12. Butler, D.S., "Converging Spherical and Cylindrical Shocks", *Armament Research Establishment*, Report No. 54/54, (1954).

13. Butler, D.S., "The Stability of Converging Spherical and Cylindrical Shock Waves", *Armament Research and Development Establishment*, Report No. (B) 18/56, (1956).

14. Stanyukovich, K.P., "Unsteady Motion of Continuous Media", *Gostekhizdat*, Englo. transl., Pergamon Press, New York, (1960).

15. Mishkin, E.A., Fujimoto, Y., "Analysis of a Cylindrical Imploding Shock Wave", *J. Fluid Mech.*, Vol. 89 - Part 1, pp. 61-78 (1979)

16. Glaister, P., "Similarity Solutions for Multi-component Flows", *Computers Math. Applic.*, Vol. 24 - No. 10, pp.77-88 (1992).

17. Ramu, A., Ranga Rao, M.P., "Converging Spherical and Cylindrical Shock Waves", *J. Eng. Math.*, Vol. 27, pp. 411-417 (1993).

18. Radha, Ch., Sharma, V.D., "Imploding Cylindrical Shock in a Perfectly Conducting and Radiating Gas", *Phys. Fluids* B, Vol. 5 - No. 12, pp. 4287-4294 (1993).

19. Sharma, V.D., Radha, Ch., "On One-dimensional Planar and Non-planar Shock Waves in a Relaxing Gas", *Phys. Fluids* B, Vol. 6 - No. 6, pp.2177-2190 (1994).

20. Chester, W., "The Propagation of Shock Waves in a Channel of Non-uniform Width", *Quart. J. Mech. and Appl. Math.*, Vol. VI - part 4, pp. 440-452 (1953).

21. Chisnell, R.F., "The Motion of a Shock Wave in a Channel, with Applications to Cylindrical and Spherical Shock Waves", *J. Fluid Mech.*, Vol. 4, pp.286-298 (1958).

22. Whitham, G.B., "On the Propagation of Shock Waves Through Regions of Non-uniform Area of Flow", *J. Fluid Mech.*, Vol. 4 - part 1, pp.337-360 (1958).

23. Whitham, G.B., "A New Approach to Problems of Shock Dynamics . Part I: Two-Dimensional Problems", *J. Fluid Mech.*, Vol. 2 - part 1, pp.145-171 (1957).

24. Whitham, G.B., "A New Approach to Problems of Shock Dynamics . Part II: Three-Dimensional Problems", *J. Fluid Mech.*, Vol. 5 - part 1, pp.369-386 (1959).

25. Whitham, G.B., "*Linear and Non-linear Waves*", John Wiley & sons, Interscience Publications (1974).

26. Fong, K., Ahlborn, B., "Stability of Converging Shock Waves", *Phys. Fluids*, Vol. 22 - No. 3, pp. 416-421 (1979).

27. Gardner, J.H., Book, D.L., Bernstein, I.B., "Stability of Imploding Shocks in the CCW Approximation", *J. Fluid Mech.*, Vol. 114, pp. 41-58 (1982).

28. Arad, B., Gazit, Y., Ludmirski, A., "A Sliding Discharge Device for Producing Cylindrical Shock Waves", *J. Phys. D: Appl. Physics*, Vol. 20, pp. 20-27 (1987).

29. Fujiwara, K., Hiroe, T., Matsuo, H., "New Method of Generating Cylindrical Imploding Shocks Using a Flyer Disk", *Appl. Phys. Letters*, Vol. 61 - No.26, pp. 3110-3112 (1992).

30. Fujiwara, K., Matsuo, H., Hiroe, T., "New Methods for Generating Cylindrical Imploding Shocks ", *Proc. of the 19th Int. Symp. on Shock Waves and Shock Tubes*, Marseille, France (Vol. IV), pp. 81-86 (1993).

31. Neemeh, R.A., Ostrowski, P.P., Wu, J.H.T., "Thermal Performance of a Logarithmic-Spiral Resonance Tube", *AIAA Journal*, Vol. 22 - No. 12, pp. 1823-1825 (1984).

32. Kishige, H. and Teshima, K., Nishida, M., "Focusing of Shock Waves Reflected from an Axisymmetrically Parabolic Wall", *Proc. of the 18th Int. Symp. on Shock Waves and Shock Tubes*, Sendai, Japan, pp. 340-345 (1991).

33. Inoue, O., Takahashi, N., Takayama, K., "Shock Wave Focusing in a Log-Spiral Duct", *AIAA Journal*, Vol. 31 - No. 6, pp. 1150-1152 (1993).

34. Sakamoto, I. and Higashino, F., "Focusing of Reflected Shock Waves Analyzed by Means of Geometrical Shock Dynamics", *JSME Int. Journal* - series II (Fluids), Vol. 36 - No. 4, pp. 560-566 (1993).

35. Perry, R.W. and Kantrowitz, A., "The Production and Stability of Converging Shocks", *J. Appl. Phys.*, Vol. 22 - No. 7, pp. 878-886 (1951).

36. Knystautus, R. and Lee, J.H., "Experiments on the Stability of Converging Cylindrical Detonations", *Combustion and Flames*, Vol. 16, pp.61-73 (1971).

37. Wu, J.H.T., Neemeh, R.A., Ostrowski, P.P., Elabdin, M.N., "Production of Converging Cylindrical Shock Waves by Finite Element Conical Contractions", *Proc. of the 11th Int. Symp. on Shock Tubes and Shock Waves*, Seattle, U.S.A. (1977)

38. Wu, J.H.T., Neemeh, R.A., Ostrowski, P.P., "Experimental Studies of the Production of Converging Cylindrical Shock Waves", *AIAA Journal*, Vol. 18, pp. 47-49 (1980).

39. Wu, J.H.T., Neemeh, R.A., Ostrowski, P.P., "Experiments on the Stability of Converging Cylindrical Shock Waves", *AIAA Journal*, Vol. 19 - No. 3, pp. 257-258 (1981).

40. Neemeh, R.A. and Ahmed, Z., "Stability and Collapsing of Strong and Weak Converging Cylindrical Shock Waves Subjected to External Perturbation", *Proc. of the 15th Int. Symp. on Shock Tubes and Shock Waves*, Berkley, Cal., pp. 423-439 (1985).

41. Takayama, K. Klein, H. and Groenig, H., "An Experimental Investigation of the Stability of Converging Cylindrical Shock Waves in Air", *Experiments in Fluids*, Vol.5, pp.315-322 (1987).

42. Watanabe, M. and Takayama, K., "Stability of Converging Cylindrical Shock Waves", *Shock Waves*, Vol. 1, pp.149-160 (1991).

43. Payne, R.B., "A Numerical Method for a Converging Cylindrical Shock", *J. Fluid Mech.*, Vol. 2, pp.185-200 (1957).

44. Sod, G.A., "A Numerical Study of a Converging Cylindrical Shock", *J. Fluid Mech.*, Vol. 83 - part 4, pp.785-794 (1977).

45. Munz, C.D., "Two-step Schemes for the Euler Equations and Numerical Experiments on the Stability of Converging Cylindrical Shock Wave", *Proc. of the 16th Int. Symp. on Shock Waves and Shock Tubes*, Aachen, Germany, pp.685-691 (1987).

46. Shankar, R and Singh, T.V., "on Converging Cylindrical Shock in Radiation Gas Dynamics - Numerical Study", *J. Phys. Soc. of Japan*, Vol. 16 - No. 9, pp. 3146-3152 (1992).

47. Glaister, P., "Real Gas Flows in a Duct", *Computers Math. Applic.*, Vol. 24 - No. 11, pp.45-59 (1992).

48. Demmig, F., Hehmsoth, H.-H., "Model Computation of Converging Cylindrical Shock Waves: Initial Configurations, Probagation and reflection", *Proc. of the 17th Int. Symp. on Shock Waves and Shock Tubes*, Bethlehem, Pa., pp. 155-160 (1989).

49. Oran, E.S. and DeVore, C.R., Boris, J.P., "Theory and Simulations of Imploding Detonations", *Proc. of the 18th Int. Symp. on Shock Waves and Shock Tubes*, Sendai, Japan, pp. 1091-1098 (1991).

50. Watanabe, M. and Takayama, K., "Stability of Converging Cylindrical Shock Waves", *JSME Int. Journal* series II (Fluids), Vol. 35 - No. 2, pp.218-227 (1992).

51. Oran, E.S. and DeVore, C.R., "The Stability of Imploding Detonations: Results of Numerical Simulations", *Phys. Fluids*, Vol. 6 - No. 1, pp. 369-380 (1994).

52. Demmig, F. et al., "Experiments and Model Computation of Cylindrical Shock Waves with Time-resolved Deformation and Fragmentation", *Shock Waves* (1994).

53. Igra, O., Ben-dor, G., Aizik, F. and Gelfand, B., "Experimental and Numerical Investigation of Shock Wave Attenuation in Dust-Gas Suspensions", *Proc. of the 19th*

Int. Symp. on Shock Waves and Shock Tubes, Marseille, France (Vol. III), pp. 49-54 (1993).

54. Rudinger, G., "*Wave Diagrams for Nonsteady Flow in Ducts*", D. Van Nostrad Co., Inc. (1955)

55. Rosciszewski, J, "Calculations of the Motion of Non-uniform Shock Waves", *J. Fluid Mech.*, Vol. 8, pp. 337-367 (1961).

56. Szumowski, A.P., "Motion of a Shock Wave Along a Perforated Tube", *Proc. of the 8th Int. Symp. on Shock Waves and Shock Tubes*, Imperial College, London, U.K., p. 14/1 (1971).

57. Wu, J.H.T., Ostrowski, P.P., "Shock Attenuation in a Perforated Duct", *Proc. of the 8th Int. Symp. on Shock Waves and Shock Tubes*, Imperial College, London, U.K., pp. 15/1-14 (1971).

58. Merzkirch, W., Erdmann, W., "Measurement and Calculation of Shock Attenuation in a Channel With Perforated Walls", *Proc. of the 13th Int. Symp. on Shock Waves and Shock Tubes*, Niagra Falls, pp. 185-190 (1981).

59. Frolov, S.M., Gelfand, B.E., "Shock Wave Attenuation in Channels With Perforated Walls", *Proc. of the 18th Int. Symp. on Shock Waves and Shock Tubes*, Sendai, Japan, pp. 197-202 (1991).

60. Frolov, S.M., "Effectiveness of Attenuating Shock Waves in Channels With Various Mehods", *J. Appl. Mech. & Tech. Phys.*, pp. 31-36 (1994).

61. Skews, B.W., "The Shape of a Diffracting Shock Wave", *J. Fluid Mech.*, Vol. 29 (1967).

62. Skews, B.W., " Shock Diffraction on Rounded Corners", *Third Australian Conf. on Hydraulics & fluid Mech.*, The Institution of Engineers, Australia (1968).

63. Wu, J.H.T., Ostrowski, P.P., "Shock Interaction with a Narrow Slit", *C.A.S.I. Transact.*, Vol. 5 - No. 1, pp. 38-41 (1972).

64. Ostrowski, P.P., "*Attenuation of a Shock Wave By a Single Transverse Slit*", Ph.D. Thesis, McGill University (1975)

65. Lee, J.H.S., Ostrowski, P.P., Wu, J.H.T., "Shock Attenuation by a Single Transverse Slit", *J. Fluid Mech.*, Vol. 76 - part 4, pp. 675-688 (1976).

66. Wu, J.H.T., Yu, T.S.H., Neemeh, R.A., Ostrowski, P.P., "Stability of Cylindrical Converging Shock Perturbed by a Bleed Aperture", *Proc. of the 12th Int. Symp. on Shock Tubes and Shock Waves*, Jerusalem, Israel (1979).

67. Neemeh, R.A., "The Propagation and Stability of Converging Cylindrical Shock Waves in Narrow Cylindrical Chambers", *Proc. of the 18th Int. Symp. on Shock Waves and Shock Tubes*, Sendai, Japan, pp. 273-278 (1991).

68. Amirfazli, A., "*Numerical Simulation of Imploding Shock Waves*", M.Sc. Thesis, Concordia University (1994).

69. Tashtoush, B. M., "*The Effect of Non-uniform Bleed and Cylindrical Chamber Width on Converging Cylindrical Shock Wave Stability*", Ph.D. Thesis, Concordia University (1994).

70. Neemeh, R.A., Tashtoush, B.M., Vatistas, G.H., "The Relationship Between the Size of the Perturbation and the Vortex Pairs Structure for Converging Cylindrical

Shocks", *Proc. of the 19th Int. Symp. on Shock Waves and Shock Tubes*, Marseille, France, (Vol. IV), pp. 75-80 (1993).

71. Wendt, J.F. (ed.), "*Computational Fluid Dynamics: an Introduction*", Von Karman Institute publications, Springer Verlag (1992).

72. Book, D.L., Lohner, R., "Simulation and Theory of the Quatrefoil Instability of a Converging Cylindrical Shock", *Proc. of the 17th Int. Symp. on Shock Waves and Shock Tubes*, Bethlehem, Pa., pp. 149-153 (1989).

73. Sivier, S., Baum, J.D., Loth, E., Lohner, R., "Vorticity Produced by Shock Wave Diffraction", *Proc. of the 18th Int. Symp. on Shock Waves and Shock Tubes*, Sendai, Japan, pp. 143-150 (1991).

74. Luo, H., Baum, J.D., Lohner, R., "A Comparison Study of Two Finite Element Schemes for Computation of Shock Waves", *Proc. of the 19th Int. Symp. on Shock Waves and Shock Tubes*, Marseille, France, (Vol. I), pp. 401-406 (1993).

75. Baruzzi, G., "*Finite Element Solutions of the Euler Equations in Primitive Variables Form*", M.Sc. Thesis, Concordia University (1989)

76. Baruzzi, G., Habashi, W.G., Hafez, M.M., "Finite Element Solutions of the Euler Equations for Transonic External Flows", *AIAA Journal*, Vol. 29 - No. 11, pp. 1886-1893 (1991).

77. Saad, Y., Schultz, M.H., "GMRES: a Generalized Minimal RESidual Algorithm for Solving Nonsymmetric Linear Systems", *SIAM. J. Sci. Stat. Comput.*, Vol. 7 - No. 3, p. 856-869 (1986).

78. Strigberger, J., Baruzzi, G., Habashi, W.G., Fortin, M., "Some Special Purpose Preconditioners for Conjugate Gradient-like Methods Applied to CFD", *Int. J. Num. Meth. Fluids*, Vol. 16 - No. 7, pp. 581-596 (1993).

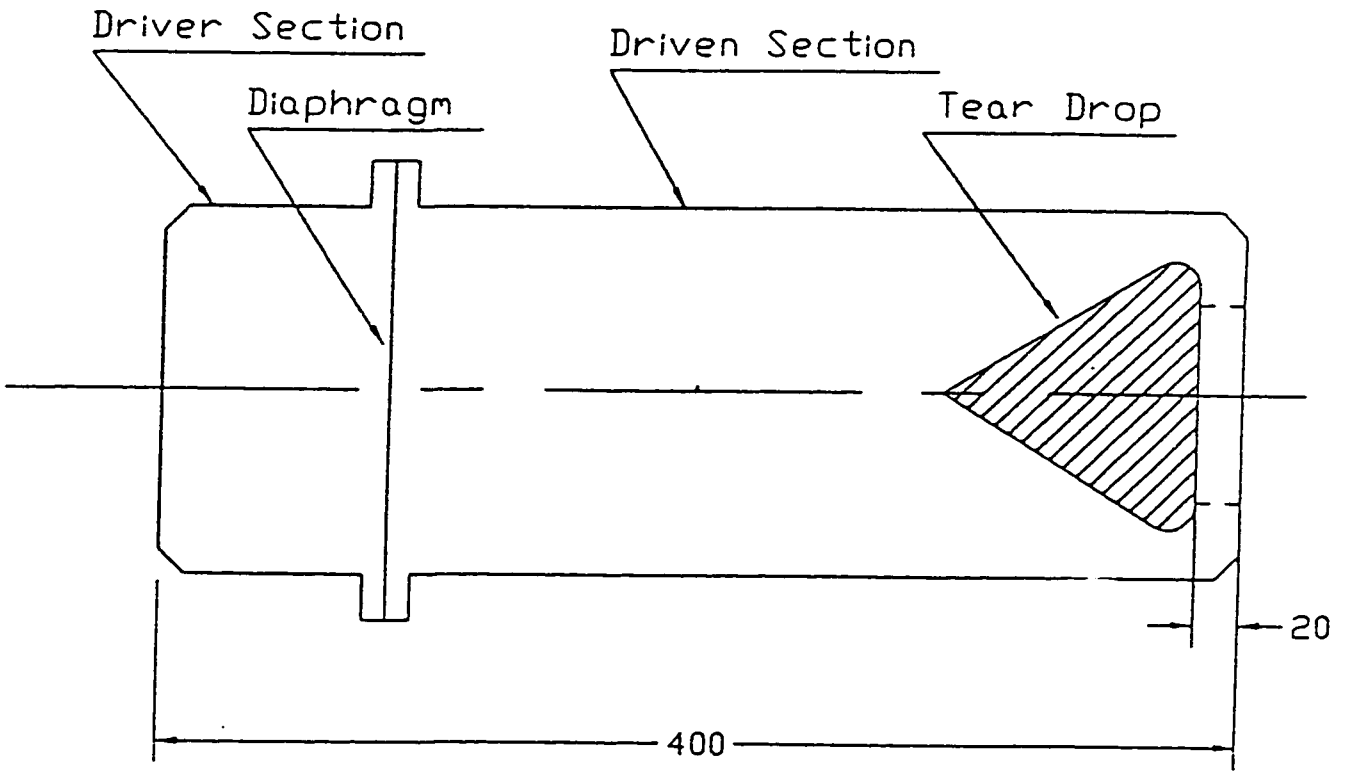

Fig.(1.1) Perry and Kantrowitz shock tube.

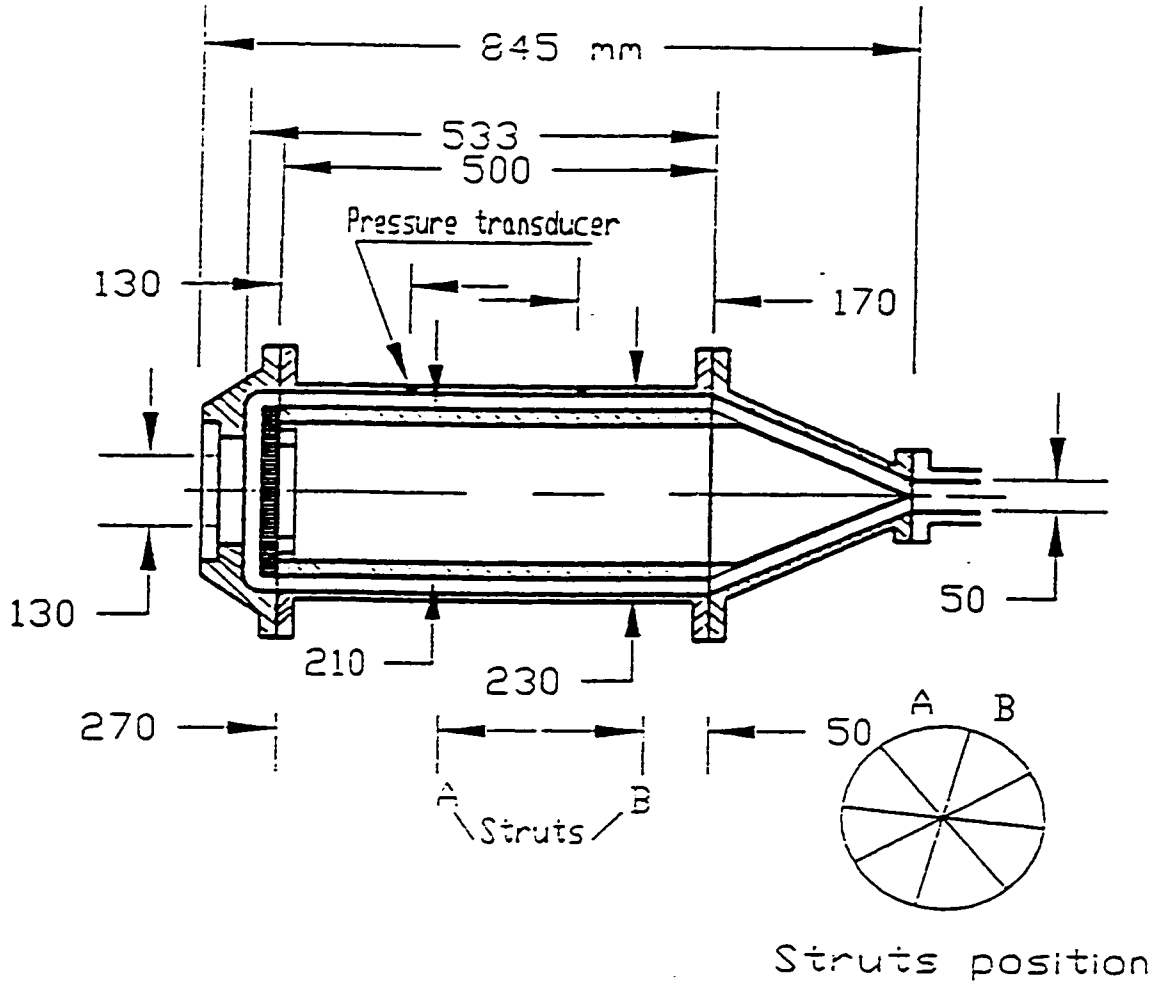

Fig.(1.2) Takayama and Watanabe shock tube.

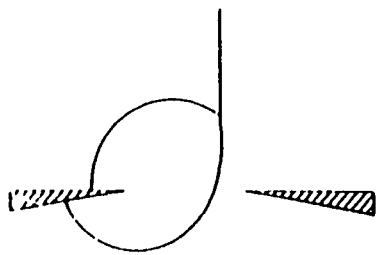

a. Diffraction

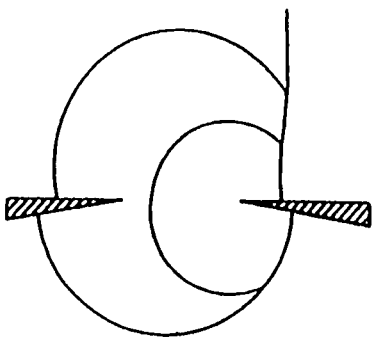

b. Diffraction and
Mach Reflection

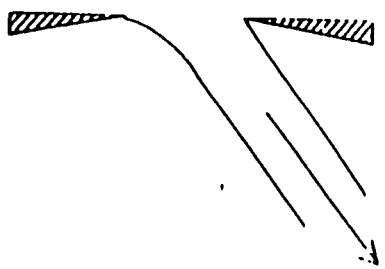

c. Steady -state
Configuration

Fig.(1.3) Shock-slit interaction (subsonic duct flow).

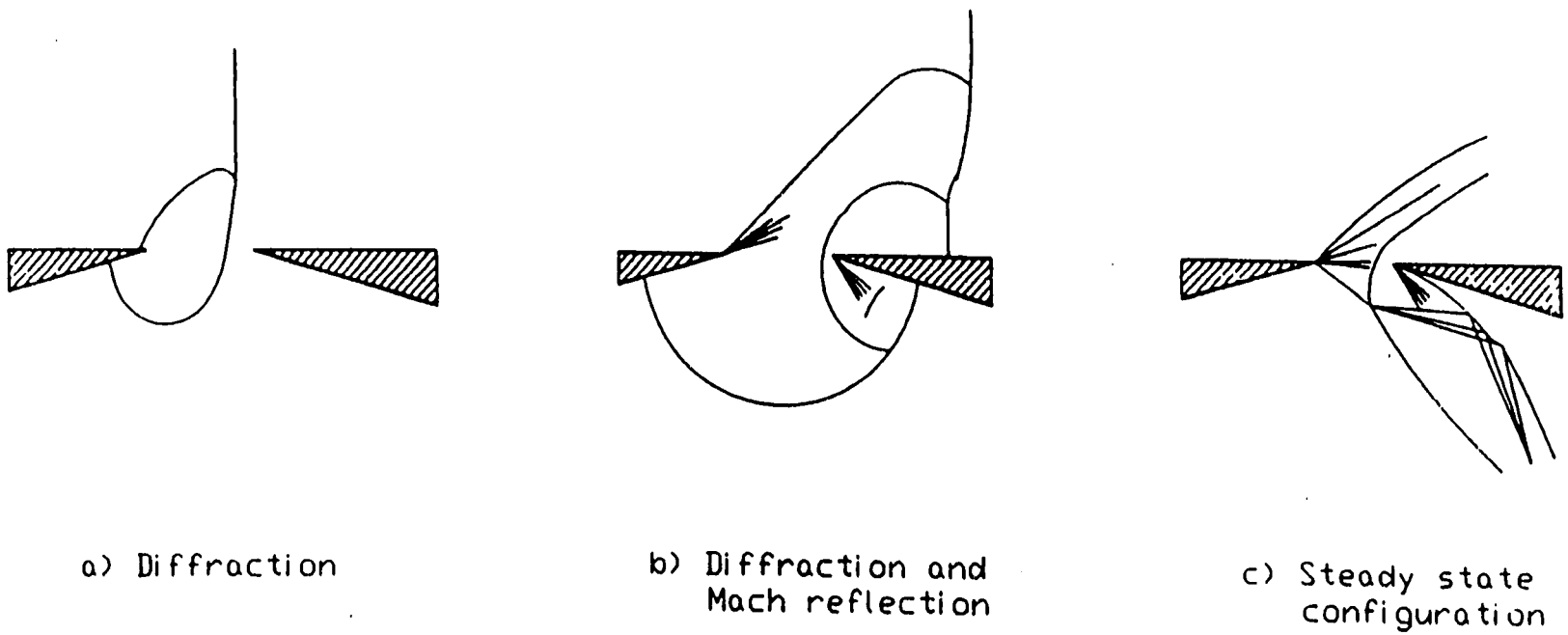

Fig.(1.4) Shock-slit interaction (supersonic duct flow).

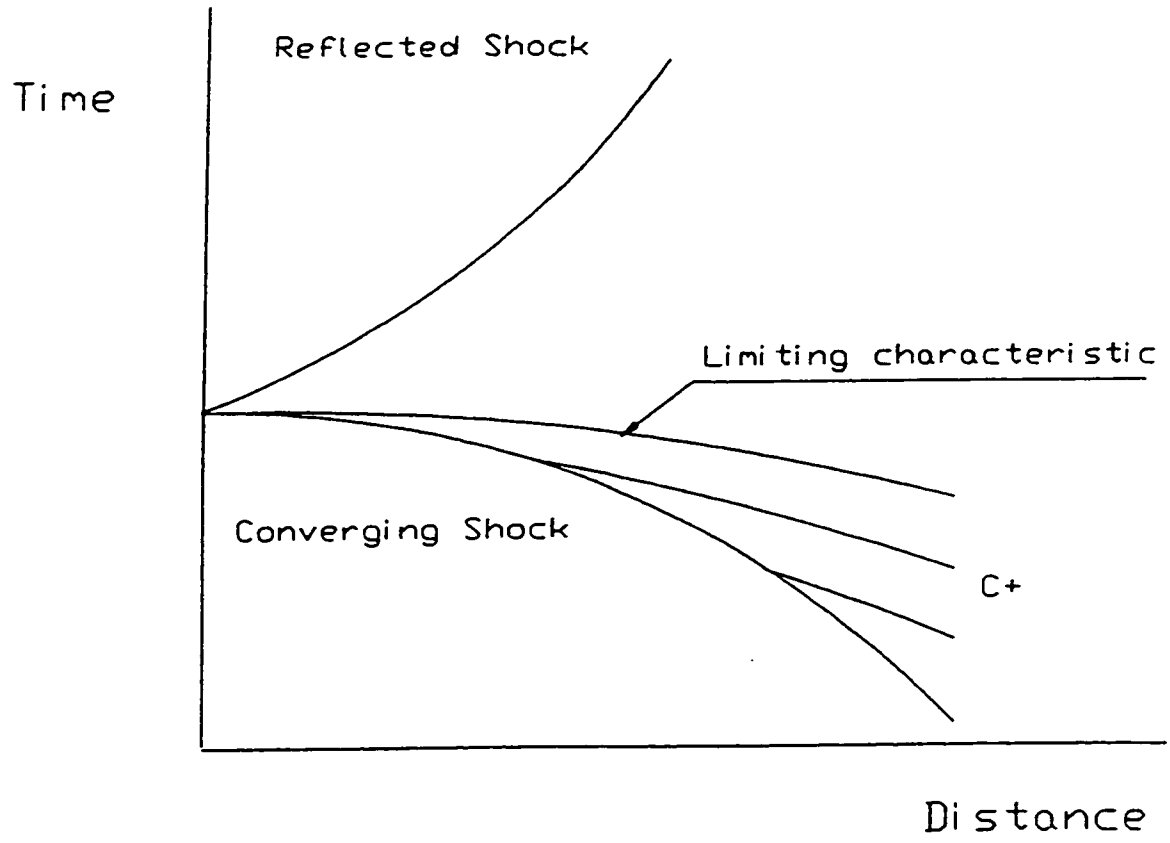

Fig.(2.1) The (x , t) diagram for Guderley's implosion solution.

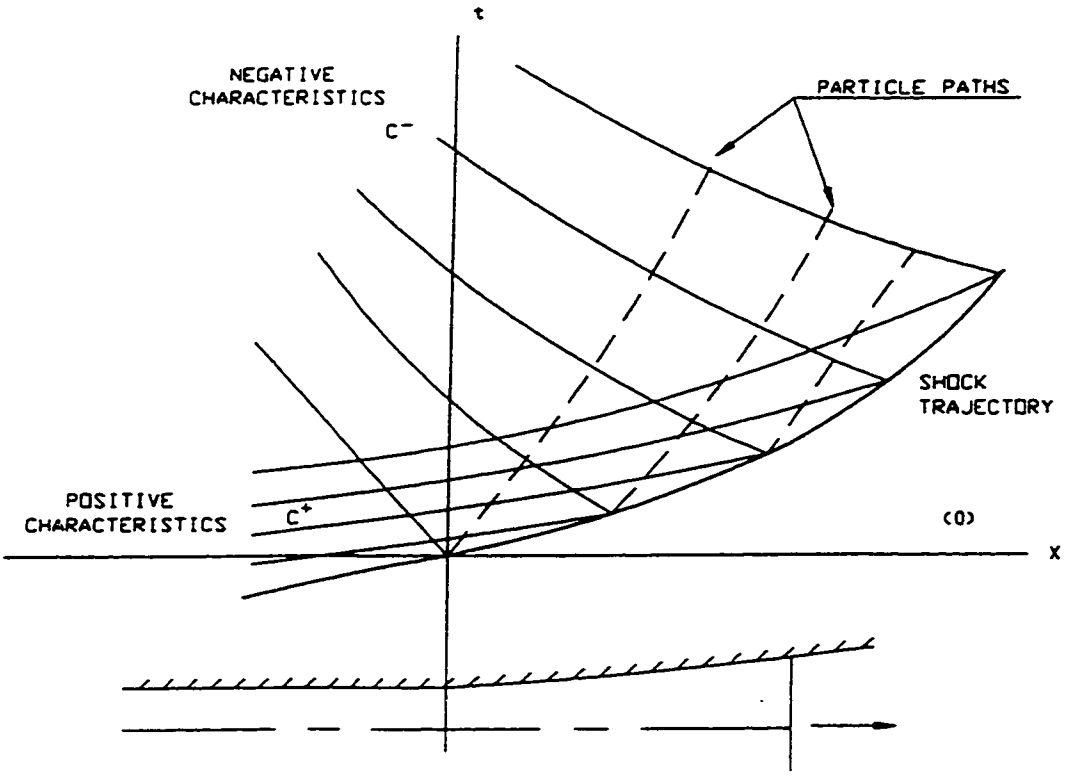

Fig.(2.2) The (x , t) diagram for shock propagation in a non-uniform area duct (subsonic flow behind the shock).

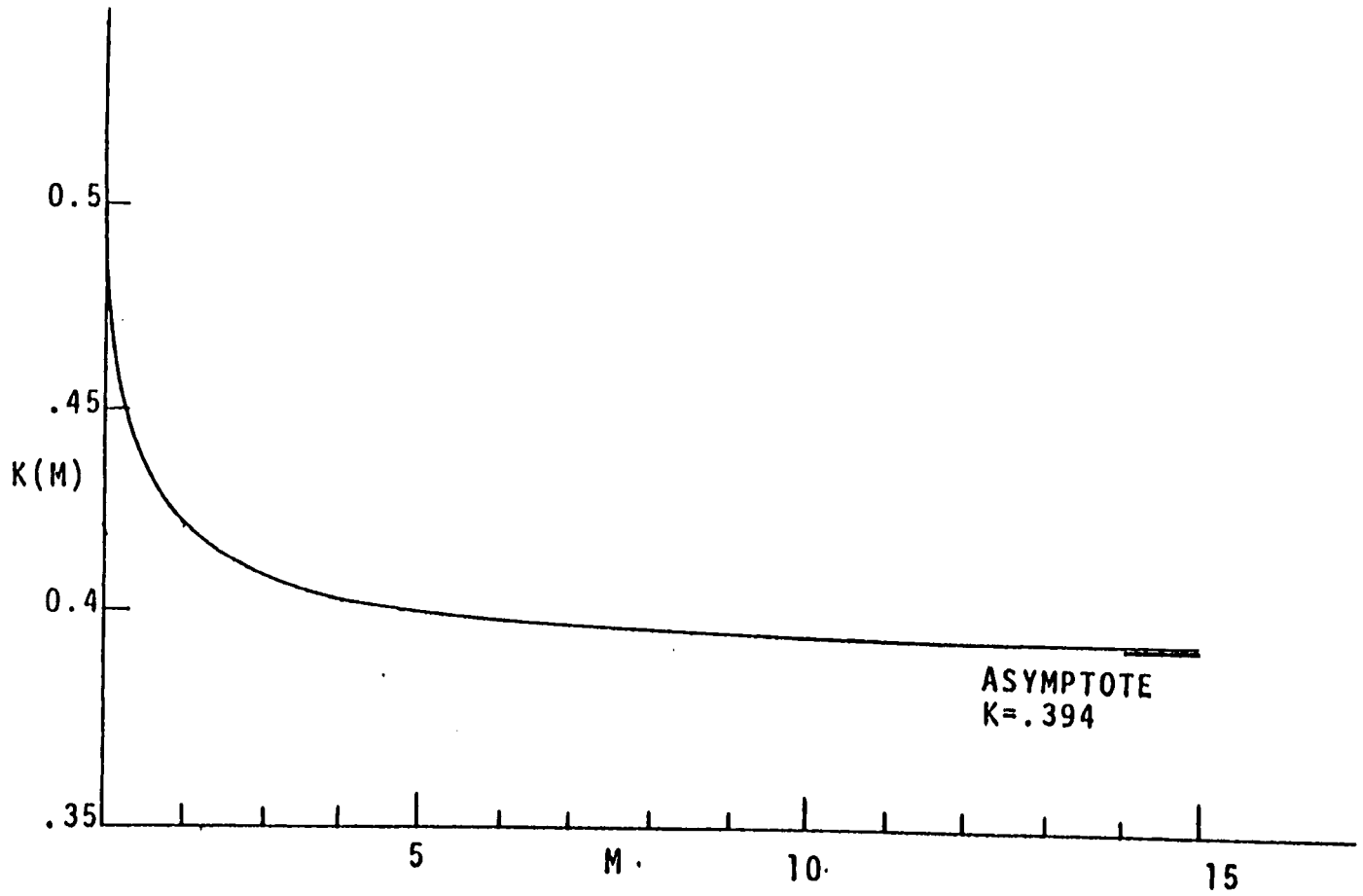

Fig.(2.3) The Chester function [ref. 64].

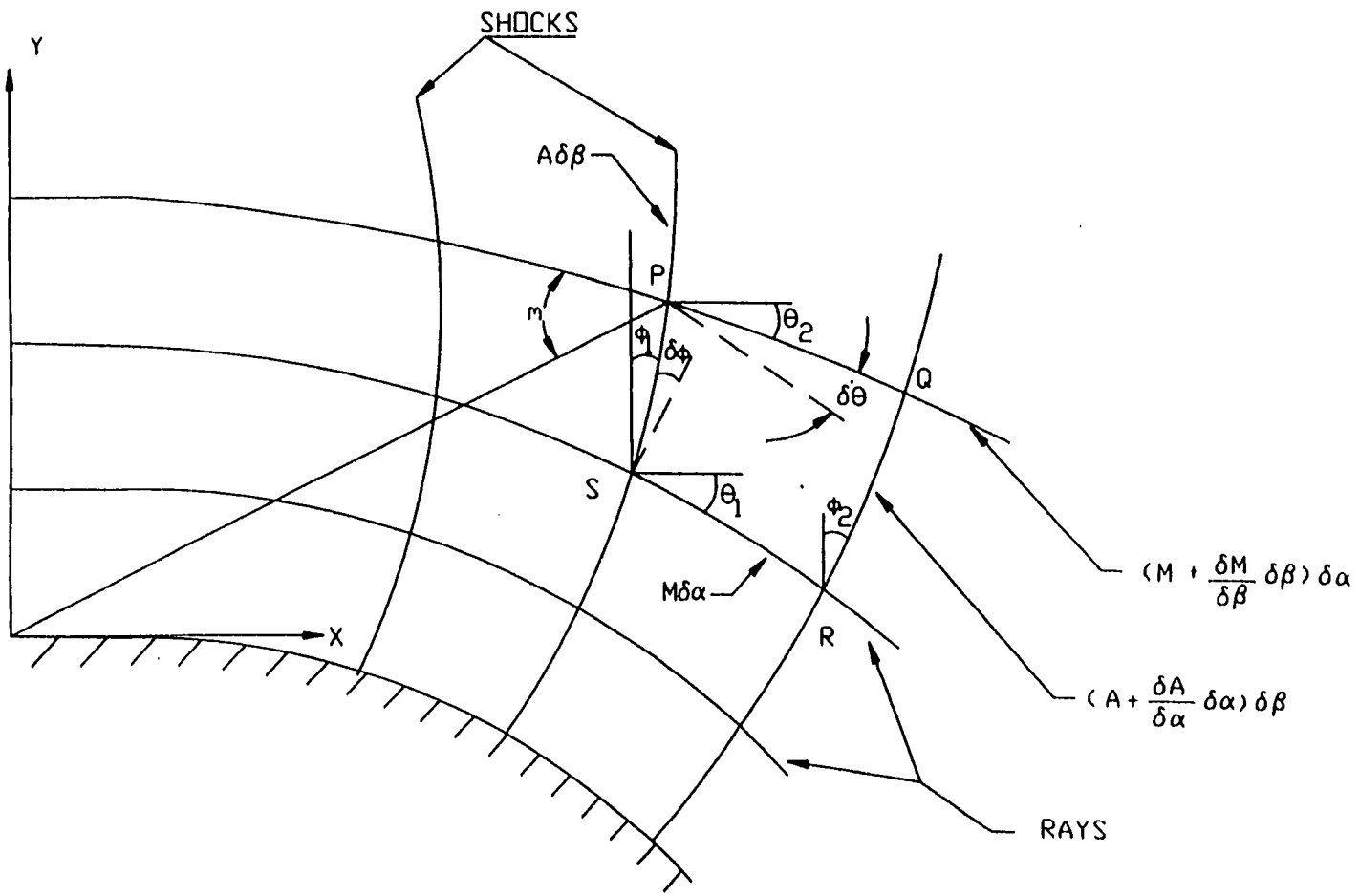

Fig.(2.4) Curvilinear quadrilateral element.

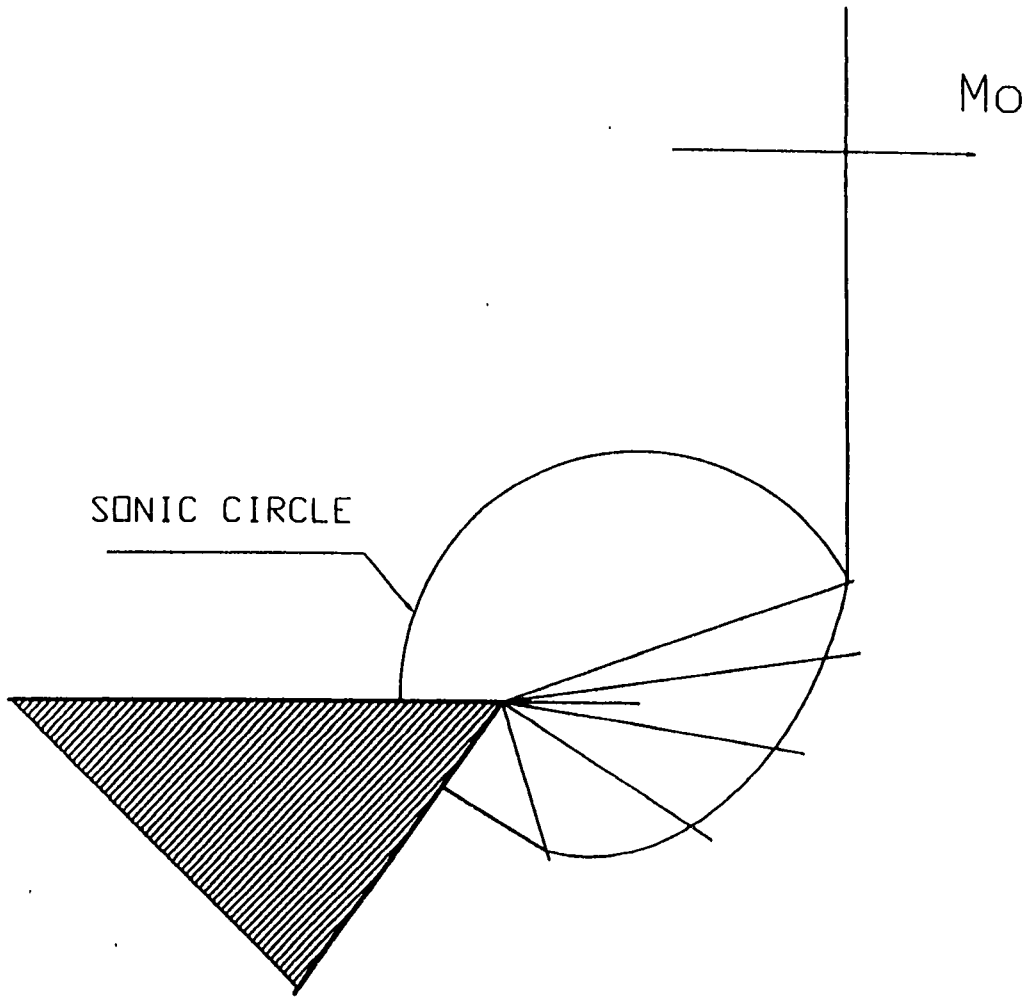

Fig.(2.5) Shock diffraction at a convex corner
(subsonic flow behind the incident shock).

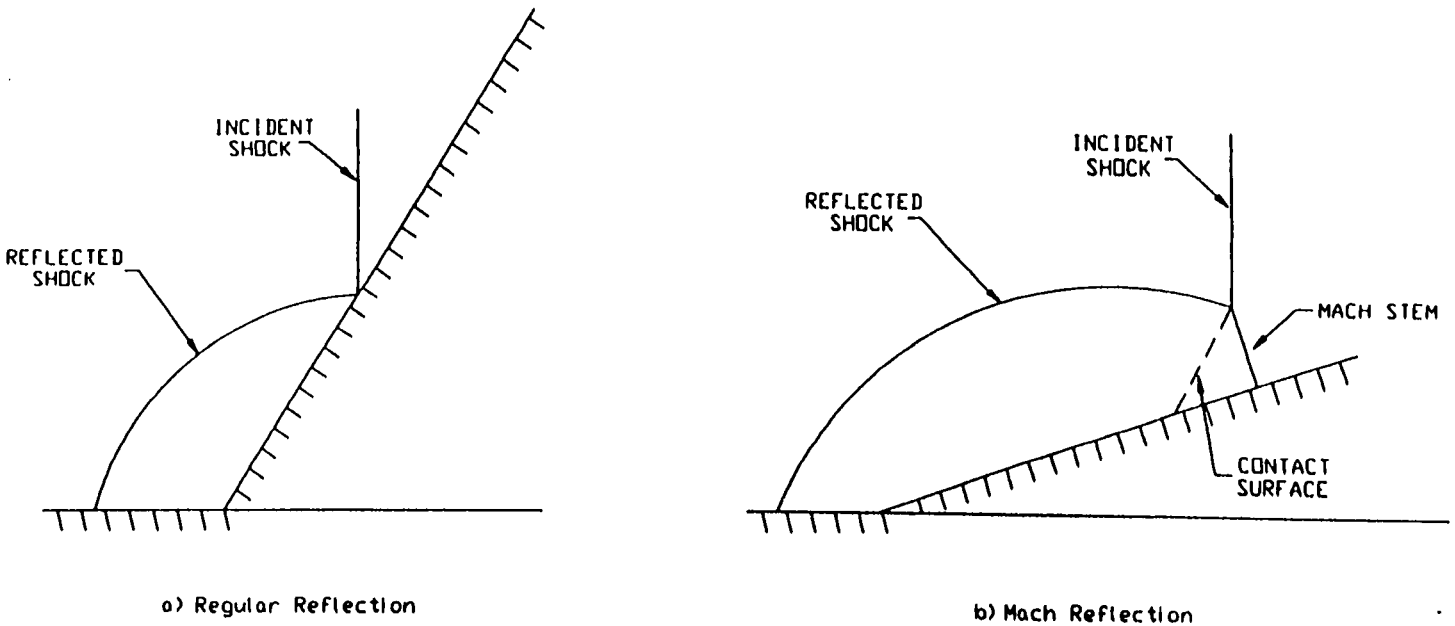

Fig.(2.6) Reflection of a moving shock wave.

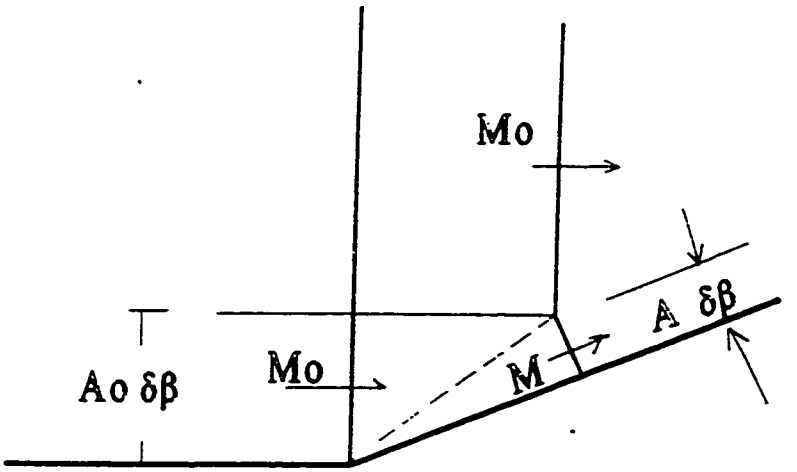

Fig.(2.7) Ray-shock treatment of Mach reflection.

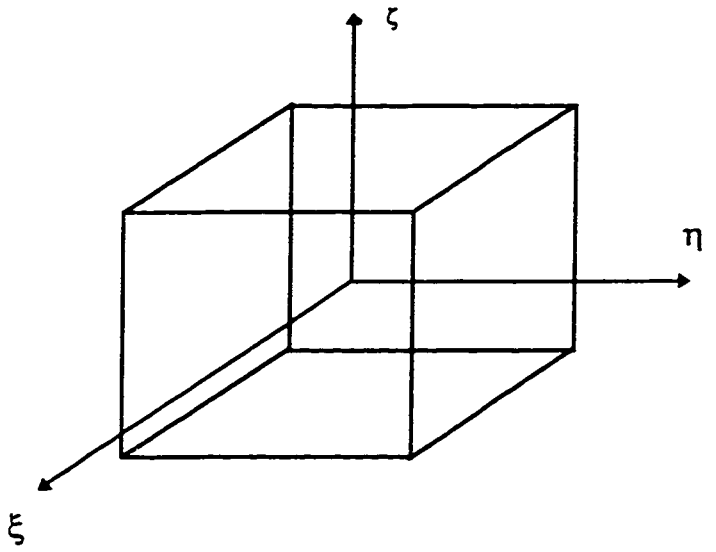

a) Natural co-ordinate space

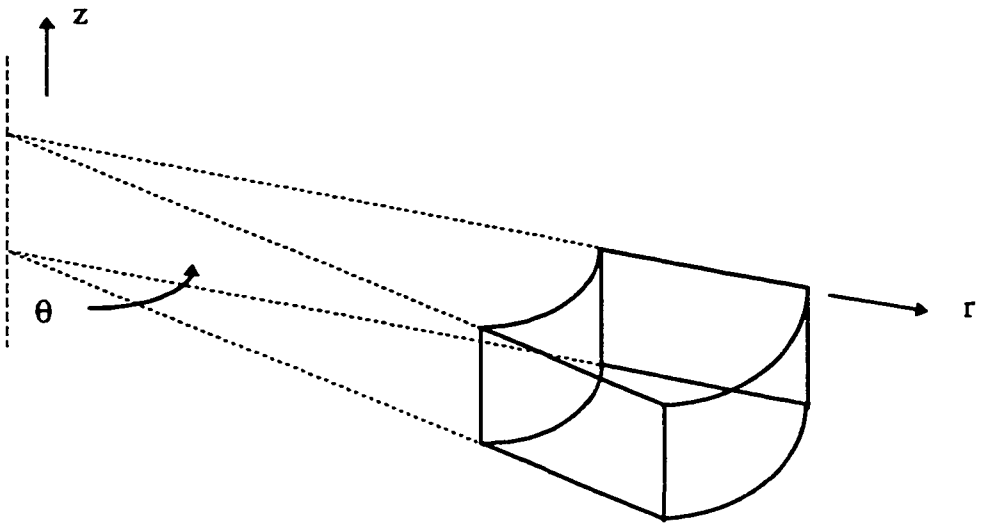

b) Physical co-ordinate space

Fig.(3.1) Finite Element geometry.

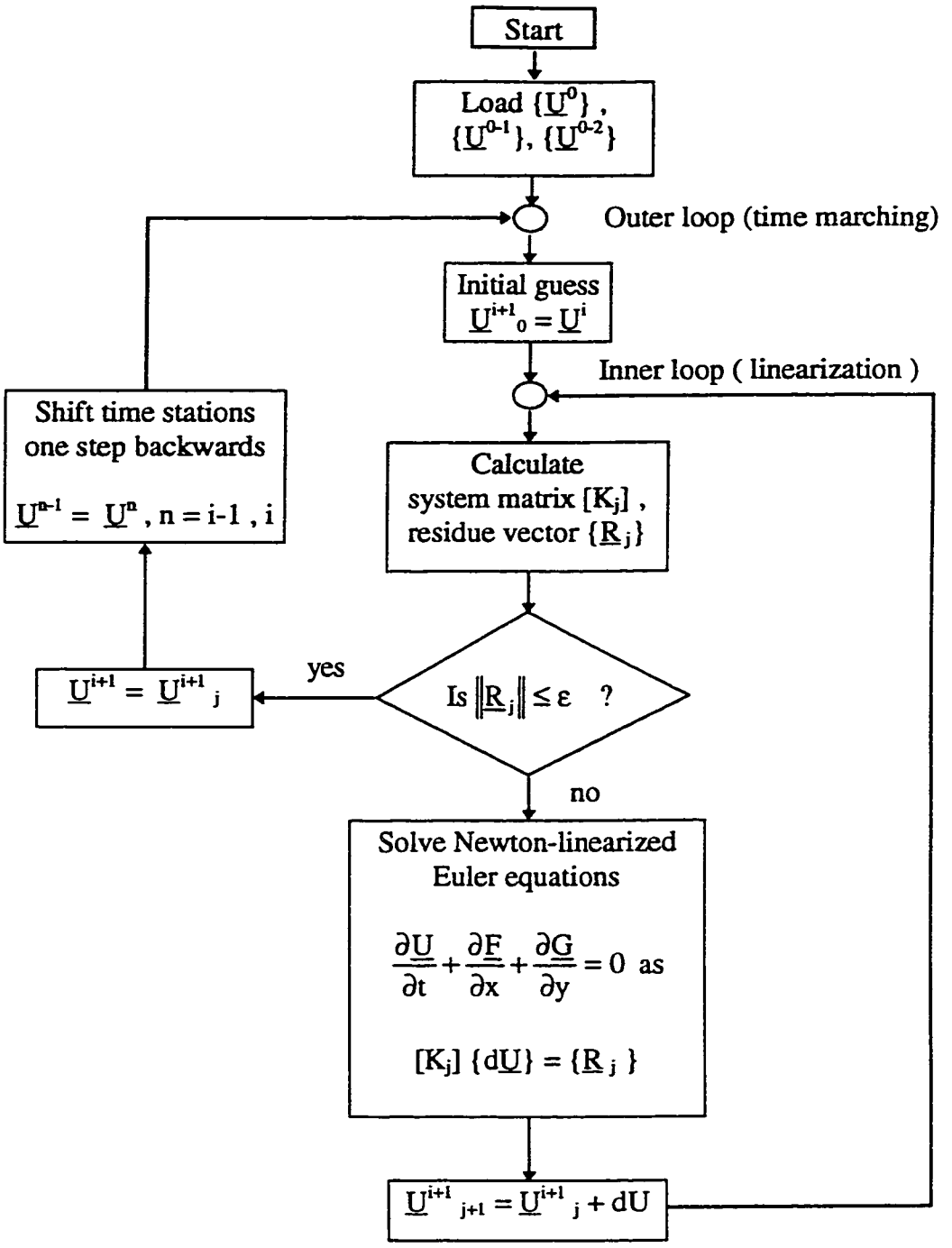

Fig.(3.2) Flow chart for the numerical solution.

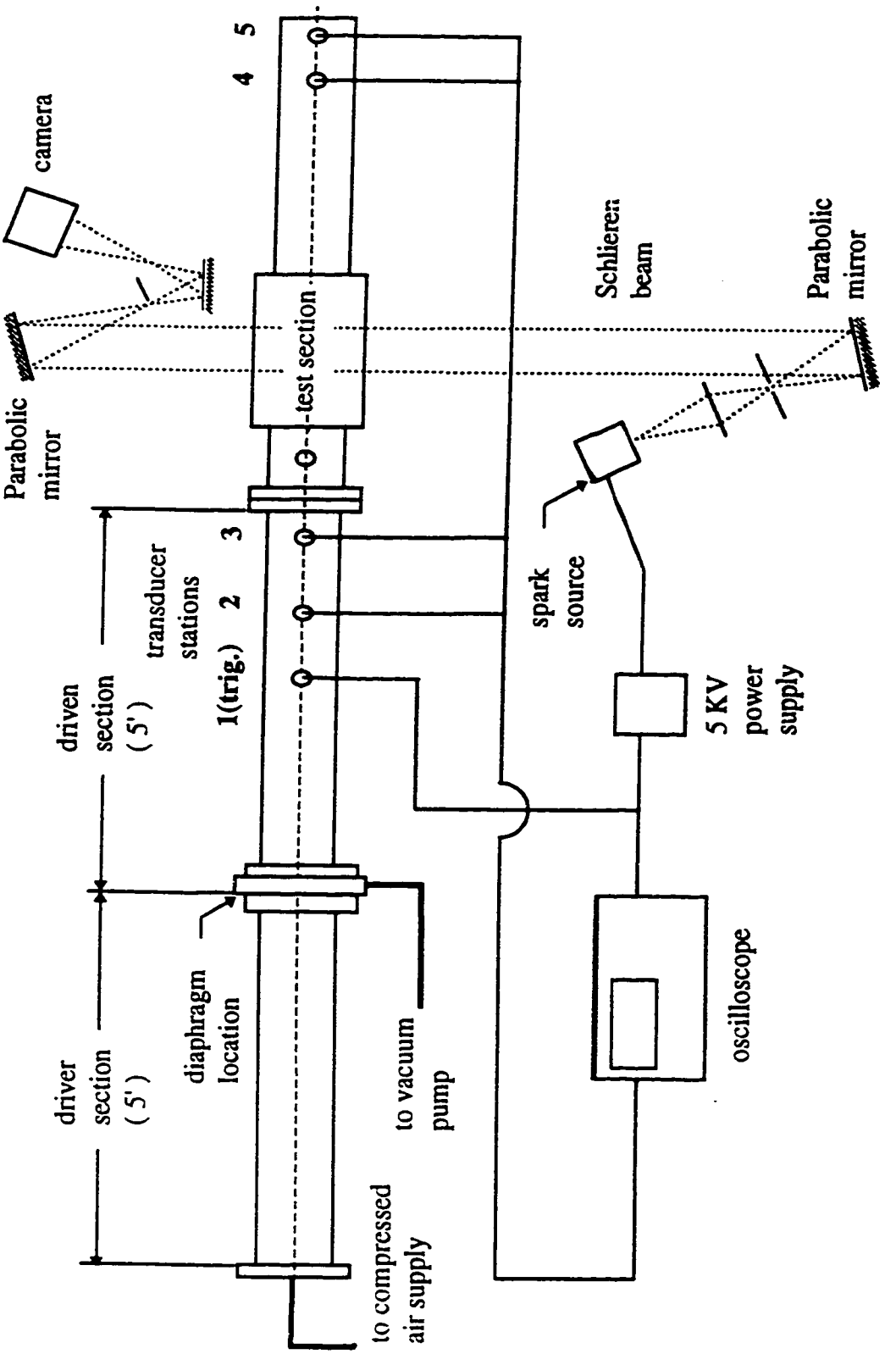

Fig.(4.1) 2-D shock tube experimental setup

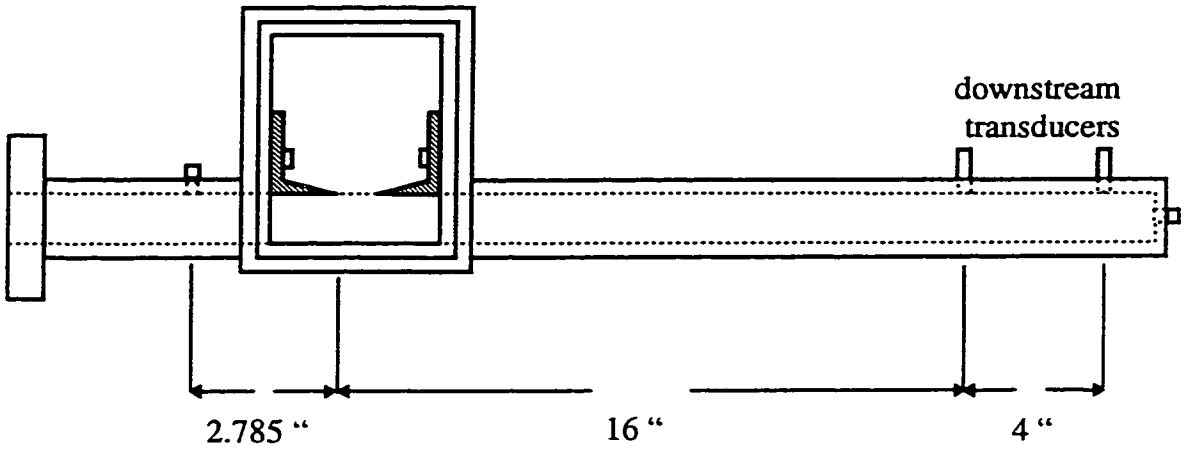

a) Shock-slit interaction experiment.

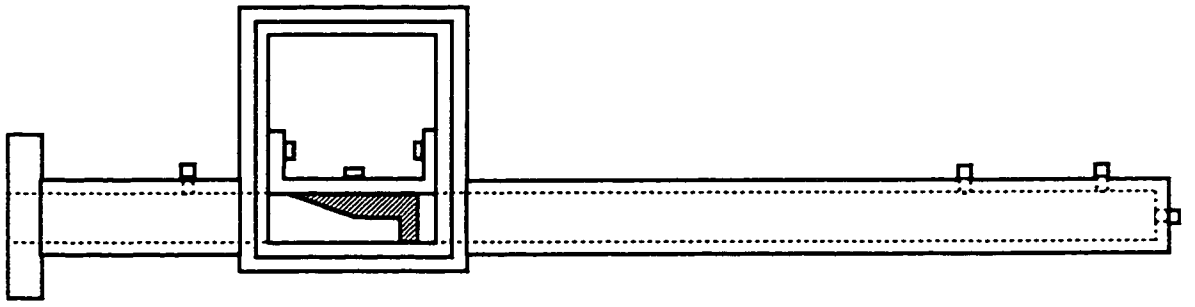

b) Shock strengthening 15° ramp experiment.

Fig.(4.2) Test sections used in the 2-D square shock tube.

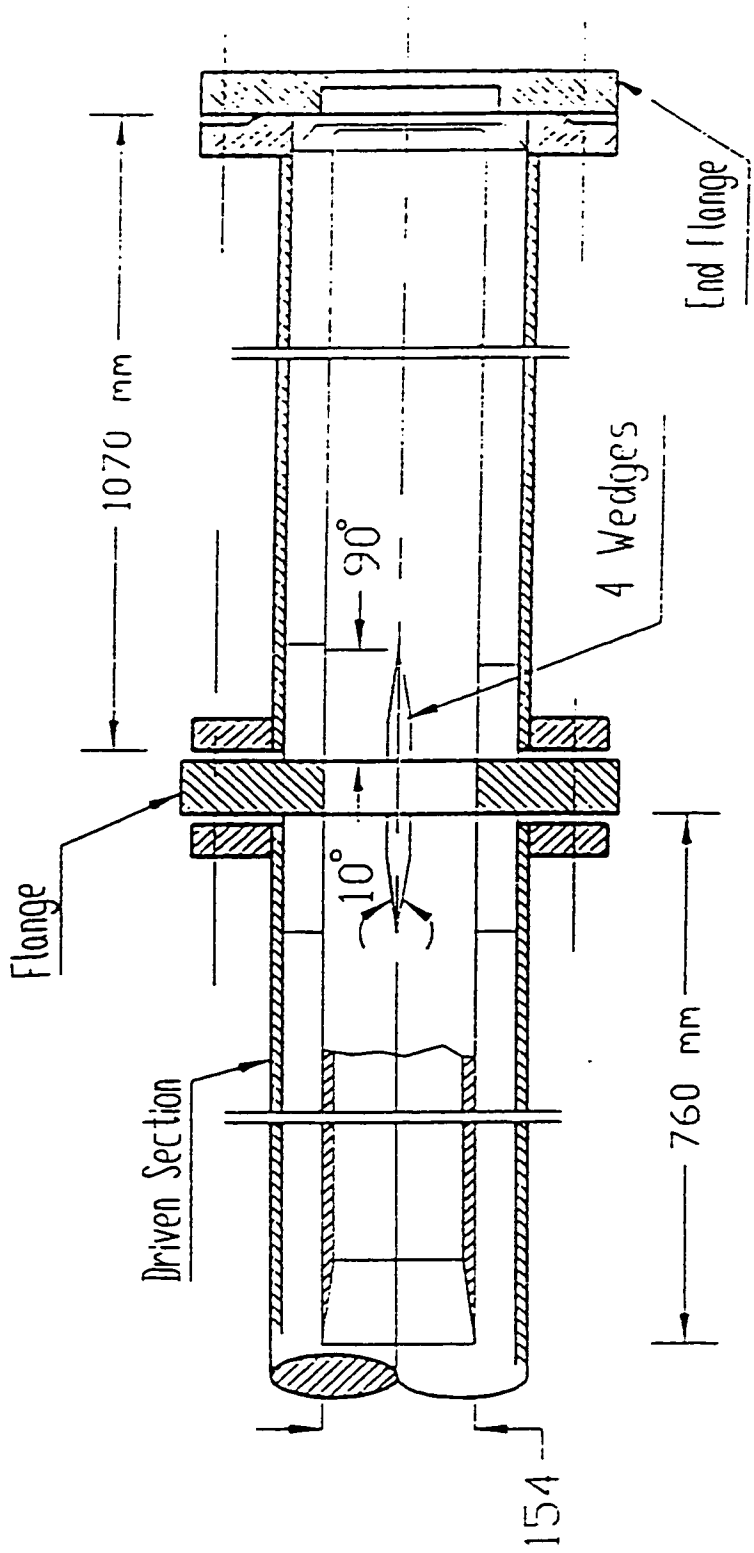

Fig.(4.3) Test section for the cylindrical shock tube.

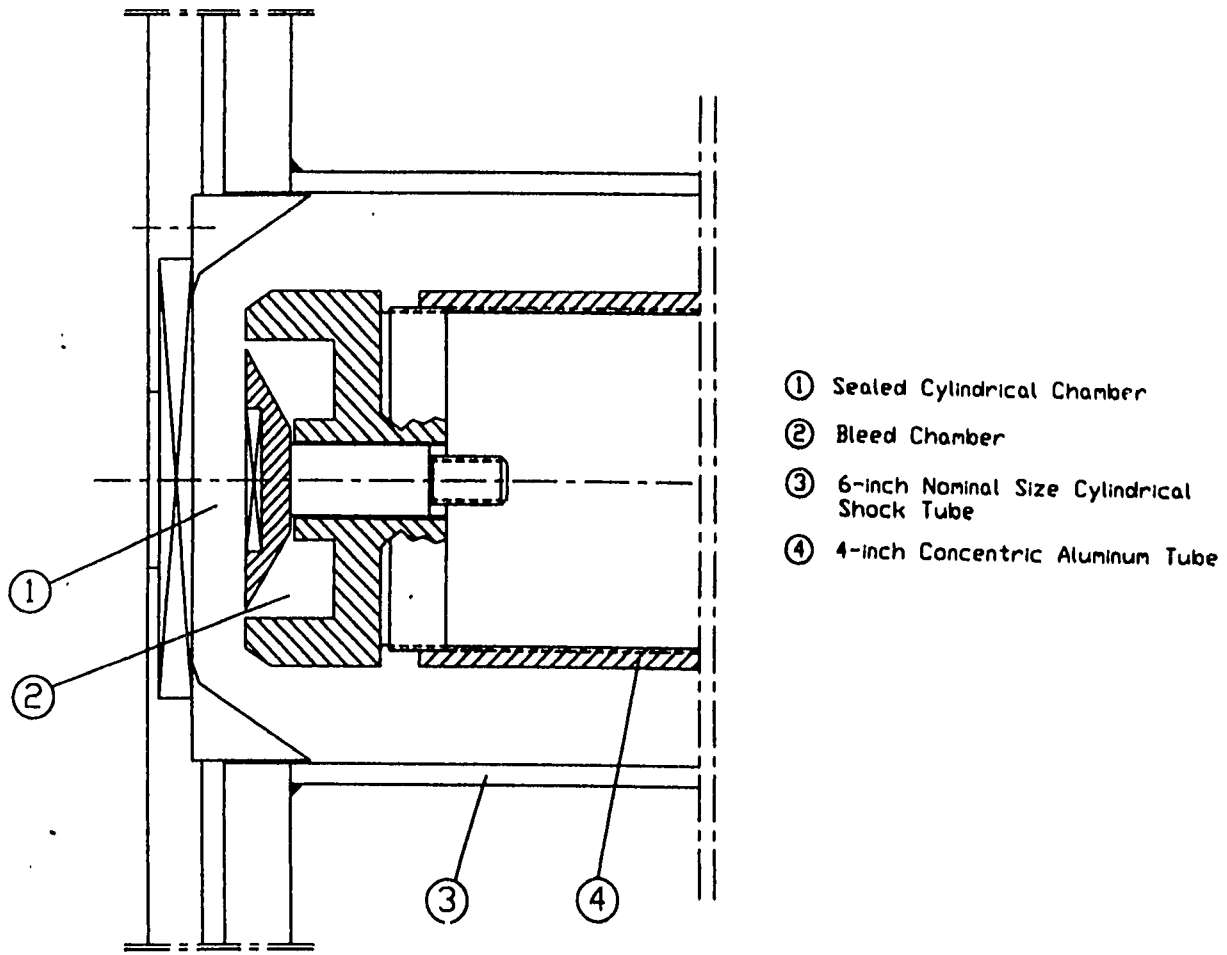

Fig.(4.4) The new test section.

QUARTZ, LOW-IMPEDANCE, VOLTAGE-MODE

SUBMINIATURE PRESSURE TRANSDUCER

with built-in amplifier Series 105A

PCB PIEZOTRONICS

PRESSURE

- flush, flat diaphragm; only 0.1 inch diameter
- small frontal area, requires little mounting space
- choice of three installation configurations
- rigid quartz element
- built-in unity-gain amplifier enhances resolution
- high level, low-impedance output signal

For shock wave, blast, explosion, combustion, compression, actuation, pulsation, cavitation, ultrasonic, aerodynamic, hydraulic, fluidic, acoustic and turbulence pressure measurements in applications with very restricted mounting space or where frontal area is critical.

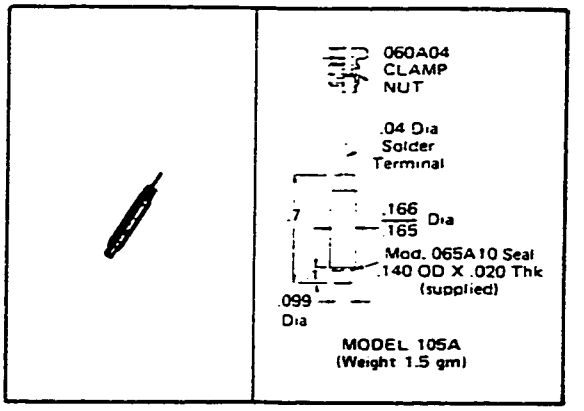

MODEL 105A
(Weight 1.5 gm)

SPECIFICATIONS	MODEL NO. MODEL NO. MODEL NO.	105A 105A02 105A03	105A12 105A13	105A22 105A23	105A33	105A43
Full Scale Range	psi	100	1000	5000	10000	30000
Maximum Pressure	psi	200	2000	7500	15000	40000
Resolution (200 μV p-p Noise)	psi	.01	0.1	0.2	0.4	1.0
Sensitivity	mV/psi	20[1]	5	1	0.5	0.2
Resonant Frequency	KHz	250	250	250	250	250
Rise Time	μsec	2	2	2	2	2
Discharge Time Constant	sec	1	1	1	10	100
Low-Frequency (−5%)	Hz	0.5	0.5	0.5	0.05	0.005
Linearity B.S.L.	% F.S.	2	2	2	2	2
Output Voltage, F.S.	volts	2	5	5	5	6
Output Impedance	ohms	100	100	100	100	100
Acceleration Sensitivity	psi/g	0.003	0.003	0.003	0.003	0.003
Temperature Coefficient	%/°F	0.03	0.03	0.03	0.03	0.03
Temperature Range	°F	−100 +250	−100 +250	−100 +250	−100 +250	−100 +250
Flash Temperature	°F	3000	3000	3000	3000	3000
Vibration/Shock	g pk	1000/5000	1000/5000	1000/5000	1000/5000	1000/5000
Material	S.S.	17-4PH	17-4PH	17-4PH	17-4PH	17-4PH
Power Req'd (thru CC Diode)	+VDC/mA	+18-24/2-20	+18-24/2-20	+18-24/2-20	+18-24/2-20	+18-24/2-20

Note [1] 10mV/psi for Model 105A03

Series 105A universal quartz sub-minigages measure slow and fast dynamic pressures from full vacuum to 30,000 psi, relative to the initial or average pressure level. The structure of this tiny instrument contains two quartz disks operating in a thickness-compression mode. An internal microelectronic, unity-gain amplifier generates a high-level low-impedance analog output signal proportional to the measurand when the transducer is connected with a coaxial or 2-wire cable to a pcb power unit. Three external configurations offer a variety of mounting possibilities. Contoured conformal tips are also possible.

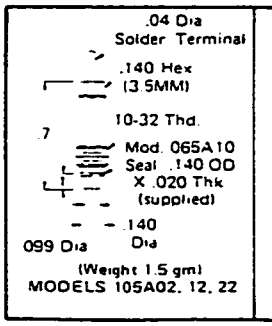

(Weight 1.5 gm)
MODELS 105A02, 12, 22

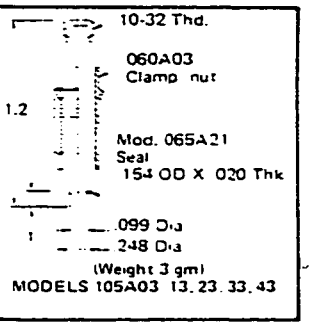

(Weight 3 gm)
MODELS 105A03, 13, 23, 33, 43

19

Fig.(4.5) Specifications for the pressure transducers.

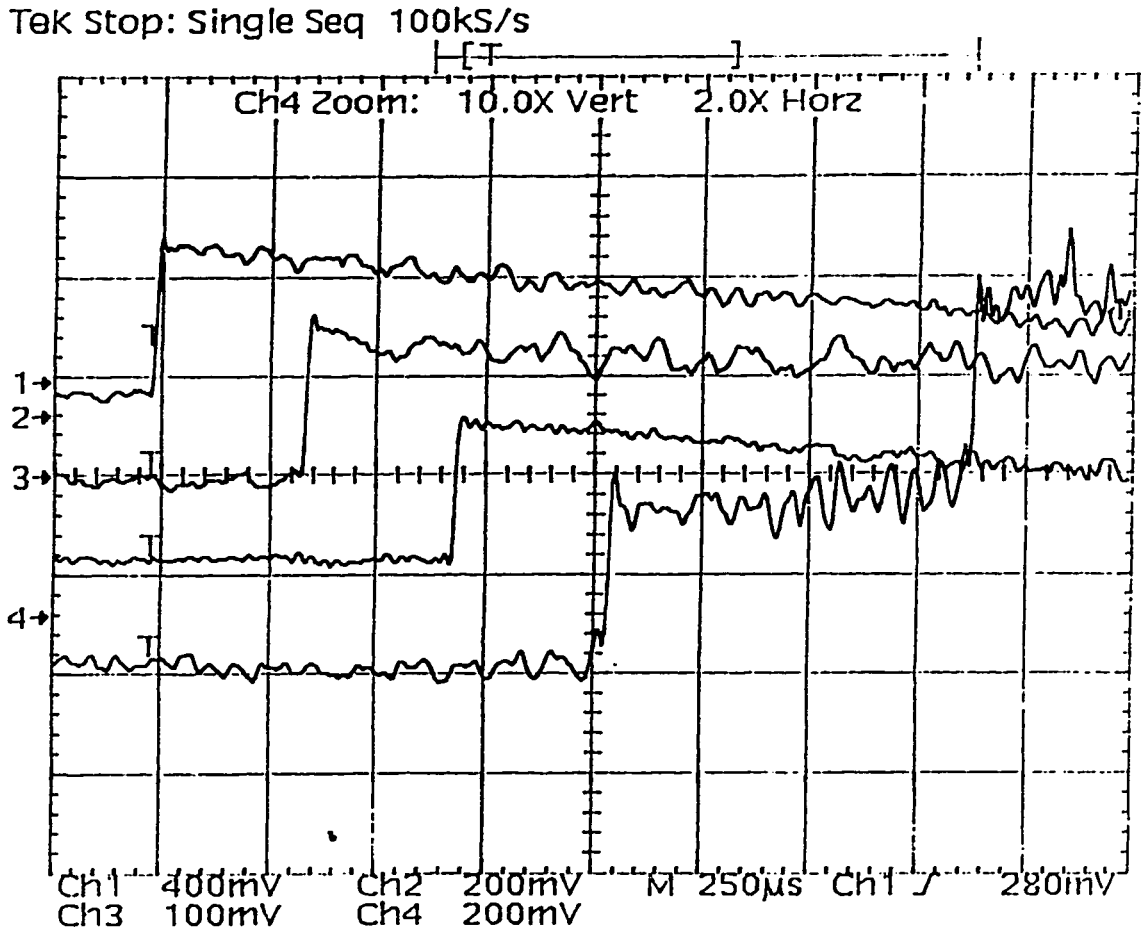

Fig.(4.6) Sample oscilloscope output for pressure transducer calibration.

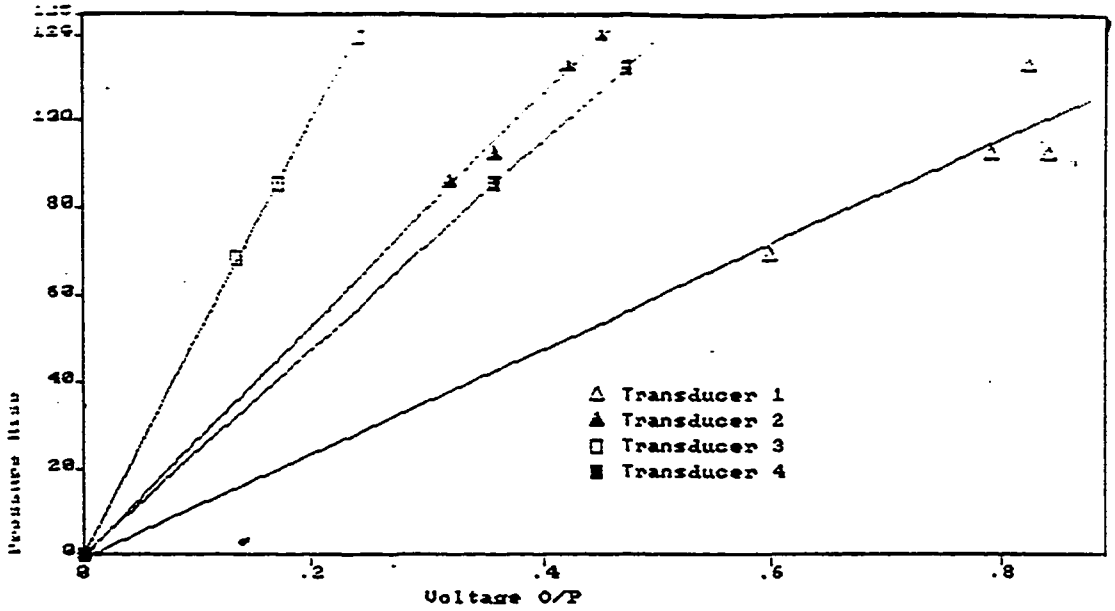

THE REGRESSION POLYNOMIAL OF LINE 1 -

(-7.854E-01) + (1.203E+02)*X
THE VARIANCE - 5.639E+01

THE REGRESSION POLYNOMIAL OF LINE 2 -

(-3.395E-01) + (2.652E+02)*X
THE VARIANCE - 3.048E+00

THE REGRESSION POLYNOMIAL OF LINE 3 -

(1.270E-01) + (4.979E+02)*X
THE VARIANCE - 8.448E-01

THE REGRESSION POLYNOMIAL OF LINE 4 -

(-2.844E-01) + (2.77xE+02)*X
THE VARIANCE - 9.030E-04

Fig.(4.7) Pressure transducers' calibration curves.

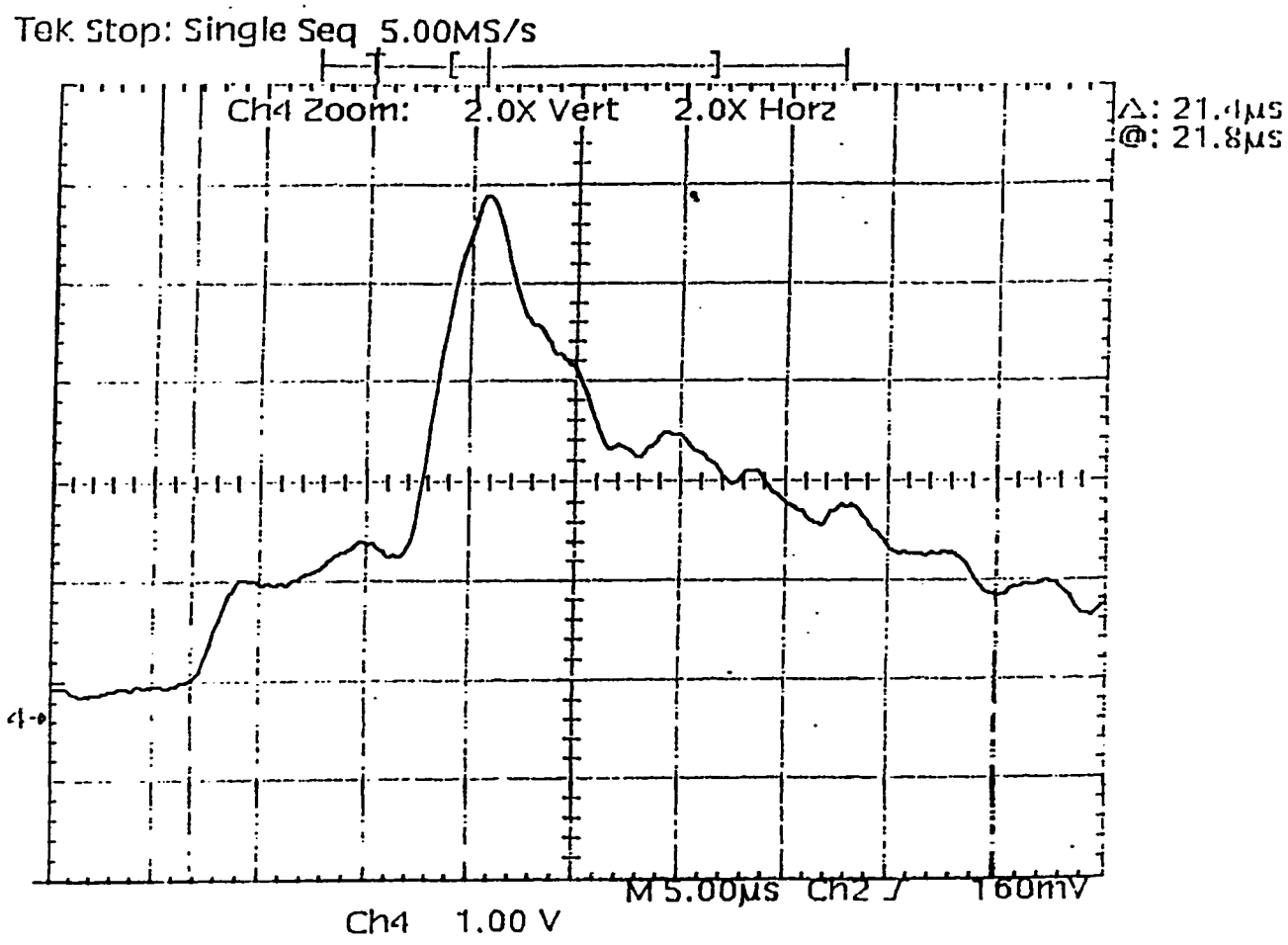

Fig.(4.8) Sample oscilloscope output for cylindrical imploding shock.
(near center, no bleed)

a.

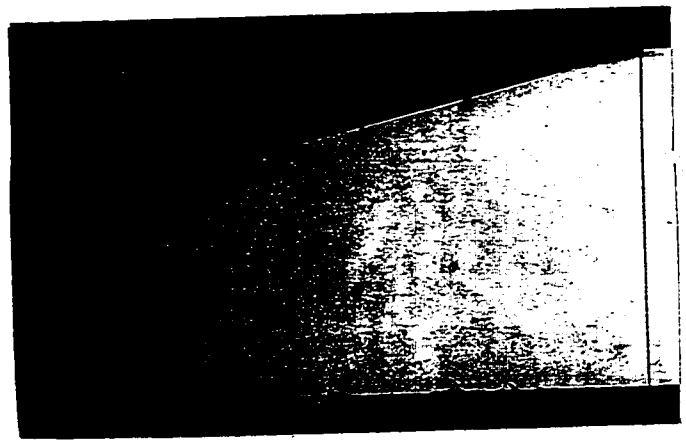

b.

c.

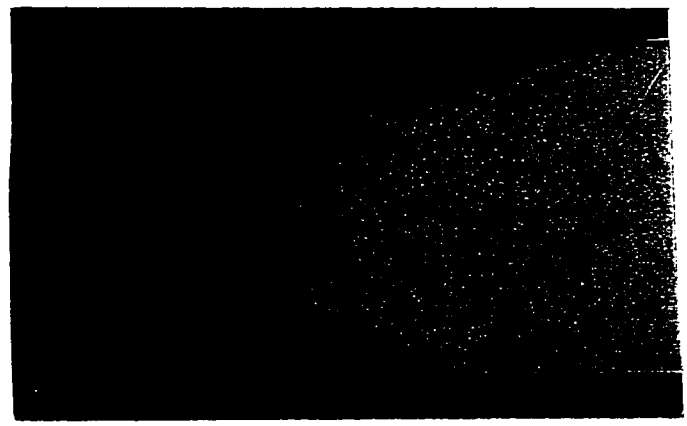

Fig. 5.1 Schlieren photos for shock propagation over a 15° ramp, $M_o = 2.106$

d.

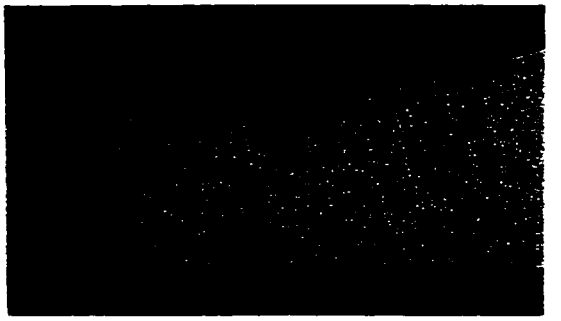

e.

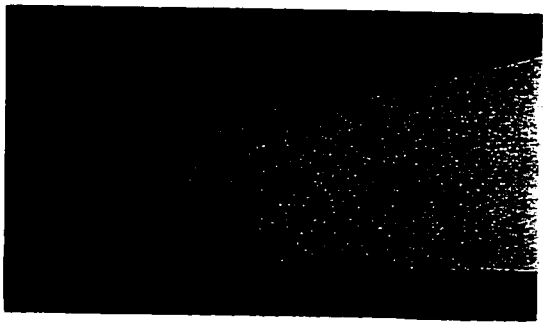

f.

Fig. 5.1 Cont'd

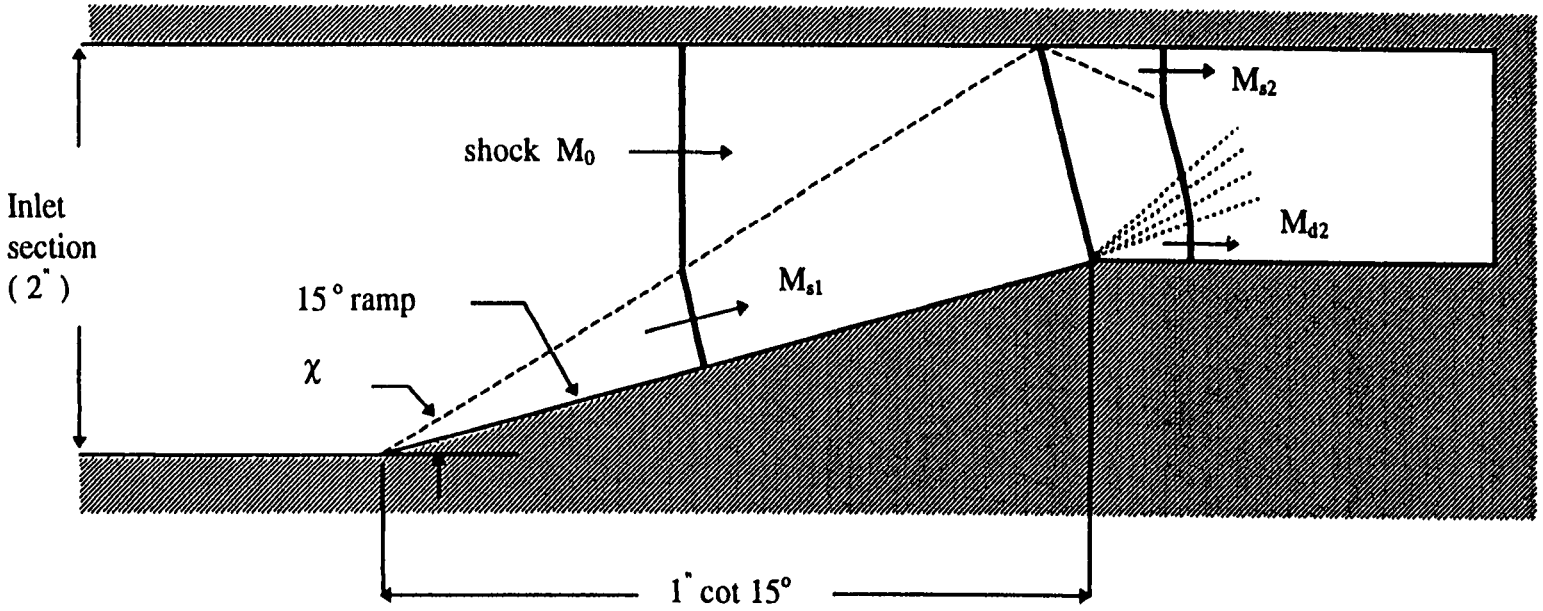

M_0 = Incident shock Mach number

M_{s1} = First stem Mach number

M_{s2} = Second stem Mach number

M_{d2} = Diffracted shock Mach number

χ = Shock-shock angle

Fig.(5.2) Shock front stages for the ramp test case

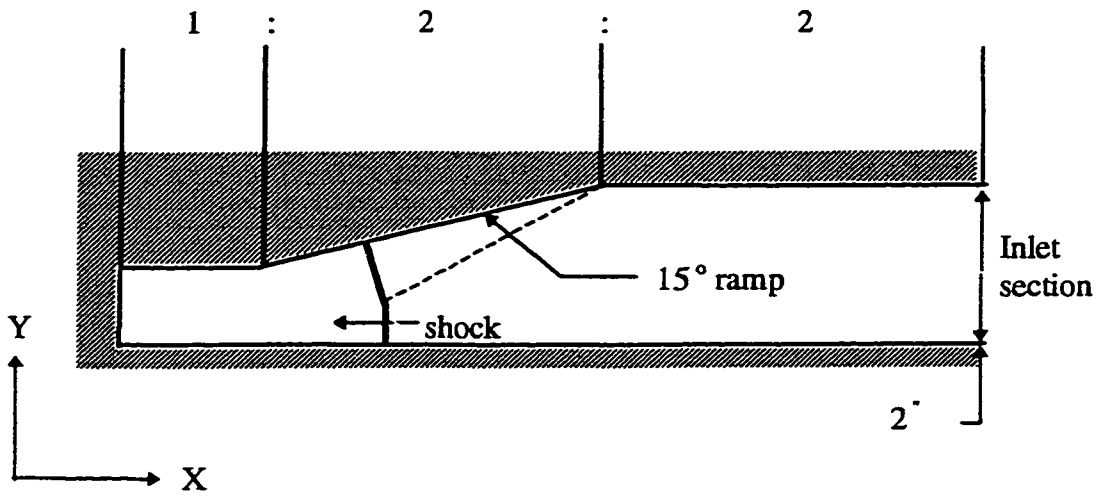

a) Domain geometry

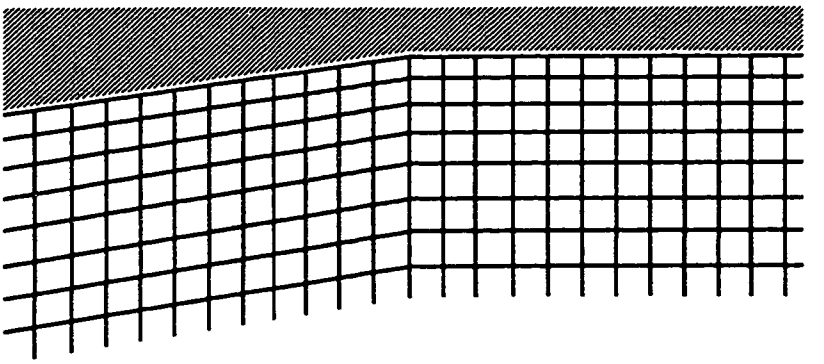

b) Grid geometry near
the concave edge (x 10)

Fig.(5.3) Computational domain for the ramp test case.

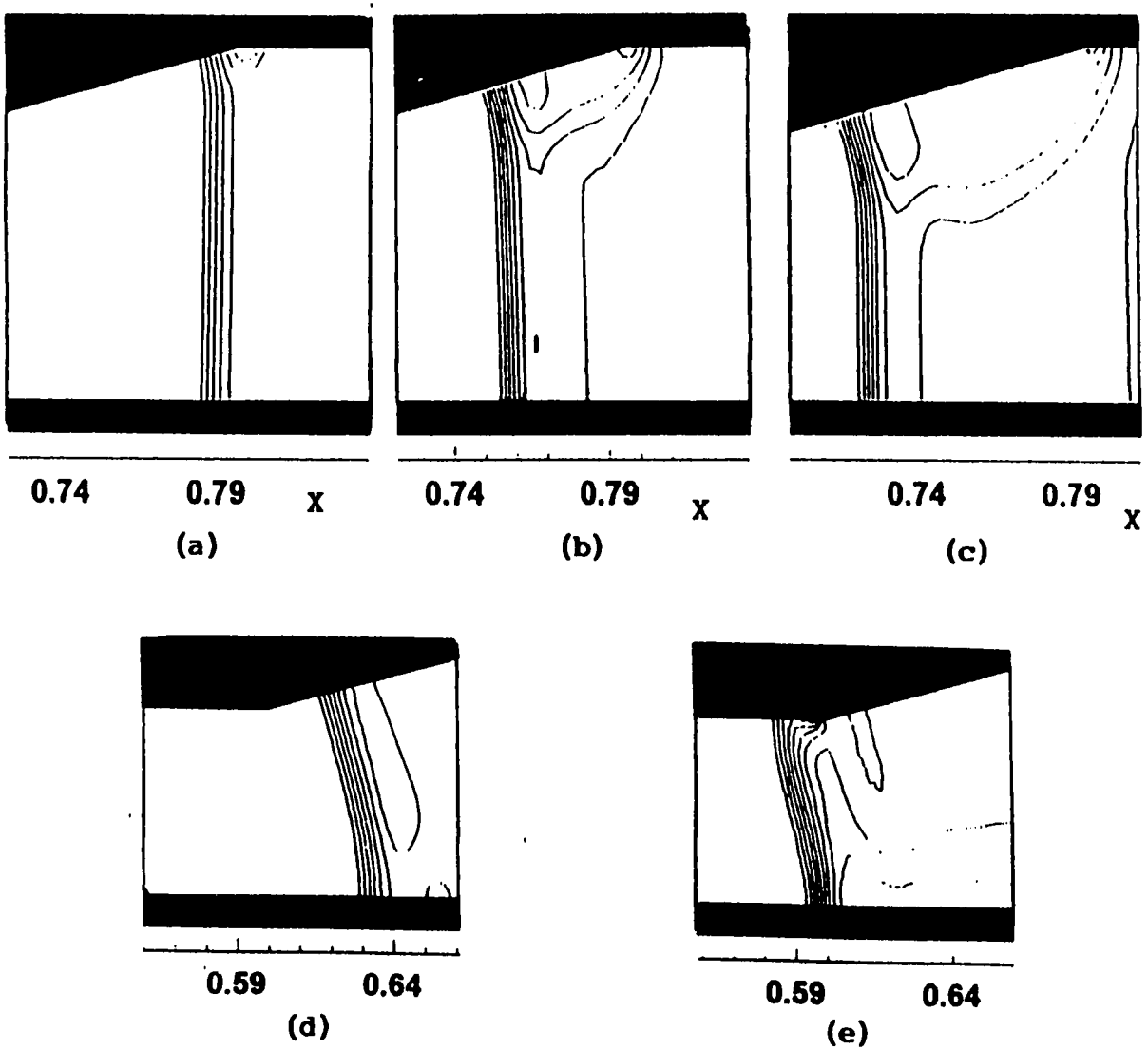

Fig.(5.4) Density contours for the ramp test case.

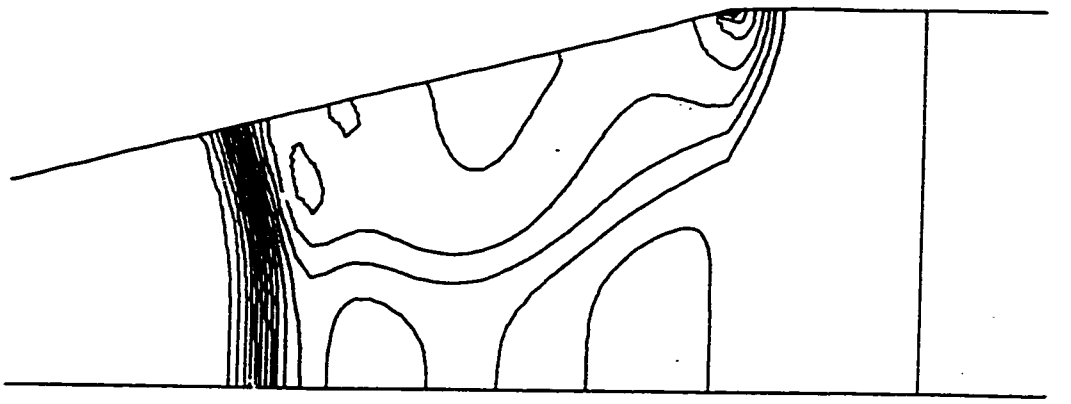

150 x 50

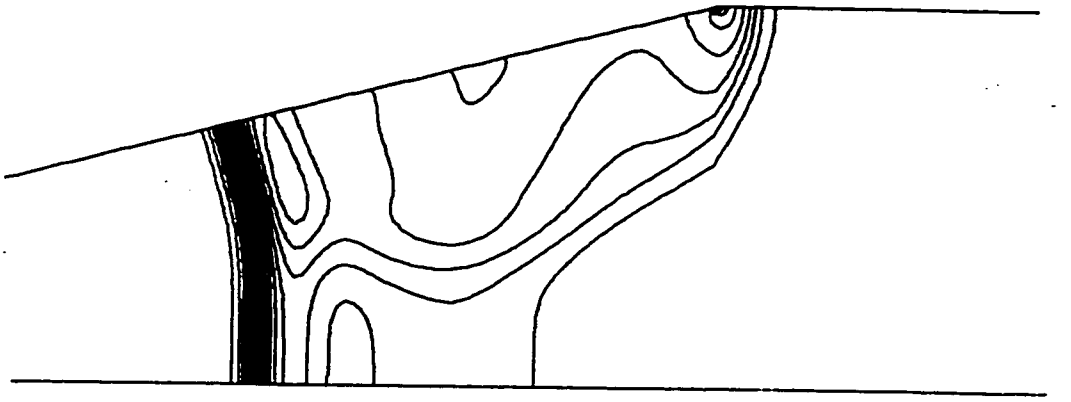

300 x 70

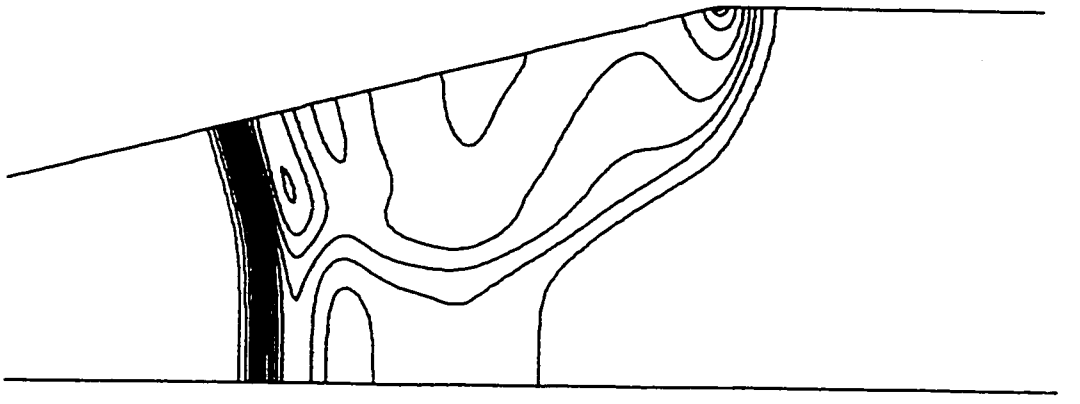

540 x 90

Fig.(5.5) Grid senitivity checks for the ramp problem ($M_0 = 2.106$)
(density contours)

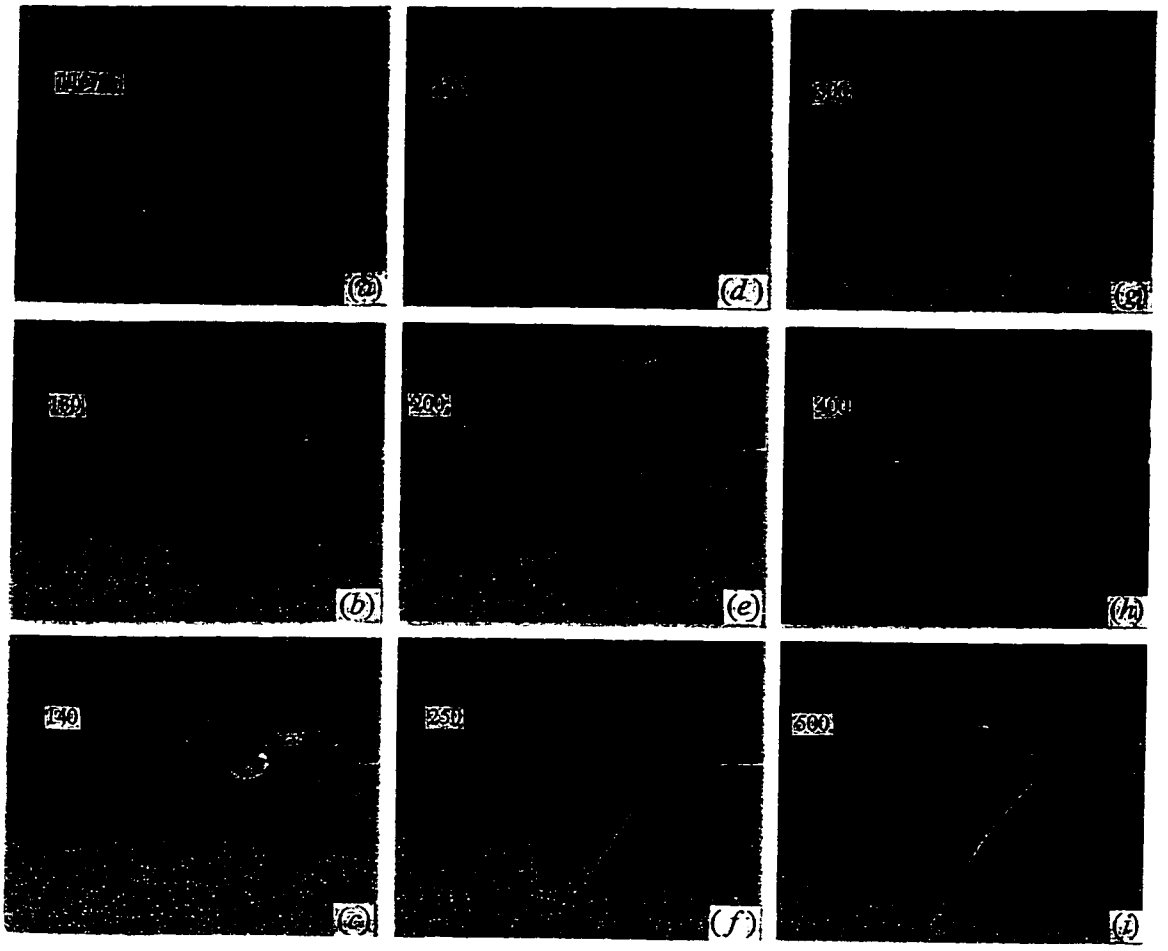

Fig.(5.6) Schlieren photos for shock-slit interaction ($M_0 = 2.33$)
(Ostrowski [64]).

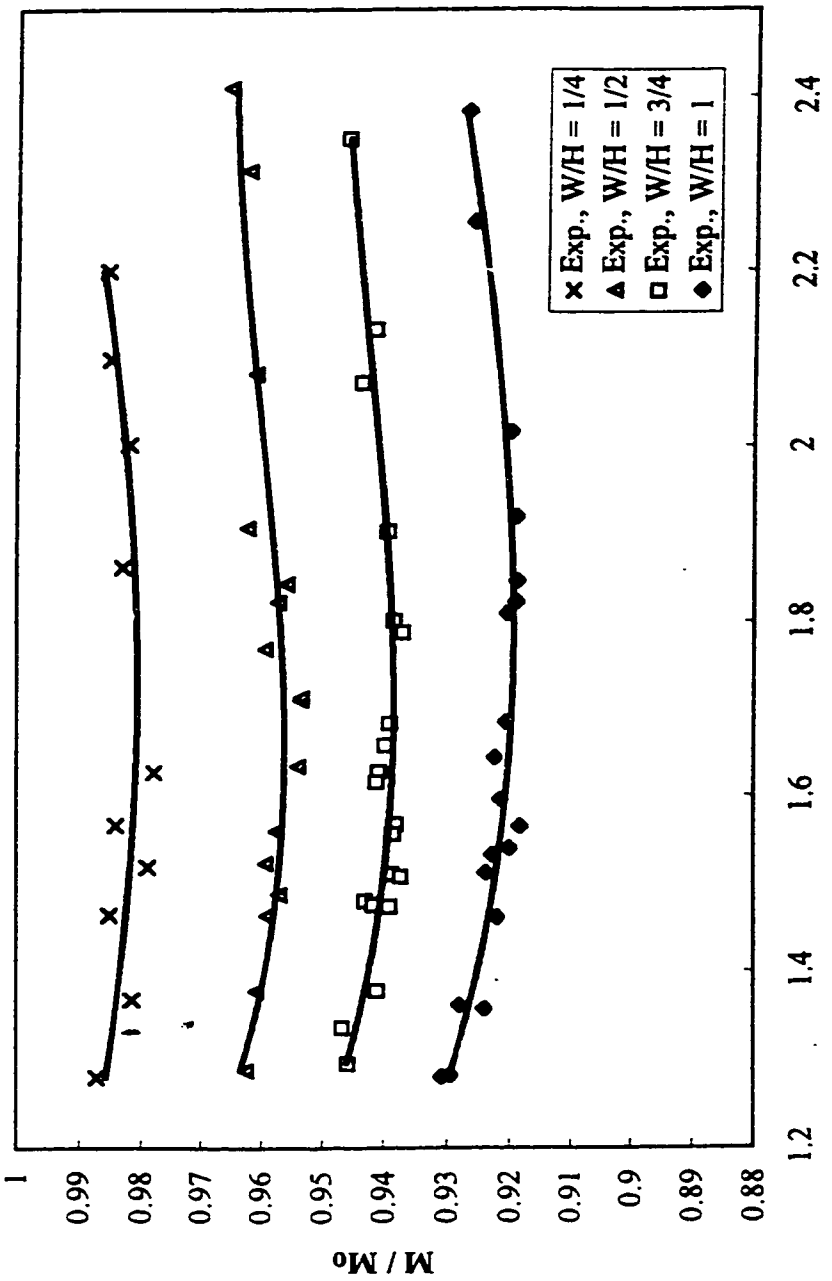

Fig.(5.7) Attenuation coefficient for shock-slit interaction.

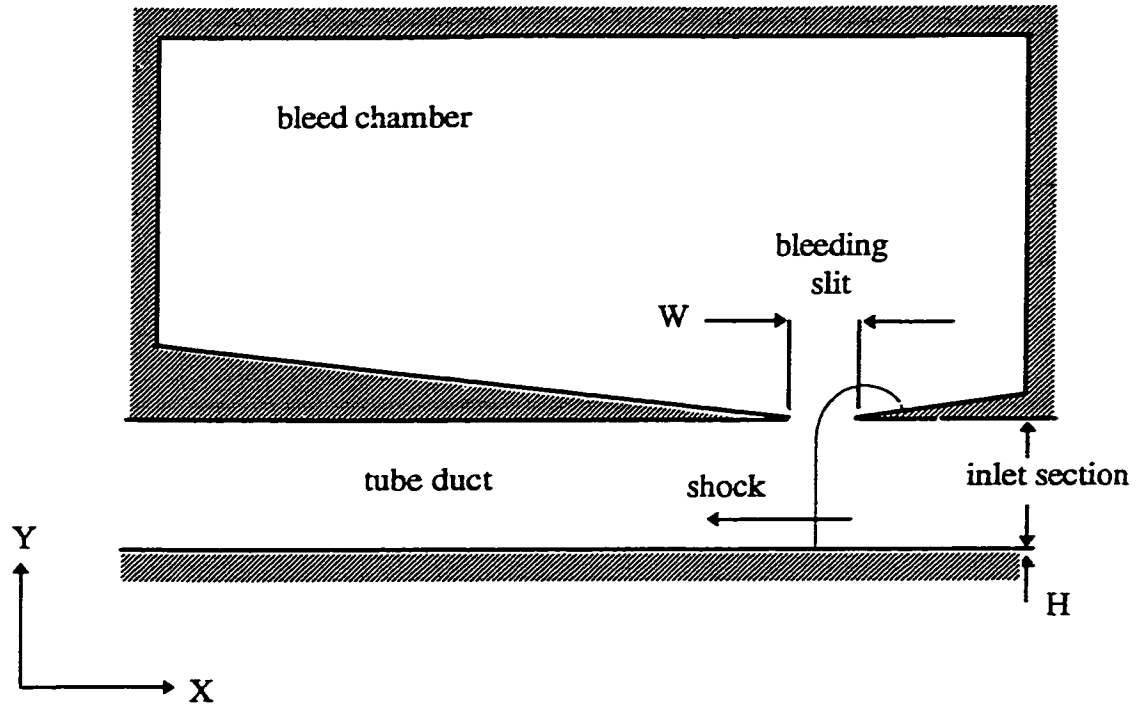

a) Domain geometry

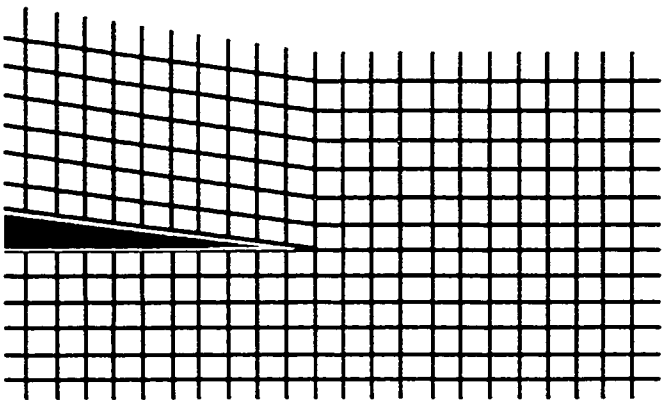

b) Grid near the downstream edge (x 10)

Fig.(5.8) Computational domain for shock-slit interaction ($M_0 = 2.33$).

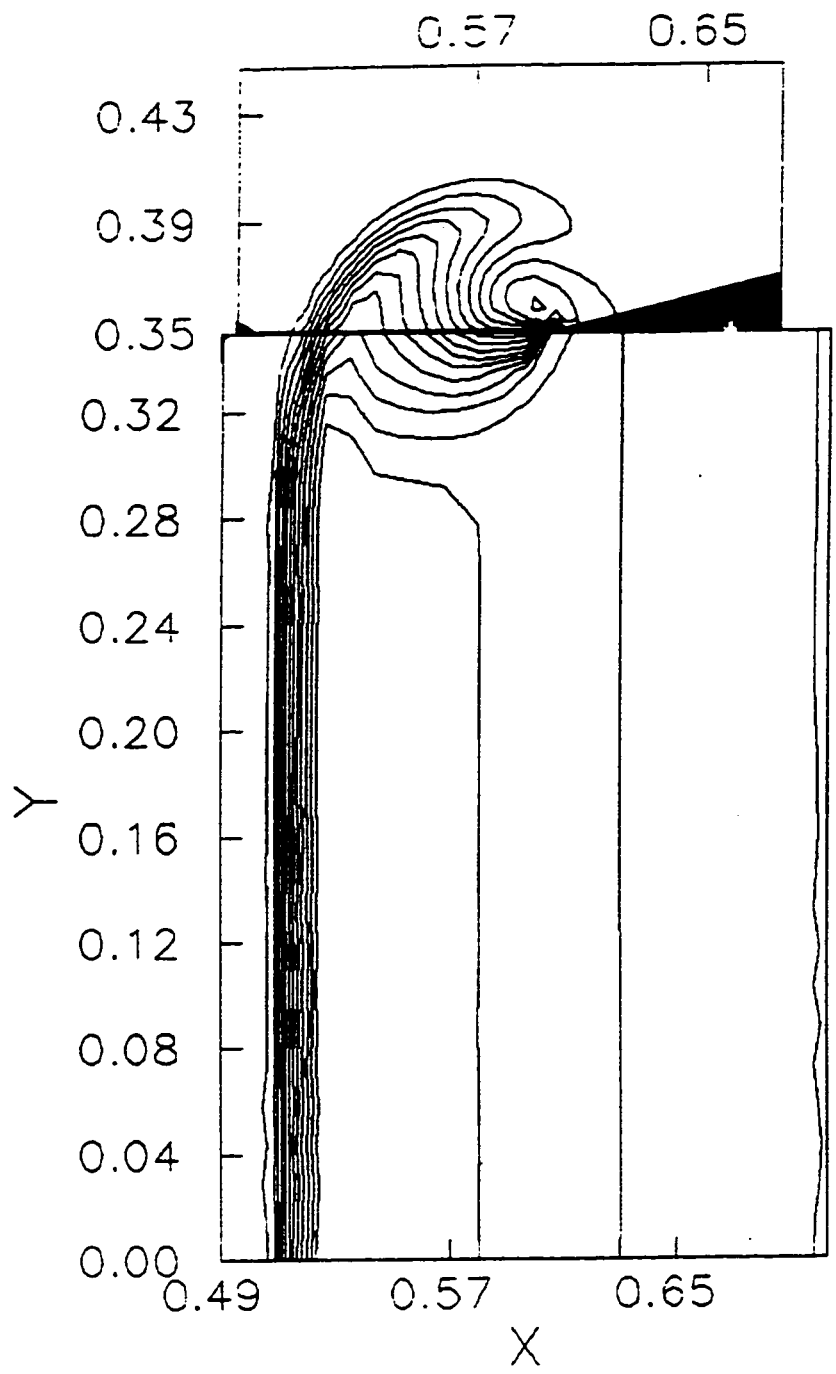

Fig.(5.9a) Density contours for shock-slit interaction
($M_0 = 2.33$, 40 time steps).

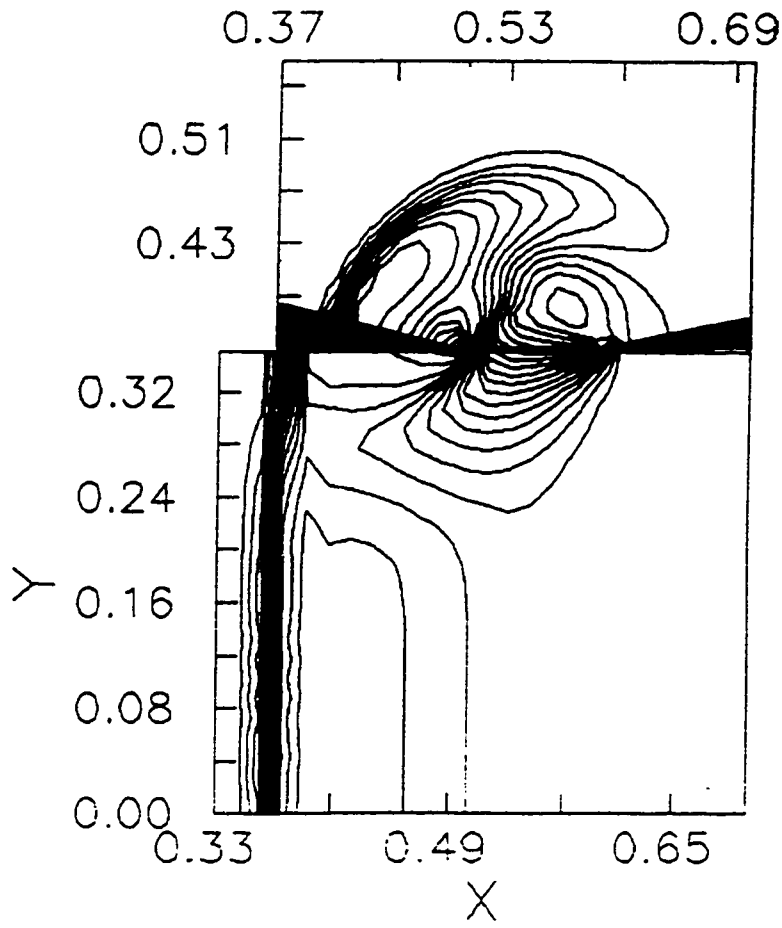

Fig.(5.9b) Density contours for shock-slit interaction
(M_0 = 2.33, 80 time steps).

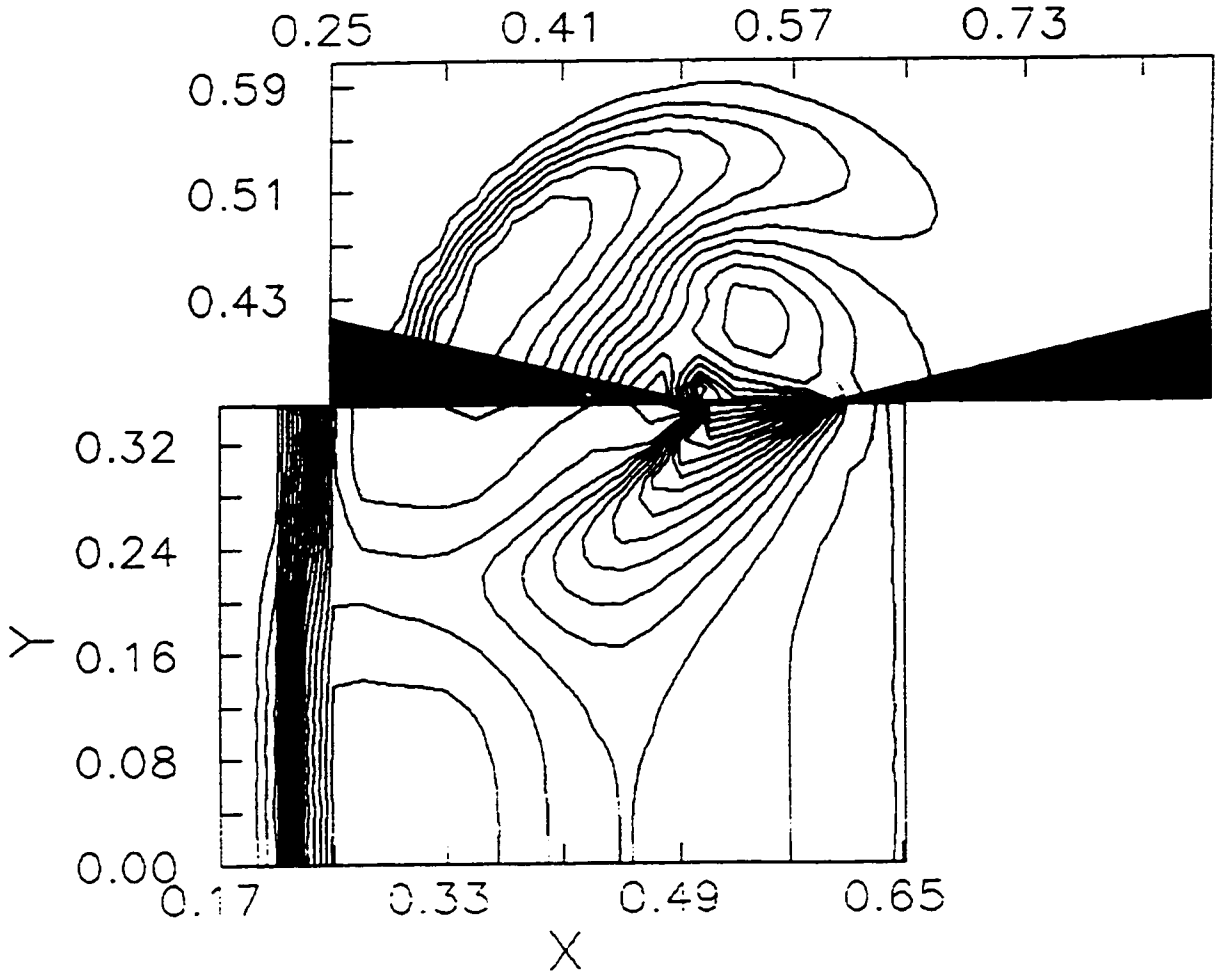

Fig.(5.9c) Density contours for outer diffracted shock
($M_0 = 2.33$, 120 time steps).

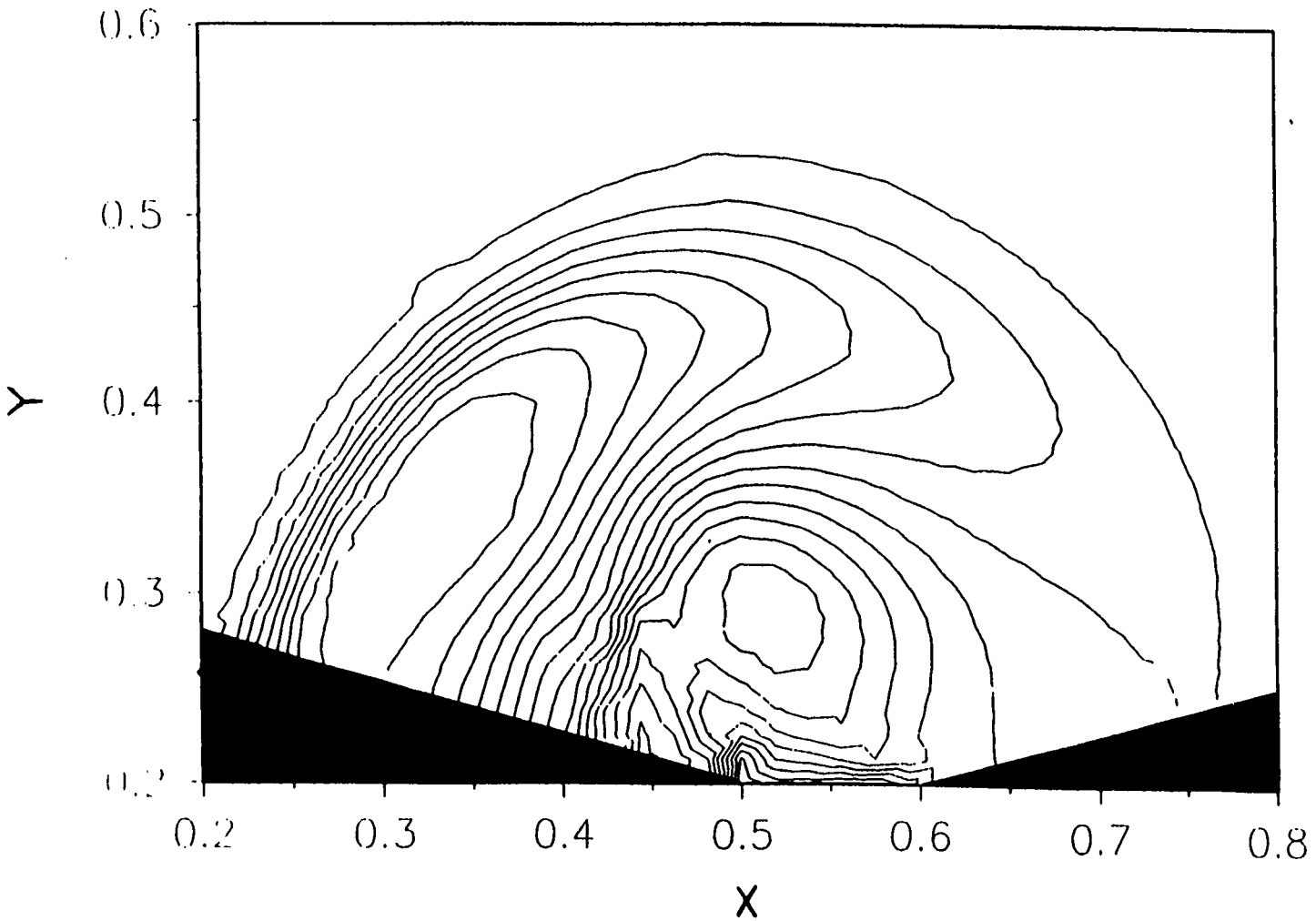

Fig.(5.9d) Density contours for outer diffracted shock
(M_0 = 2.33, 150 time steps).

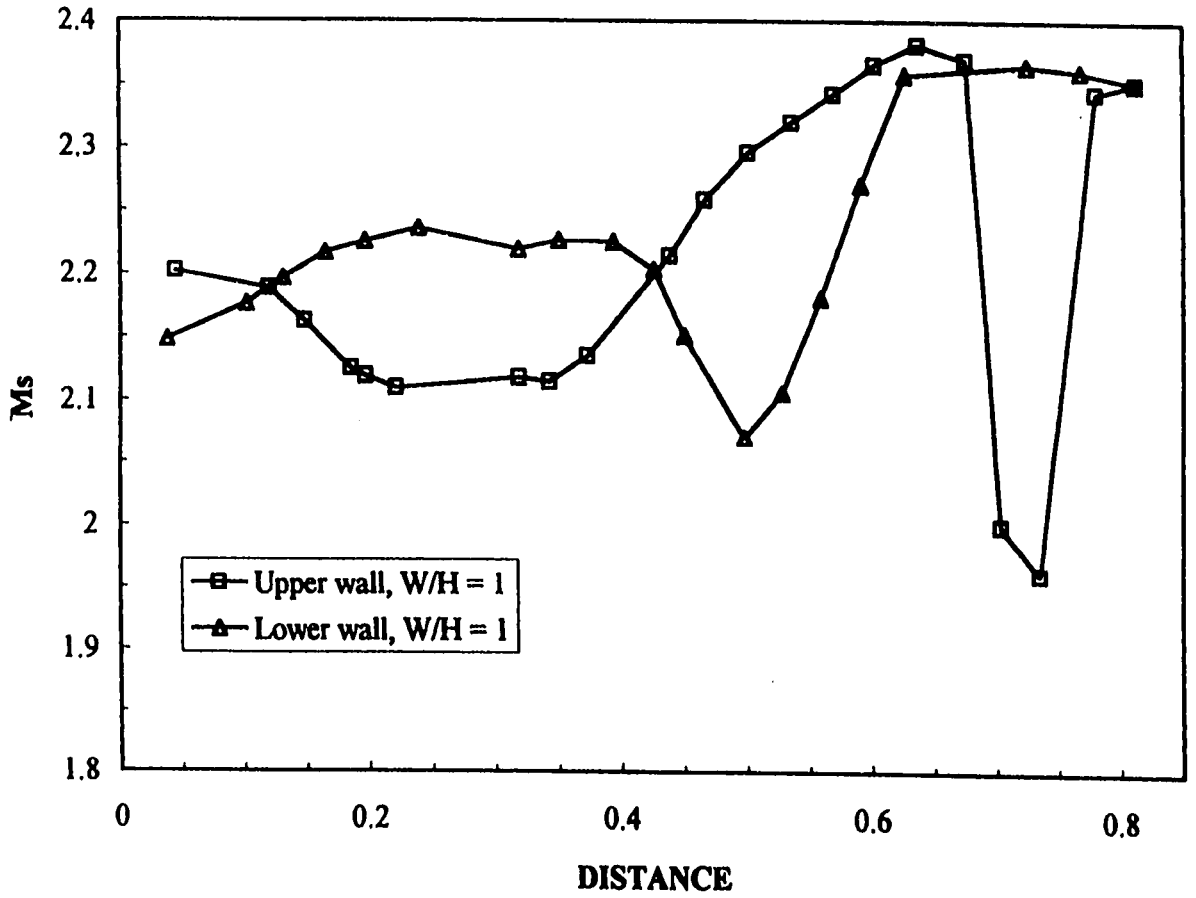

Fig.(5.10) Shock Mach number distribution along the duct walls (W/H = 1.0).

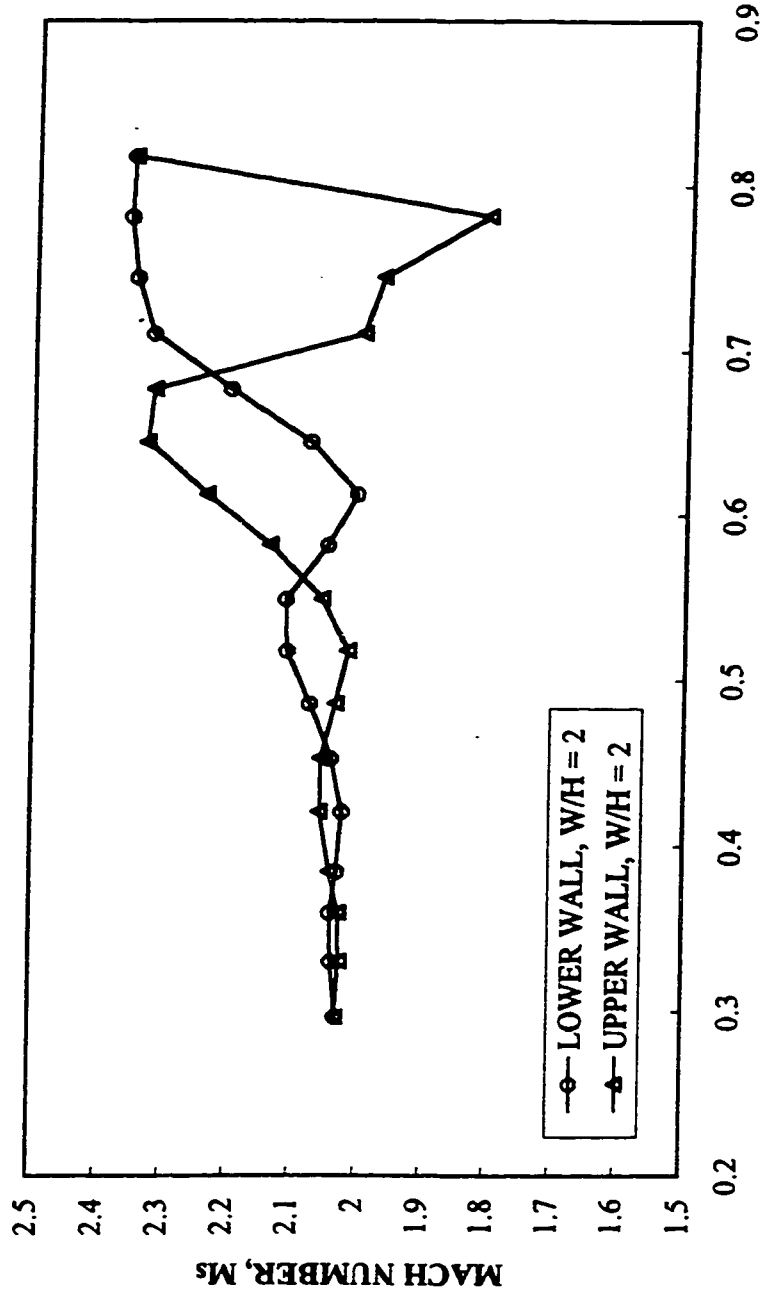

Fig.(5.11) Shock Mach number distribution along the duct walls (W/H = 2.0).

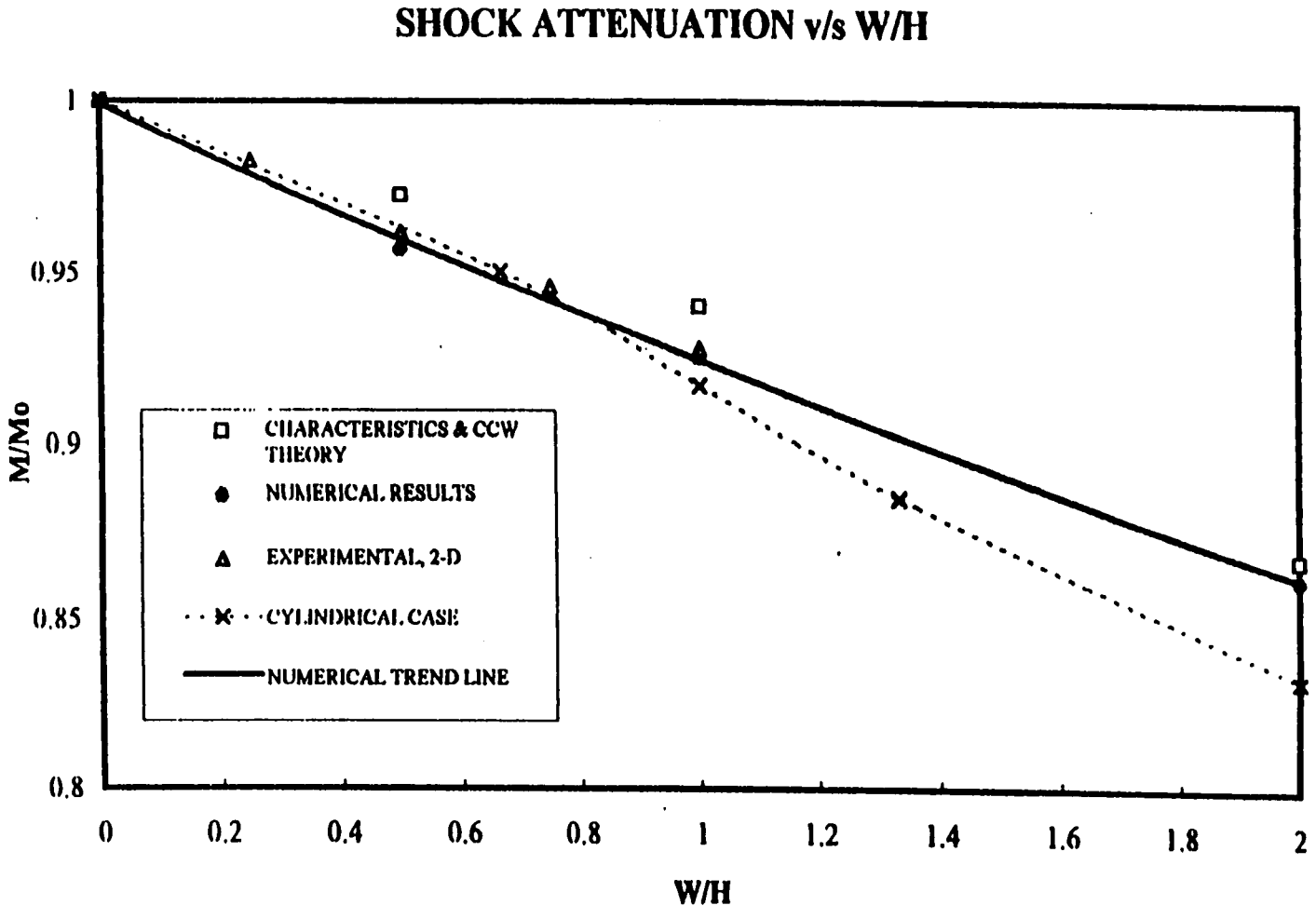

Fig.(5.12) Attenuation coefficient for the shock-slit interaction ($M_0 = 2.33$).

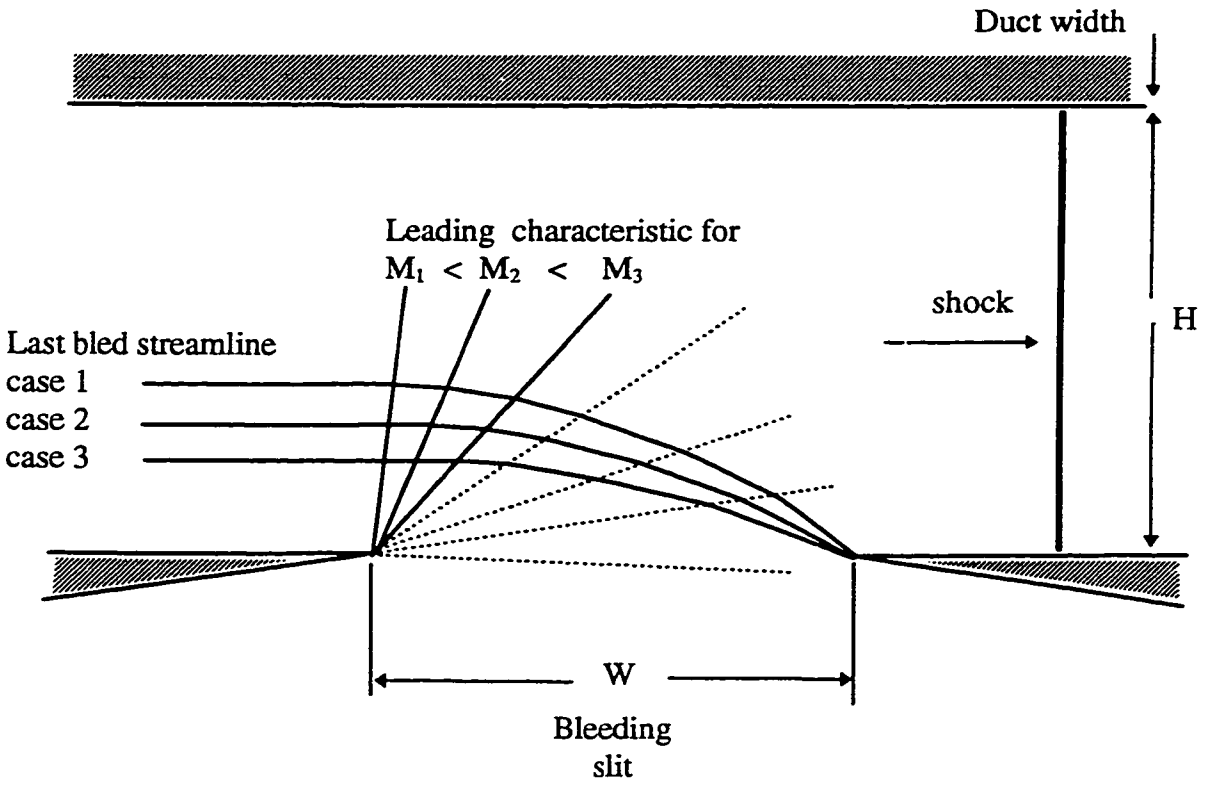

Fig.(5.13) The effect of incident Shock Mach number on bleed ratio (supersonic duct flow).

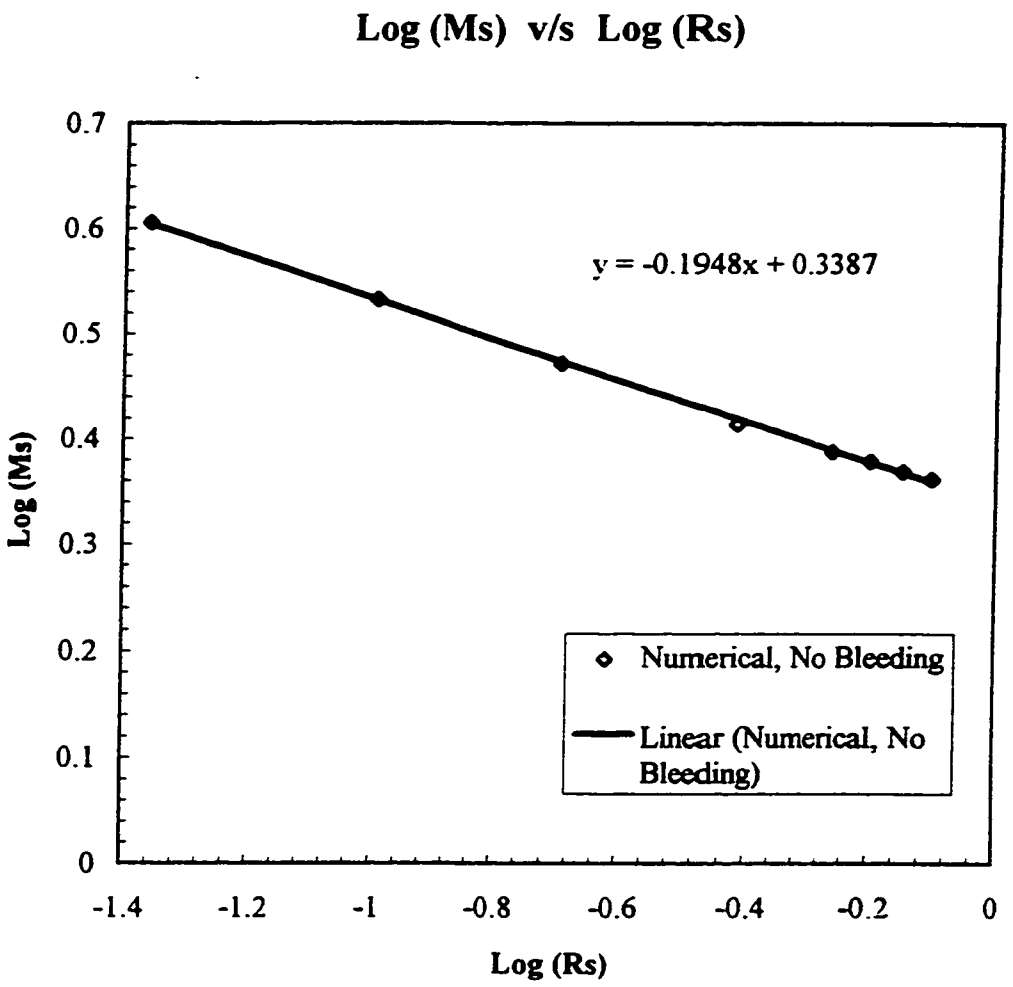

Fig.(5.14) Converging shock Mach number .vs. shock radius.

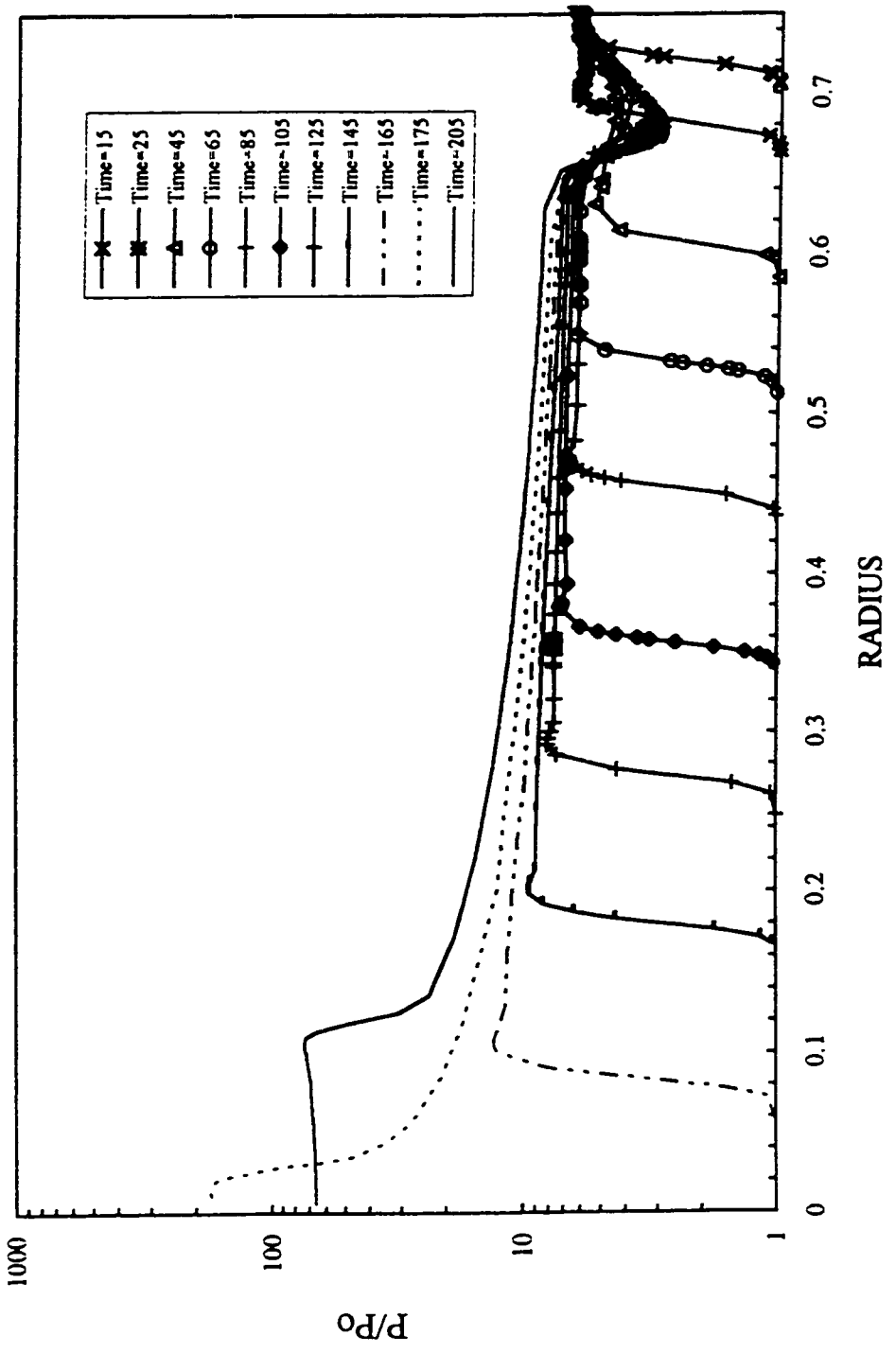

Fig.(5.15) Pressure distribution for converging cylindrical shocks.

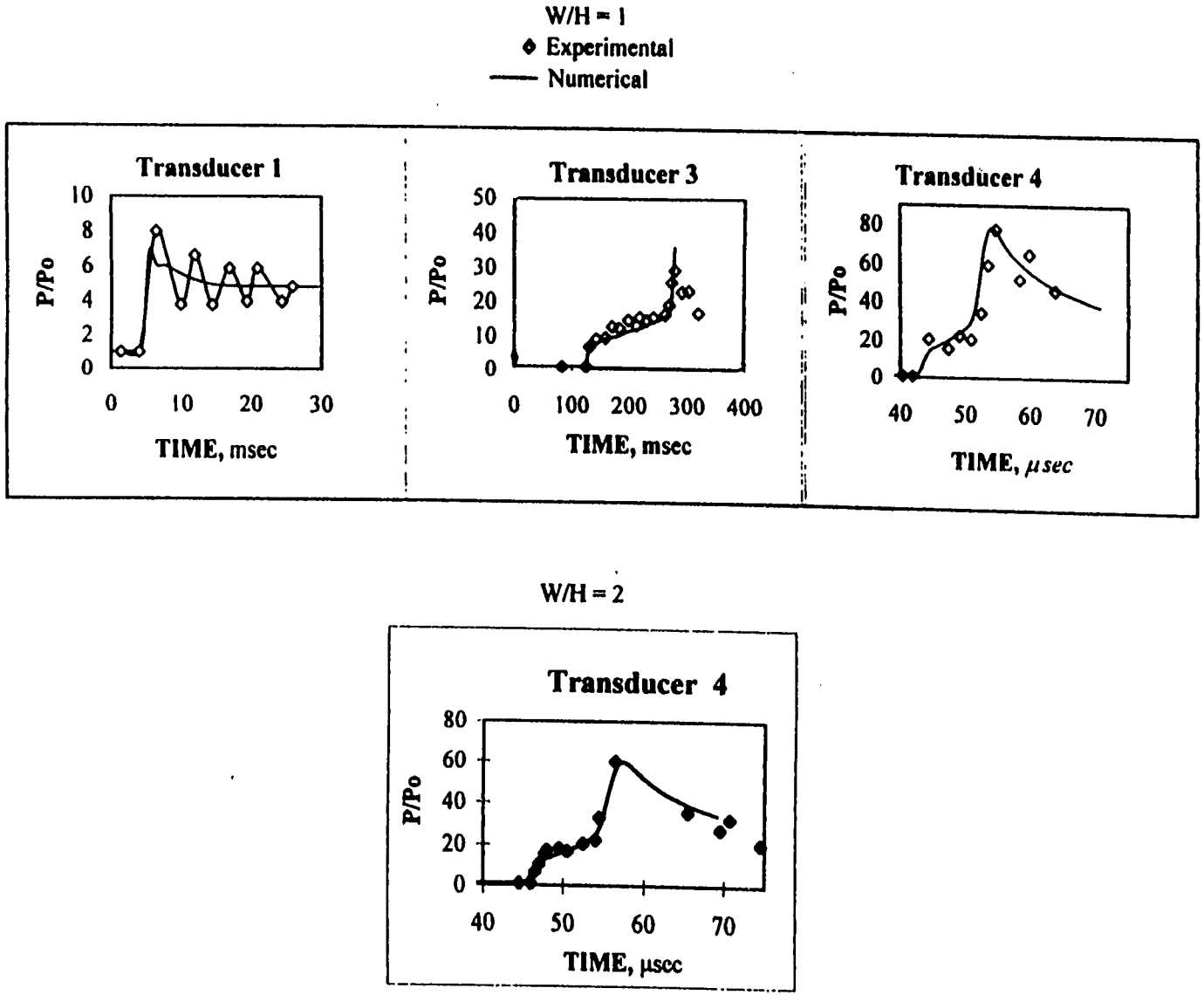

Fig.(5.16) Numerical and experimental pressure history at transducer locations ($M_0 = 2.33$).

W/H = 0.25		W/H = 0.5		W/H = 0.75		W/H = 1	
Mo	M/Mo	Mo	M/Mo	Mo	M/Mo	Mo	M/Mo
2.200	0.986	2.409	0.966	2.352	0.946	2.383	0.927
2.100	0.985	2.314	0.963	2.135	0.942	2.255	0.926
2.003	0.982	2.084	0.961	2.074	0.944	2.017	0.920
1.863	0.983	1.908	0.962	1.904	0.939	1.920	0.919
1.628	0.978	1.844	0.956	1.802	0.938	1.847	0.919
1.567	0.984	1.823	0.957	1.789	0.937	1.823	0.919
1.519	0.979	1.770	0.959	1.684	0.939	1.810	0.920
1.465	0.985	1.711	0.954	1.659	0.940	1.685	0.921
1.368	0.982	1.714	0.954	1.629	0.941	1.644	0.922
1.280	0.987	1.635	0.954	1.617	0.941	1.596	0.921
		1.559	0.958	1.568	0.938	1.565	0.918
		1.523	0.959	1.557	0.939	1.540	0.920
		1.487	0.957	1.511	0.939	1.532	0.923
		1.463	0.959	1.508	0.937	1.511	0.924
		1.378	0.961	1.481	0.943	1.461	0.922
		1.288	0.963	1.476	0.942	1.361	0.928
				1.474	0.939	1.357	0.924
				1.379	0.941	1.282	0.930
				1.337	0.947	1.280	0.931
				1.295	0.946		

Table (5.1) Experimental results for 2-D shock-slit interaction ($M_0 = 2.33$).

W/H = 1						W/H = 2	
Transducer 1		Transducer 3		Transducer 4		Transducer 4	
Time	P/Po	Time	P/Po	Time	P/Po	Time	P/Po
1.40	1.00	83.40	1.00	40.40	1.00	44.50	1.00
4.00	1.00	125.00	1.00	41.90	1.00	46.00	1.00
6.40	8.00	130.94	7.00	44.40	21.00	46.50	6.65
9.90	3.76	142.83	9.31	47.40	16.00	47.00	10.41
11.90	6.64	158.67	9.77	49.10	22.88	47.70	15.44
14.40	3.76	170.56	13.00	50.90	21.00	48.00	17.32
16.90	5.88	182.45	12.54	52.40	34.75	49.50	17.95
19.40	3.97	198.29	14.85	53.50	59.75	50.50	16.69
20.90	5.88	212.16	13.46	54.70	77.88	52.50	20.46
24.40	3.97	218.10	15.77	58.40	52.25	54.00	22.34
25.90	4.82	229.99	14.85	59.90	65.38	54.50	33.01
		241.87	15.77	63.90	46.63	56.50	60.00
		261.68	16.69			65.50	35.52
		269.60	19.46			69.50	27.36
		273.56	25.92			70.70	32.38
		279.51	29.62			74.50	20.46
		291.39	23.15			78.50	22.97
		303.28	23.43				
		319.12	17.15				

Table (5.2) Experimental results for cylindrical shock-slit interaction ($M_0 = 2.33$).